Emerin and Inherited Disease

by

Janet Hsiao

B.S., Chemical Engineering
Massachusetts Institute of Technology, 2003

Harvard-MIT Division of Health Science and Technology
in partial fulfillment of the requirements for the degree of

Masters of Engineering in Biomedical engineering
at the
Massachusetts Institute of Technology

September 2004

Signature of Author: .....

Janet Hsiao
Harvard-MIT Division of Health Sciences and Technology
Masters of Engineering in Biomedical Engineering
16 August 2004

Certified by: .....

Richard Lee
Associate Professor Harvard Medical School
Thesis Supervisor

Certified by: .....

Roger Kamm
Professor of Biological Engineering
and Mechanical Engineering
Thesis Supervisor

Accepted by: .....

Martha L. Gray, Ph.D.
Edward Hood Taplin Professor of Medical and Electrical Engineering
Co-Director, Harvard-MIT Divison of Health Sciences and Technology

Emerin and Inherited Disease

by

Janet Hsiao

Submitted to the department of Health Science and Technology
on August 16, 2004 in Partial Fulfillment of the Requirements for the Degree of
Masters of Engineering in Biomedical Engineering

Abstract

Mutations in the lamin A/C gene (*Lmna*) and the lamin-associated protein emerin gene (*EM*) cause a variety of human diseases including Emery-Dreifuss muscular dystrophy, dilated cardiomyopathy, familial partial lipodystrophy, Charcot-Marie-Tooth Neuropathy and Hutchinson-Gilford progeria syndrome. The molecular mechanisms underlying the varied phenotypes are unknown, and both a mechanical stress hypothesis and an altered gene expression hypothesis have been proposed to explain the tissue specific effects observed in laminopathies. To investigate the role of emerin in mechanotransduction, lamin A/C deficient ($Lmna^{-/-}$) fibroblasts, and emerin deficient ($EM^{-/y}$) fibroblasts were studied for nuclear mechanical properties, cytoskeletal stiffness, and mechanical strain-induced signaling. $EM^{-/y}$ fibroblasts exhibited similar cell sensitivity, nuclear and cytoskeletal properties compared to wild type cells under stress and strain. Interestingly, both $Lmna^{-/-}$ and *EM-/y* fibroblasts had impaired mechanotransduction, characterized by attenuated expression of the mechanosensitive genes *egr-1*, *iex-1*, and *txnip* in response to mechanical stimulation. In addition, NF-κB signaling appeared disturbed in $Lmna^{-/-}$ cells, but normal in $EM^{-/y}$ fibroblasts. The relationship between changes in cytoskeletal stiffness recently discovered in $Lmna^{-/-}$ cells and nuclear mechanics under strain was explored using a computational finite elemental model. Analysis of the several models using variations in material properties and cell geometry revealed that nuclear shape, material properties of the cytoskeleton and nucleus, as well as the size and location of strain application on the cell are important parameters in determining the magnitude of stress and strain within the nucleus and at the nuclear surface.

Acknowledgements

I would like to thank Rich and Brigham and Women's Hospital for giving me the opportunity to work in their lab and for the patience and support I was given as I struggled through learning various molecular biology techniques. I'd like to also thank Roger Kamm for his supervision and helping to define the engineering aspect of our project through ADINA modeling. I'd also like to thank Roger Mark for guiding me through the new HST Masters of Engineering Program.

I also would like to thank members of the Lee and Kamm lab for all their incredible patience in teaching me several biological experimental techniques and the aspects of the lab. Jan Lammerding has been an integral member of this project and none of the work would have been possible without his guidance, supervision, support, and infinite patience. I'd also like to thank Christian Schulze, Jun Yoshioka, Parth Partwari, and the rest of the Lee lab for their support and wisdom. Mohammad Reza Kaazempur Mofrad and Hélène Karcher have been vital to the modeling aspect of the thesis. Their teaching and expertise of ADINA in cell modeling have helped to make the engineering aspect of this thesis enjoyable.

Finally I would like to thank my family and friends for the encouragement and support they have given as I transitioned from an undergraduate student to a graduate student. Janet Lai has been an incredibly caring and supportive friend during academic and emotionally difficult times – thank you.

Table of Contents

List of Tables and Figures

1.0 EMERIN and INHERITED DISEASE

1.1 INTRODUCTION

1.1.1 Nucleus and Nuclear Envelope Proteins

The distinguishing feature of eukaroyotic cells is the nucleus, the genetic center of the cell that directs and controls DNA replication, RNA transcription and processing for the synthesis of proteins and enzymes, and ribosome assembly within the cell.[1] The nuclear envelope surrounding the chromatin separates the nucleus from the cytoplasm and has been found to not only regulate the entry and exit of molecules between the nucleus and cytoplasm, but also to play an important role in development, structural organization of the nucleus, and nuclear function in different tissues. The nuclear envelope is composed of the inner and outer membranes, separated by a luminal space that is continuous with the endoplasmic reticulum lumen. Communication and regulation of nuclear transport between the nucleoplasm and cytoplasm occurs through nuclear pore complexes at the sites where the inner and outer membrane join. Underneath the inner nuclear membrane is nuclear lamina, a meshwork of intermediate filaments which includes lamin proteins and several lamin-associated proteins. These integral membrane proteins include three isoforms of lamina-associated protein 1 (LAP1), five isoforms of lamin-associated protein 2 (LAP2), and one isoform of lamin associated protein 2α (lacks a transmembrane domain). The five isoforms of LAP2 include emerin, MAN1, lamin B receptor (LBR), nurim, and UNC-84 [2]. Near the inner nuclear membrane is the peripheral chromatin, a large portion of which is heterochromatin (Figure 1.1).

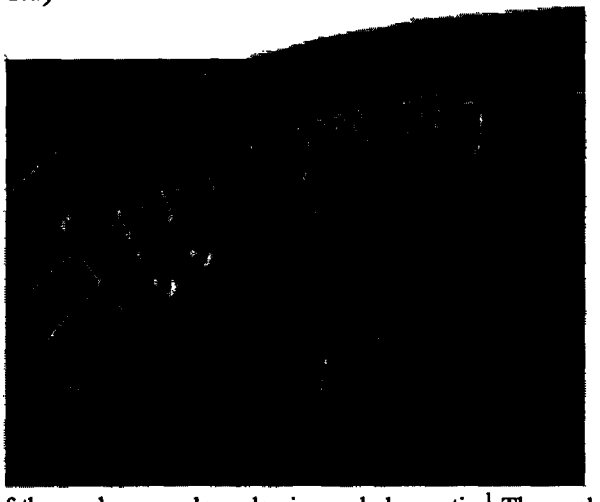

Figure 1.1 Schematic view of the nuclear envelope, lamina and chromatin.[1] The nuclear envelope is composed of the inner and outer membranes, separated by a luminal space that is continuous with the endoplasmic reticulum lumen. Underneath the inner nuclear membrane is the nuclear lamina, a meshwork of intermediate filaments which includes lamin proteins and several lamin-associated proteins.

Lamin

Lamins are type V intermediate filament proteins of the nuclear lamina, a meshwork of nuclear-specific proteins underlying the inner nuclear membrane. Lamins have been found to have many different functions in the cell, including anchoring and evenly distributing nuclear pore complexes, recruiting other proteins such as emerin to the nuclear envelope, and

determining nuclear shape and size. Three lamin genes (Lamin A/C, B1, and B2 gene) are located at autosomal chromosome 1 (1q21.2-q21.3) in humans. The Lamin A/C gene (*Lmna*) is alternatively spliced to produce two major A-type lamin proteins (Lmna A and Lmna C) and two minor A-type lamin proteins (Lmna AΔ10 and Lmna C2 – specific to testis).

Emerin

Emerin, another integral protein of the nuclear inner membrane, is expressed in most human tissues and is bound to nuclear intermediate filaments that are formed by the lamin proteins. This 34 kDa protein belongs to a family of nuclear proteins that include a ~40-residue LEM-domain that binds to barrier-to-autointegration factor (BAF), a conserved chromatin protein. Emerin is not essential for cell viability, but it contributes to shared vital functions, including nuclear assembly and cell cycle progression, and is important in the specific functions of the skeletal muscles, tendons, and heart. Experiments with emerin-deficient *C.elegans* embryos showed that LEM-domain proteins collectively are essential for viability. Overexpression of the full nucleoplasmic domain of emerin extends the mammalian cell cycle by seven hours, supporting emerin's involvement in cell cycle regulation. The nucleoplasmic domain of emerin has dominant effects in *Xenopus* nuclear assembly extracts, suggesting a potential structural role for emerin during nuclear assembly[3]. The interaction of emerin with various binding factors implies multiple roles for emerin in the nucleus. Emerin binds BAF to reassemble at the nuclear envelope after mitosis and is thought to be anchored to the inner nuclear membrane by nesprin-1α. Through its interaction with α- and β-actin as well as F-actin, emerin has the potential to stabilize actin polymers at the nuclear envelope[4]. Emerin also binds directly to two transcription factors Btf and YT521-B. Bft, a transcription repressor is thought to be sequestered by emerin, and thus to suppress apoptosis.[5] YT521-B is involved in determining sites for alternate mRNA splicing, and emerin influences splice site selection by YT521-B[6]. Thus, emerin's interaction with multiple transcription regulators and an RNA splicing factor suggests an important role in transcriptional regulation.[5]

1.1.2 Laminopathies

Most inherited diseases are associated with mutations in a specific gene. Sometimes, mutations in two or more different genes result in diseases with a similar phenotype. Rarely do different mutations in the same gene result in a multitude of seemingly different and unrelated diseases. However, different mutations in the *Lmna* gene have been identified to cause at least six different diseases collectively called laminopathies[7] (Figure 1.2). Through studying the underlying pathways of these laminopathies, the function of the nuclear envelope has been expanded as a key player in development, structural organization of the nucleus, and nuclear function in different tissues. These inherited diseases may arise from global effects of the elimination of lamins A and C, misfolding or truncation of the lamin A carboxy-terminal domain, or through an error in lamin-specific binding to lamina-associated proteins. Laminopathies can be grouped into those affecting skeletal and cardiac muscle and those affecting adipose tissue and bones. Laminopathies affecting striated muscle include X-linked Emery-Dreifuss Musclar Dystrophy (EDMD), the autosomal dominant form of EDMD (AD-EDMD), Limb girdle musclar dystrophy type 1B(LGMD-1B), dilated cardiomyopathy (DCM), and Charcot-Marie-Tooth Neuropathy type 2 B1 (CMT2B1). The laminopathies affecting

adipose tissue are Dunnigan's familial partial lipodystrophy (FPLD) and mandibuloacral dysplasia (MAD). The laminopathies are described in more detail below.

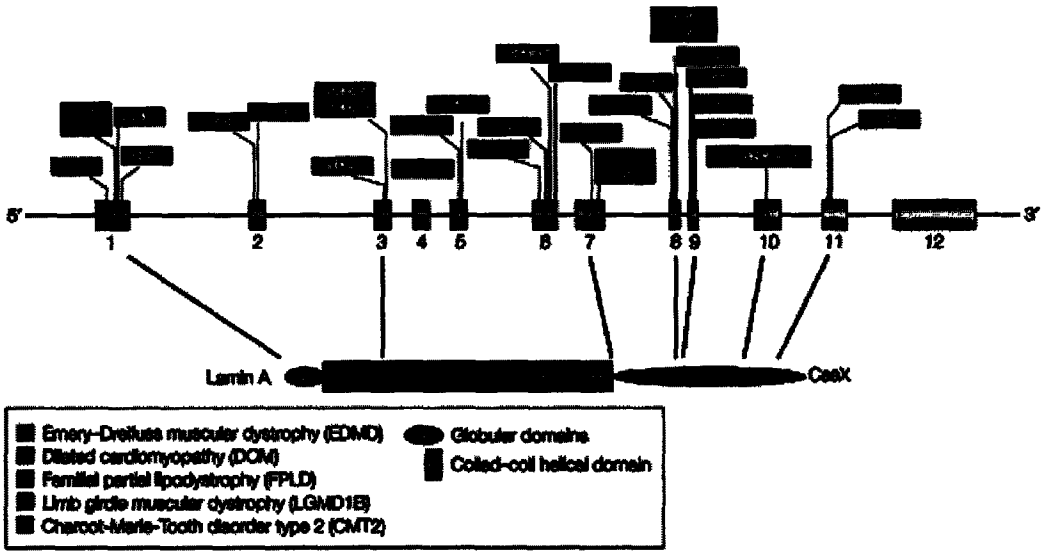

Figure 1.2: Laminopathy-linked mutations in the *Lmna* gene: Different mutations in the *Lmna* A/C gene lead to many different diseases, yet the molecular mechanisms underlying the varied phenotypes are unknown. These inherited diseases may arise from global effects of the elimination of lamins A and C, misfolding or truncation of the lamin A carboxy-terminal domain, or through an error in lamin-specific binding to lamina-associated proteins. Laminopathies can be grouped into those affecting skeletal and cardiac muscle and those affecting adipose tissue and bone. [7]

Skeletal and Cardiomyopathies

X-linked Emery-Dreifuss Muscular Dystrophy (EDMD) was the first disorder to be recognized as a laminopathy and opened a new area of research on the role of the nuclear envelope in disease. EDMD is the third most common X-linked form of muscular dystrophy and is characterized by early onset in childhood with progressive muscle wasting and weakening, contractions in the Achilles and elbow tendons, a rigid spine, abnormal heart rhythms, heart block, and cardiomyopathy leading to possible cardiac arrest.[8] Mutations that cause EDMD were originally mapped to the X-linked gene *STA* (also known as *EM*) that encodes emerin. Most emerin defects that are associated with this disease are nonsense mutations that produce soluble forms of the protein. The most consistent cellular feature of X-linked EDMD is the loss of emerin from the nuclear periphery through mislocalization of emerin to the cytoplasm. A specific subset of EDMD-causing emerin mutations has been identified, and these mutations do not disrupt emerin stability or nuclear envelope localization. Patients with these mutations show typical (null phenotype) EDMD disease phenotype, yet their mutation disrupts binding to only one or a few binding partners[5]. This finding suggests that EDMD could arise from disruption of protein complexes that may include emerin and lamins. While X-linked EDMD is associated with a mutation in the lamin-associated protein emerin, the autosomal form of EDMD is

associated with missence mutations throughout the *Lmna* exons that result in misfolding or failure of the lamin protein to correctly assemble, leading to partial or complete loss of function.

Limb girdle muscular dystrophy is similar to EDMD, but results in a milder condition and later onset of skeletal myopathy and conduction defects. The distinguishable features of this muscular dystrophy include the absence of early tendon contractures and the predominance of proximal limb weakness.[9] Mutations (e.g. *Lmna* R377H) are present in the rod and carboxy-terminal domains of the *Lmna* A/C gene. Dilated cardiomyopathy (DCM) primarily features ventricular dilations and impaired systole with minimal effects on skeletal muscle[9]. DCM with conduction system disease also arises from mutations distributed throughout the *Lmna* A/C gene, encompassing both the amino- and carboxyl terminal globular domains and the central rod domain. The majority of mutations are inherited as autosomal dominant missense mutations, while some mutations include deletions and nonsense mutations of splicing alterations.

Neuropathy

Impaired A-type lamin function is also linked to an autosomal-recessive axonal neuropathy known as Charcot-Marie-Tooth neuropathy Type 2B1 (CMT2B1). This neuropathy reduces the axon density resulting in demyelinated axons and the wasting of peripheral muscles. CMT2B1 is caused by homozygous recessive missense mutation (substitution of arginine by a cysteine) at R298C in the α-helical rod domain of LMNA [10]. This mutation is thought to perturb lateral interactions between A-type lamins to give a partial loss of function of A-type lamins.

Lipodystrophy

Dunnigan-type Familial Partial Lipodystrophy (FPLD) is characterized by the loss of subcutaneous fat in the limbs and trunk with excessive fat accumulation around the neck and shoulders, leading to a condition known as the 'buffalo hump'. Redistribution of white adipose tissue is apparent after puberty, is particularly striking in women, and leads to hypertriglyceridemia, insulin resistance, and type II diabetes[11]. FPLD is autosomal dominantly inherited with extremely specific mutations, mapping to residues 465, 482 (most frequent), 486 in all A-type lamins or residues 582, or 584 in the lamin A tail[12]. Mandibuloacral dysplasia (MAD) similarly results in redistribution of white adipose tissue as well as bone deformities, craniofacial skeletal defects, predominantly in the jaw, and osteolysis in the tips of the fingers. MAD is inherited in a homozygous recessive (R572H) manner. FPLD and MAD mutations are clustered around residues in the carboxy terminal globular domain. The residues mutated in these two lipodystrophies lie at the surface of the globular domains leading to minimal effects on lamin stability, while those mutations of the muscular laminopathies affect residues at the inside of the globular domain. Mutations in the internal residues result in greater disruption to the lamin structure, affecting the ability of lamins to dimerize with other lamins, and to interact with other nuclear proteins.

Hutchinson-Gilford Progeria Syndrome

One unique rare disease caused by a single heterozygous splicing mutation in the *Lmna* gene is Hutchinson-Gilford Progeria Syndrome. This mutation (C1824 to T1824) results in deletions in the carboxy terminal globular domain and therefore major loss of Lamin A expression.[13] Children with progeria show many features associated with aging and die in their teens (median age of death 13.4 years) from cardiovascular problems due to coronary artery

disease. This disease is characterized by postnatal growth retardation, midface hypoplasia, micrognathia, premature atherosclerosis, absence of subcutaneous fat, alopecia, and generalized osteodysplasia with osteolysis and pathologic fractures,[14] suggesting that A-type lamin integrity is significant to some aspects of the aging process.

1.1.3 Molecular and cellular mechanisms underlying laminopathies

Numerous tissue-specific pathologies arise from the various mutations in the *Lmna* gene. How these different pathologies arise from alterations in the same gene that is ubiquitously expressed is not fully understood.[7] The mechanical stress hypothesis and altered gene hypothesis are two theories proposed to explain the underlying cause of these laminopathies. The mechanical stress hypothesis conjectures that mutations in A-type lamins affect the structural integrity of the nucleus resulting in a greater susceptibility to physical stress. The nuclear fragility contributes to the pathologies subjected to mechanical stresses where the contractile forces of skeletal and cardiac muscles rupture weaker nuclei. Mechanical strain may also disrupt the interaction of lamins and their binding partners linking them to chromatin or the cytoskeleton. The altered gene hypothesis proposes that the loss of Lamin A/C from the nuclear lamina and the inside of nucleus affects chromatin organization and transcriptional regulation of gene expression.[12] Many proteins associated with the nuclear envelope are directly or indirectly involved in chromatin organization, transcription and binding to DNA. These two hypotheses have been the key ideas in many of the experimental studies designed to understand the underlying pathway of the laminopathies.

1.1.4 Mechanotransduction

Mechanotransduction is the process by which cells transduce mechanical stimuli into biochemical signals and is found in almost all cell and tissue types. Mechanotransduction plays an essential role in maintaining physiological cell function and has many important implications in physiology, medicine, and medical device design. Mechanotransduction is seen in many cellular functions such as hypertrophy, bone regeneration, atherosclerosis due to shear forces on the vascular lining, and in controlling apoptosis.

NF-κB, one of many mechanical stress-responsive transcription factors, can function as an anti-apoptotic signal. Impaired transcriptional activation can therefore lead to increased apoptosis in mechanically strained tissue. Biomechanical signaling through NF-κB can be observed through early response gene *(iex-1)*, an NF-κB dependent survival gene[15]. In resting cells, NF-κB is sequestered in the cytoplasm by the inhibitor IκB. Upon stimulation, IκB is ubiquinated and degraded, allowing NF-κB to translocate into the nucleus and to activate target genes. *Iex-1* gene expression in response to mechanical stimulation seems to be strictly controlled by NF-κB, since overexpression of IκB, totally abolishes the biomechanical induction of *iex-1*. The mitogen activated protein kinase (MAPK) ERK 1/2 is an important regulator for mechanically induced gene expression and has been linked to NF-κB activation as well.[16]

1.1.5 Thesis Objective

Lmna null mice have been genetically engineered by deleting a region extending from exon 8 to the middle of exon 11 and introducing the deletion into ES cells by homologous recombination [17]. Heterozygotes were intercrossed to derive viable homozygous offspring. At birth, *Lmna* null mice were indistinguishable from their heterozygous or wild-type siblings. However, within 2–3 weeks a reduction in their growth rate was noted and by ~4 weeks, despite normal tooth development and the continued ability to eat, their growth had ceased. At this time their mean body weight was roughly 50% that of their wild-type or heterozygous littermates. At ~3–4 wk, the homozygotes began to display an abnormal gait with a stiff walking posture, characterized by splayed hind legs and an inability to hang onto structures with their forepaws. Their overall posture became progressively more hunched, exhibiting distinct scoliosis/kyphosis. By the eighth week, all of the homozygotes had died. In contrast, heterozygotes were apparently normal and did not exhibit any premature mortality when compared with wild type litter mates. Overall, $Lmna^{-/-}$ mice develop cardiac and skeletal myopathy bearing a striking resemblance to human EDMD [18]. Genetically engineered *EM* null mice have been created by the same group (Colin Stewart, NCI) and are currently under investigation. However, emerin null mice do not display any overt phenotypes associated with EDMD. Preliminary data indicate that older *EM* null mice had impaired regeneration of muscle, but otherwise showed no other phenotypes (personal communication with Colin Stewart).

Here, we explore the role of emerin in mechanotransduction and EDMD through the study of nuclear mechanical properties, cytoskeletal stiffness, and mechanical strain-induced signaling in $Lmna^{-/-}$ and $EM^{-/y}$ mouse embryo fibroblasts.

1.2 MATERIALS and METHODS

Cells. *Lmna*$^{+/+}$, *Lmna*$^{-/-}$, *EM* $^{+/y}$, *and EM* $^{-/y}$ mouse embryo fibroblasts were maintained in Dulbecco's Modified Essential Medium (Invitrogen, Carlsbad, CA) containing10% fetal calf serum (HyClone, Logan, UT) and penicillin/streptomycin (Invitrogen) at 37°C in 5% CO_2 humidification.

Nuclear Strain Experiments. Cells were plated at a density of 900 cells/cm^2 on fibronectin (BD, Bedford, MA) coated silicon membranes in DMEM with 10% FCS and penicillin/streptomycin (P/S). The cells were then starved for 48 h in DMEM with P/S and ITS supplement (Sigma, St. Louis, MO). For nuclear analysis, cells were incubated with Hoechst 33342 nuclear stain (1 μg/ml, Molecular Probes, Eugene, OR) in DMEM + ITS for 20 minutes prior to straining the cells. Membranes were placed on a custom-made strain device (see Appendix A for design) mounted on an Olympus IX-70 microscope and biaxial strain was applied in a stepwise fashion. Membrane and nuclear strains were computed on brightfield and fluorescence images using a custom written image analysis algorithm.[19] Normalized nuclear strain was defined as the ratio of nuclear strain to membrane strain to compensate for small variations in applied membrane strain (range 4.58% - 5.68% for primary cells; 17.4 -19.8 % for transformed cells).

Magnetic bead microrheology. Cells were plated on 35 mm polystyrene dishes (Corning, Corning, NY) then incubated with fibronectin coated paramagnetic beads (Dynal Biotech, Lake Success, NY) for 30 min the following day. To minimize nuclear effects, only beads attached more than 5 μm from the nucleus were selected for analysis. A sinusoidal force (amplitude 0.6 nN, 1 Hz, offset 0.6 nN) was applied through a magnetic trap and bead displacement was monitored using a digital camera (Roper Scientific, San Diego, CA). Displacement amplitudes were computed using custom-written MATLAB (Mathworks) algorithms [19]. The applied force as a function of current and distance from the magnetic trap was then computed based on Stoke's Law.

Microinjection. Cells were plated on fibronectin coated glass dishes (WillCo Wells, Amsterdam, Netherlands) or silicon dishes and incubated overnight. Microinjections were performed using an Eppendorf microinjector (Eppendorf, Hamburg, Germany) with Eppendorf Femtotips. In each dish, 20-50 cells were injected with TexasRed-labeled 70 kDa Dextran (Molecular Probes, dissolved at 10 mg/ml in PBS (Invitrogen)) into the cytoplasm (500 hPa, 0.6 sec) or into the nucleus (10, 100, 500, and 1500 hPa, 0.6 sec). Following the microinjection, cells were washed in HBSS (Invitrogen) and intracellular localization of Dextran-TexasRed was recorded under a fluorescent microscope. Experiments were performed by Jan Lammerding.

Strain experiments. Cells were plated on fibronectin-coated silicon membranes (3,500-5,500 cells /cm^2). After 72 h serum starvation, cells were subjected to biaxial cyclic strain (4%, 1 Hz). For chemical stimulation, cells were incubated with IL-1β (10 ng/ml, R&D Systems, Minneapolis, MN) or PMA (200 ng/ml, Sigma) in DMEM + ITS for 2 hours prior to harvest.

Flow cytometry. For cell viability assays, propidium iodide (PI, Sigma, 2 μg/ml) was added to the dishes after 24 h strain application. Cells were collected and analyzed using a Cytomics FC 500 flow cytometer (Beckman Coulter, Fullerton, CA), counting 10-30,000 events in each group. Thresholds for PI incorporation were determined based on negative (no PI staining) and positive (cells permeabilized by 50% ethanol) controls. Apoptotic and necrotic cell fractions were measured in similar experiments through permeabilization of cells through 70% ethanol and staining with Hoechst, PI, and the Vybrant Apoptosis Assay Kit #3 (Molecular Probes).

Northern analysis. For Northern analysis of *iex-1*, *egr-1*, *GAPDH,* and *txnip* mRNA, cells were prepared for strain experiments with 2 hour and 4 hour biaxial cyclic strain. Cells were harvested using RNAeasy Mini Kit kit (Qiagen). 7-12 μg of each collected RNA sample were separated by gel electrophoresis at 110-130 Volts and mRNA was then transferred overnight to a transfer membrane (MAGNA, Nylon, 0.45 micron, Osmonics, Inc.). The mRNA on the transfer membrane was then crosslinked and prehybridized with QuikHyb (Stratagene). The cDNA probe was labeled with P^{32} using a Random Primer labeling Kit (Primer-It II, Stratagene, Cedar Creek, TX). The membrane was then labeled with 10,000,000-15,000,000 counts per minute of cDNA probe.

Real Time Polymerase Chain Reaction. For further analysis of *iex-1*, cells were prepared for strain experiments with 2 hour and 4 hour biaxial strain. Cells were harvested using Qiagen RNAeasy kit. 1 μl of collected RNA was added to RT Mixes of Stratagene Light Cycler kit with *iex-1* and *β-tubulin* primers from Integrated DNA Technologies, Inc (see Appendix C for sequence). The polymerase reaction was conducted in Roche Molecular Biochemicals Light Cycler Version 5.32 with 45 cycles. The results were normalized with *β-tubulin* expression.

Luciferase experiments. Cells were transfected with plasmids for NF-κB-controlled luciferase expression and SV40-regulated β-galactosidase (Promega, Madison, WI) using GeneJammer (Stratagene). Following transfection, cells were serum starved in DMEM + ITS medium for 48 h, followed by overnight stimulation with IL-1β (10 ng/ml). Luciferase assays were quantified in a Victor2 Multilabel Counter (Perkin Elmer). Results were normalized for β-galactosidase activity and expressed as per cent baseline.

Statistical analysis. All experiments were performed at least three independent times. Data are expressed as mean ± SEM. Statistical analysis was performed using the PRISM 4.0 and INSTAT software (GraphPad, San Diego, CA). The data were analyzed by unpaired t-test (allowing different SD), one-way ANOVA or the Mann-Whitney test in case of non-parametric distribution. A two-tailed P-value of <0.05 was considered significant.

1.3 RESULTS

1.3.1 Nuclear Mechanics

Measurements on nuclear mechanics were obtained by quantifying nuclear deformation with biaxial strain applied to mouse embryonic fibroblasts derived from *EM*$^{-/y}$, *Lmna*$^{-/-}$, and Lmna$^{+/+}$ mice (as controls). Cells were plated on transparent silicone membranes so that the induced biaxial strain is applied to the nucleus through the cytoskeleton and the integrin receptors attached to the silicone membrane. This method of strain induction allows quantitative measurements of nuclear stiffness compared to cytoskeletal stiffness in living cells without having to isolate the nuclei. The induced nuclear deformations were calculated by tracking distinct features in the fluorescently labeled chromatin and normalized to membrane strain to compensate for the small variation in the applied membrane strain. As previously found [19], *Lmna*$^{-/-}$ nuclei showed significantly larger deformations compared to wild type cells at ~ 5% biaxial strain. In contrast, *EM*$^{-/y}$ fibroblasts showed deformations comparable to those of the wild type cells, indicating normal nuclear stability (Figure 1.3a).

Primary cells were found to be more sensitive to nuclear strain. Nuclear detachment in these cells was common during the nuclear strain experiments (Figure 1.3b,c). To prevent further nuclear detachment, the strain application was decreased from the initial application of 20% biaxial strain applied to transformed fibroblasts to 5% biaxial strain. Studies to determine a possible link between nuclear detachment from strain and the null fibroblasts were conducted. However, no correlation (not shown) was found between nuclear detachment during induced strain and genotype.

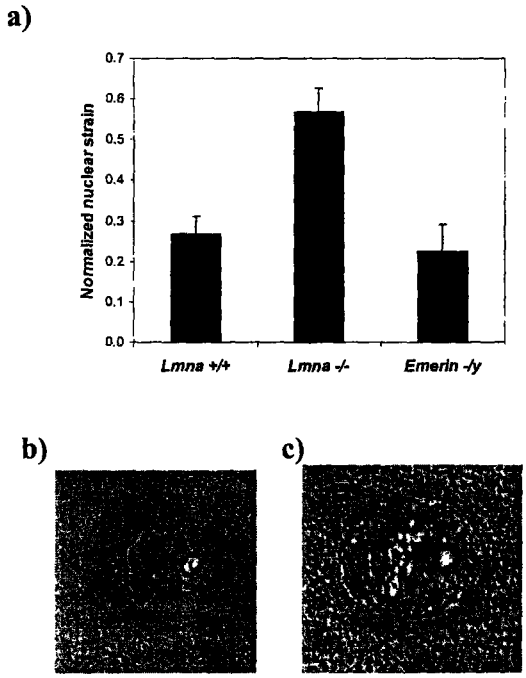

Figure 1.3 Nuclear strain experiments a) *EM*$^{-/y}$ cells showed nuclear strain comparable to wildtype cells under 5% biaxial strain while *Lmna*$^{-/-}$ cells showed significantly increased nuclear strain as previously found [19]. Nuclear detachment of cells was found during nuclear strain experiment with nucleus intact b) prestretch and c) collapsed or detached post-stretch.

1.3.2 Cytoskeletal Mechanics

To evaluate whether altered transmission forces played a role in increased nuclear deformation, magnetic bead microrheology was used to measure the cytoskeletal stiffness of the fibroblasts. Fibronectin-coated paramagnetic beads were attached to the cell (Figure 1.4a) to transmit an applied magnetic force to the cytoskeleton and induced bead displacement amplitude was measured (Figure 1.4b). Induced bead displacement amplitude showed large variations in all three cell types so that no differences in cytoskeletal stiffness were found (Figure 1.4c). Since increased nuclear deformation was not found in the $EM^{-/y}$ fibroblasts, this result supports that the $EM^{-/y}$ cells received similar forces to that of the wildtype. However, the results do differ from Lammerding et al. [19], who reported that $Lmna^{-/-}$ fibroblasts had decreased cytoskeletal stiffness compared to $Lmna^{+/+}$ cells.

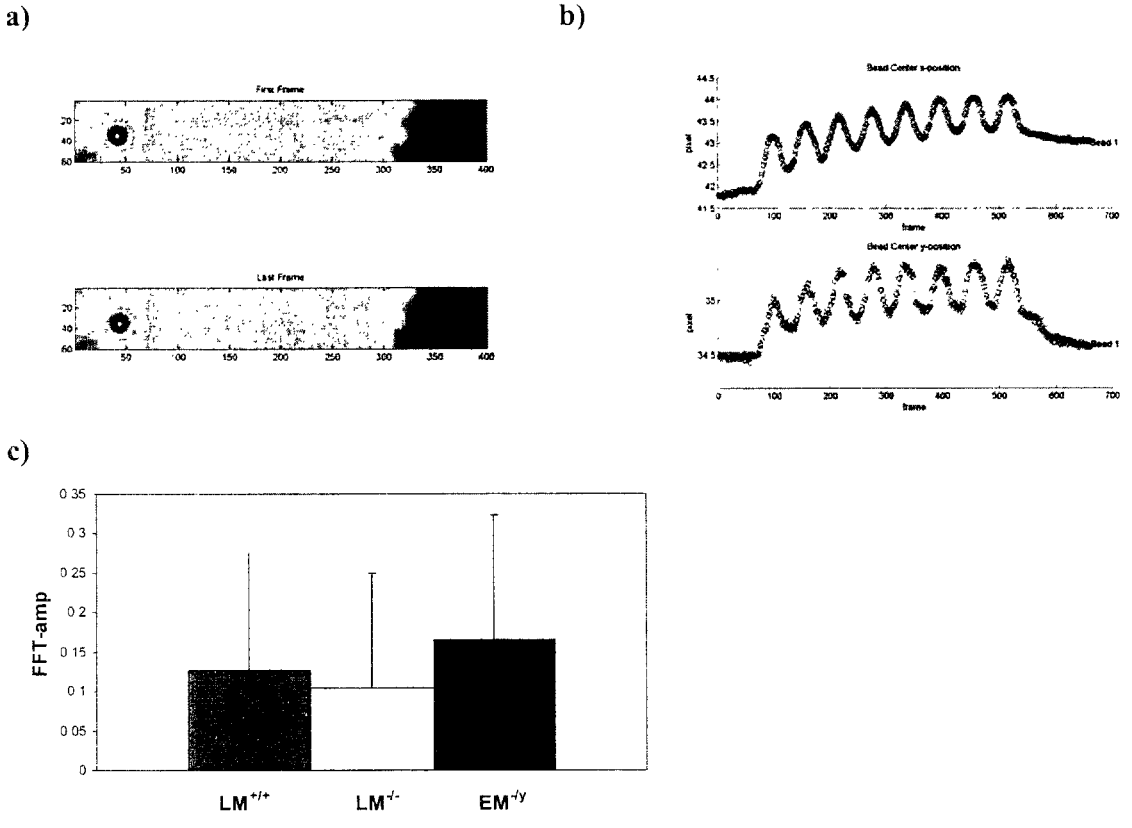

Figure 1.4 Cytoskeletal mechanics using magnetic bead rheology
a) A magnetic bead attached to a cell can be seen at the left of the figure while the magnetic trap tip is visible at the right. b) A graph of bead center x – and y-position showing induced bead displacement amplitude. c) All three cell types showed similar bead displacement amplitude based on Fast-Fourier-Transformation (FFT) analysis, indicating comparable cytoskeletal stiffness.

1.3.3 Mechanical strain induced response

Nuclear integrity may play a significant role in the tissue-specific effects of emerin and lamin A/C mutations in various laminopathies. Microinjection of fluorescently labeled 70 kDa dextran into the cytoplasm or nucleus of the fibroblast cells allows to examine the nuclear

envelope integrity, as the large dextran molecules can not cross the intact nuclear envelope. In an intact nucleus, dextran should stay within the cytoplasm during cytoplasmic microinjection. On the other hand, a damaged nuclear envelope would allow diffusion of dextran into the nucleus following cytoplasmic microinjection. Similarly, an intact nucleus should retain dextran following nuclear microinjection, while a more fragile nucleus could rupture during nuclear microinjection and allow dextran to leak out into the cytoplasm.

Following cytoplasmic microinjection, wild type, emerin deficient, and lamin A/C deficient cells showed a high percentage of intact nuclei (Figure 1.5d). At a medium injection pressure of 500 hPa, high molecular weight dextran was excluded from the nucleus during cytoplasmic injection (Figure 1.5a) indicating intact nuclear integrity under resting conditions. During nuclear microinjection, dextran was visibly limited to the nucleus in most *Lmna*$^{+/+}$ and *EM*$^{-/y}$ cells when injected at 500 hPa (Figure 1.5b). However, when dextran was injected directly into the nucleus at the same pressure, nuclear integrity in most *Lmna*$^{-/-}$ fibroblasts was compromised, resulting in fluorescently labeled dextran escaping into the cytoplasm (Figure 1.5c). In comparison, *Lmna*$^{-/-}$ fibroblasts had a higher percentage of nuclear rupture compared to *EM*$^{-/y}$ and *Lmna*$^{+/+}$ indicating increased nuclear fragility (Figure 1.5e). In contrast, *EM*$^{-/y}$ fibroblasts showed normal nuclear integrity compared to wildtype cells. As expected, nuclear microinjection at sufficiently high pressure (1,500 hPa) showed that nuclei could be ruptured in all three cell types (not shown).

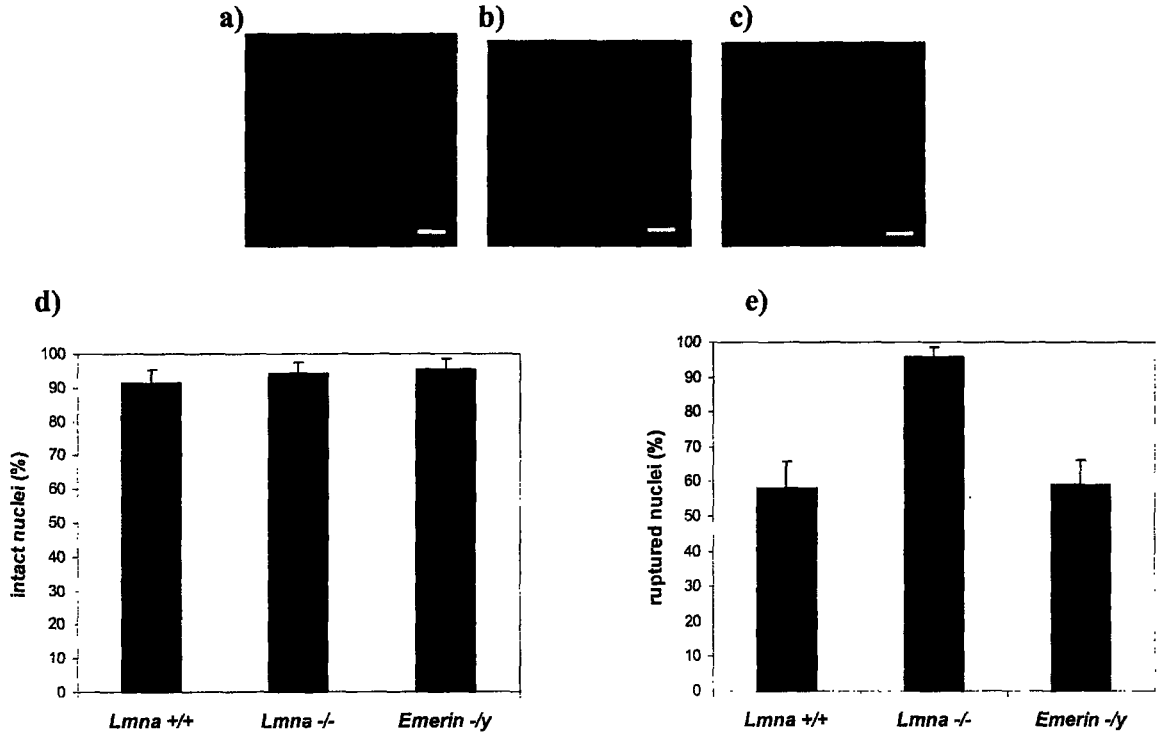

Figure 1.5 Microinjection experiments: a) Dextran was excluded from the nucleus in all three cell types during cytoplasmic microinjection. b) During nuclear microinjection, nuclei in *Lmna*$^{+/+}$ and *EM*$^{-/y}$ cells remained mostly intact and retained dextran. c) *Lmna*$^{-/-}$ cells had more ruptured nuclei during nuclear microinjection, allowing dextran to leak into the cytoplasm. d) Almost all nuclei excluded dextran during cytoplasmic microinjection, regardless of cell type. e) *Lmna*$^{-/-}$ fibroblasts showed a significantly greater percentage of ruptured nuclei during nuclear microinjection, while nuclear integrity of *EM*$^{-/y}$ and *Lmna*$^{+/+}$ fibroblasts was comparable.

1.3.4 Mechanotransduction

Impaired transcriptional activation can lead to an altered physiological response and potentially increased apoptosis in mechanically strained tissue. In normal cells, expression of the mechanosensitive genes *egr-1* and *iex-1* is up-regulated with mechanical stimulation while *txnip* is down-regulated in response to mechanical stimulation. To evaluate whether transcriptional activation was altered for these three genes in lamin A/C or emerin deficient cells, cells were stretched and mRNA levels were subsequently analyzed using Northern analysis and Real Time PCR. The cellular response of *Lmna*$^{-/-}$ and *EM*$^{-/y}$ fibroblasts to mechanical stimulation through expression of the mechanosensitive genes *egr-1*, *iex-1*, and *txnip* revealed attenuated biochemical signaling. Expression of *egr-1*, *iex-1*, and *txnip* in response to mechanical stimulation was impaired in both *Lmna*$^{-/-}$ and *EM*$^{-/y}$ cells at both 2 hours and 4 hours of 4% biaxial cyclic strain (Figure 1.6a). *EM*$^{-/y}$ *and Lmna*$^{-/-}$ fibroblasts showed decreased upregulation of *egr-1* and *iex-1*, and decreased downregulation of *txnip* at 2 and 4 hours of strain (4%) compared to *Lmna*$^{+/+}$ cells(WT). The mechanically unresponsive gene *glyceraldehyde 3-phosphate dehydrogenase* (*GAPDH*) showed unaltered expression among the cell types, suggesting that transcription was not impaired in a nonspecific manner. Impaired cellular response to stimulation of *Lmna*$^{-/-}$ and *EM*$^{-/y}$ cells through expression of *iex-1* was confirmed through Real Time PCR (Figure 3.5b). Notably, *EM*$^{-/y}$ cells showed increased i*ex-1* expression under IL-1β stimulation. This finding has been consistent through Northern analysis (not shown) as well as through Real Time PCR.

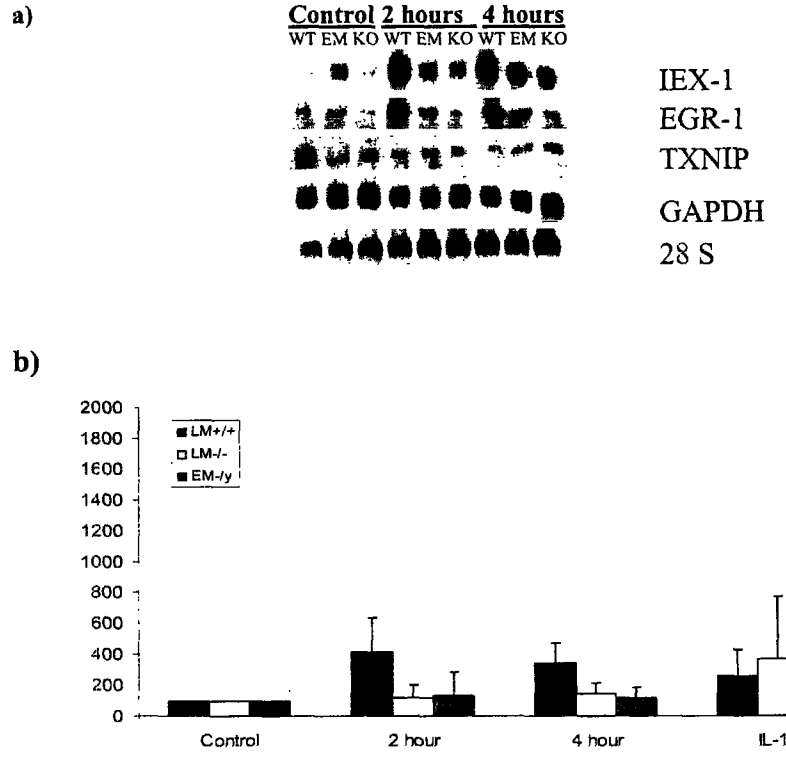

Figure 1.6 a) *EM*$^{-/y}$ *and Lmna*$^{-/-}$ fibroblasts showed decreased upregulation of *egr-1* and *iex-1*, and decreased downregulation of *txnip* at 2 and 4 hours of strain (4%) compared to *Lmna*$^{+/+}$ cells(WT). b) Real Time PCR confirmed impaired transcriptional activation of *iex-1*.

1.3.5 NF-κB signaling

Iex-1 is an NF-κB dependent survival gene and its reduced expression in transcriptional activation may be due to a disturbance in NF-κB signaling, since NF-κB activation is one of the many pathways involved in cellular mechanosensing. Primary cells of *EM* fibroblasts showed high variability in luciferase activity, thus it was difficult to accurately compare NF-κB regulated luciferase activity (Fibure1.7a). IL-1β-induced activity of NF-κB dependent luciferase was impaired in transformed $Lmna^{-/-}$ fibroblasts (also previously found in Lammerding, et al.), but transformed $EM^{-/y}$ fibroblasts showed similar activity to that of the wildtype fibroblasts (Figure 1.7b). These results indicate that NF-κB controlled transcriptional regulation was not affected in $EM^{-/y}$ in response to cytokine stimulation.

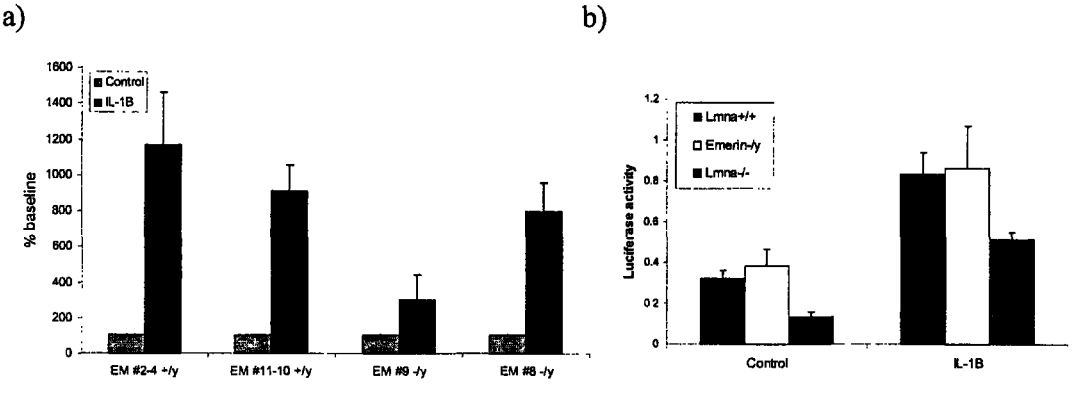

Figure 1.7 a) Primary cells of *EM* fibroblasts showed high variability in luciferase activity, b) NF-κB signaling in transformed EM^{y} cells unimpaired while cytokine-induced NF-κB regulated luciferase activity was significantly impaired in $Lmna^{-/-}$ cells (baseline values: $Lmna^{+/+}$ .322± .042, $Lmna^{-/-}$ .133± .025, $EM^{-/y}$ .384± .080). $Lmna^{-/-}$ fibroblasts showed a significantly lower baseline activity.

1.3.6 Viability Experiments

Viability experiments were conducted to determine the sensitivity of $EM^{-/y}$ fibroblasts to mechanical strain. In the first study, cells were stretched at 5% biaxial strain for 24 hours, harvested, stained with propidium iodide, and analyzed through flow cytometry. Propidium iodide (PI) binds stoichiometrically to double-stranded nucleic acid, allowing fluorescence intensity to be used as an indicator of cellular DNA content. It readily enters and stains nonviable cells, and cannot cross the membrane of viable cells. Figure 1.8b and Figure 1.8c show the negative (no PI) and positive (permeabilized cells) controls for establishing a threshold. However in comparing PI uptake in cells unstretched (Figure 1.8d) and cells stretched at 5% biaxial strain (Figure 1.8e), the thresholds were similar and showed no distinct peaks of viable

and non-viable cells. Instead, in both the control and 5%-strain cells, the two peaks shifted together to form a large peak making it difficult to determine the percentage of PI positive cells.

A similar experiment was conducted to determine the fraction of apoptotic cells in response to 24 hour cyclic strain (5%, 1 Hz). Programmed cell death can be detected by flow cytometry by a characteristic pattern of morphological, biochemical and molecular changes such as of DNA content, altered membrane permeability or the detection of endonucleolysis as characterized by DNA strand breaks. Cells undergoing apoptosis have increased amounts of DNA fragments, resulting in a visible peak in the sub-G1 phase. To determine the percentage of apoptotic cells, PI staining was used to determine the DNA content of the cells through flow cytometry. However, all three cell types showed no statistical differences in the percentage of apoptotic cells (from analysis of the sub-G1 phase) with induced strain (Figure 1.8f). Hydrogen peroxide (H_2O_2) was used as a positive control, yet did not show consistent results, instead showing highly variable apoptotic rates among the cell types. One reason for these inconsistent findings might be that cells transformed to immortalized cells, making it difficult to assess the percentage of apoptotic cells since these transformed cells were likely more sturdy and less sensitive to strain and could continue to proliferate during the 24 h experimental time span.

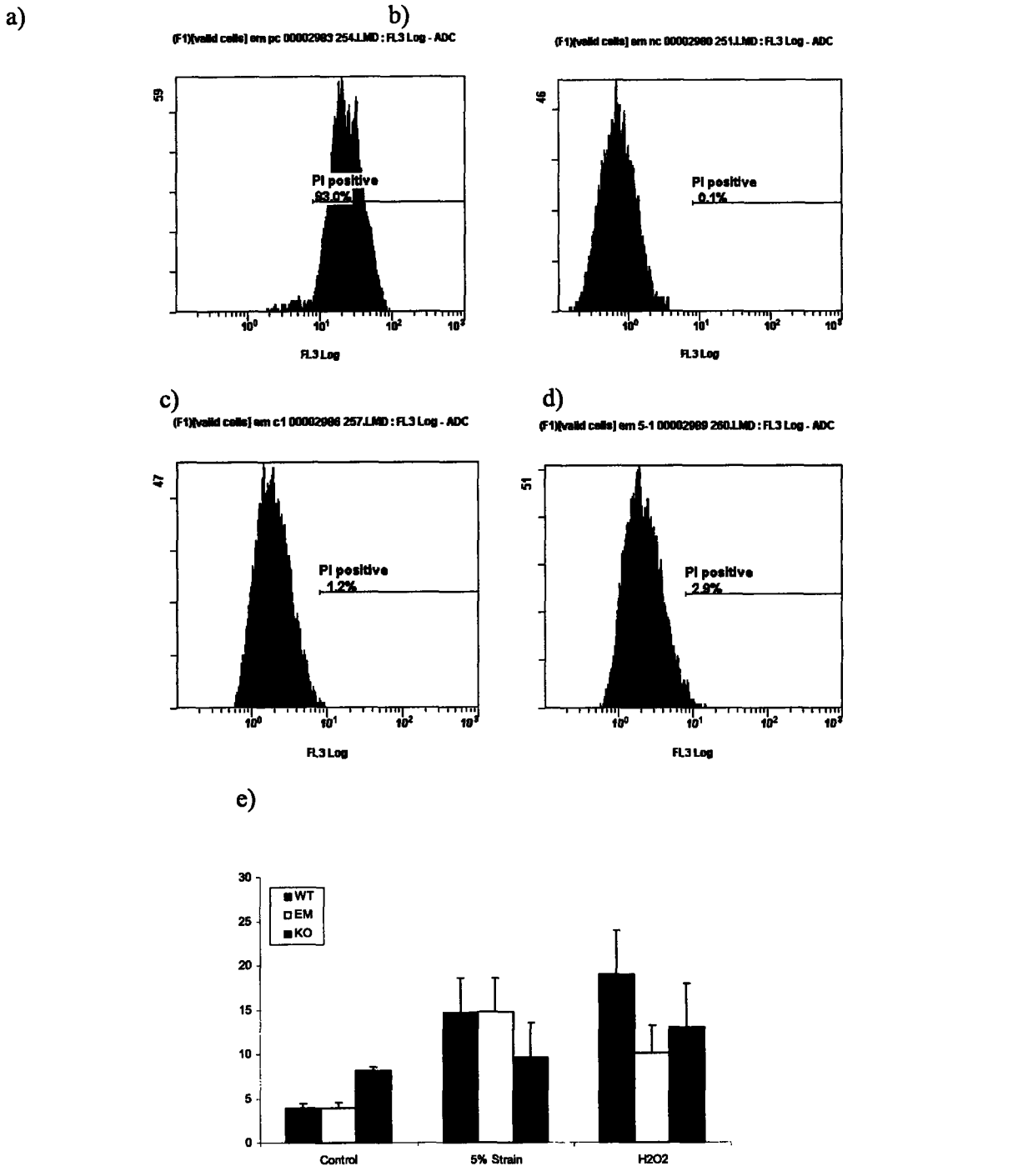

Figure 1.8 Viability Assays using propidium iodide showed no conclusive data to sensitivity to 24 hour cyclic strain among cell types. **a)** Negative control (no PI) and **b)** positive control (permeabilized with 50% ethanol) to establish a threshold. **c)** Control cells and **d)** 5% Biaxial Cyclic strain cells show no distinct peaks for viable and nonviable cells. Instead, the two peaks fell together making it difficult to determine the percentage of non-viable cells. **e)** DNA content analysis showed no statistical difference in the percentage of cells in the sub-G1 phase (apoptotic) between cell types.

1.4 DISCUSSION

The overall goal of this project was to explore the function of emerin in the nuclear envelope and possibly the underlying mechanisms of X-linked and autosomal Emery Dreifuss Muscular Dystrophy. With mutations in both lamin A/C and emerin causing the same phenotype of Emery Dreifuss Muscular Dystrophy, similar functions and regulation pathways were expected between the two proteins. Therefore, many of the experiments were designed to establish whether emerin deficient cells would exhibit similar properties and functions to that of lamin A/C deficient fibroblasts. However, while we confirmed the increased fragility and decreased stiffness of *Lmna*$^{-/-}$ nuclei in primary mouse embryo fibroblasts, we did not observe altered nuclear mechanics in *EM*$^{-/y}$ fibroblasts.

Impaired nuclear integrity can lead to nuclear rupture, cell death, and altered nuclear mechanosensing, contributing to disease phenotypes. Fragmented nuclei have been found in skeletal muscle fibers from emerin-deficient EDMD patients and in fibroblasts from FPLD patients following heat shock treatment [20,21]. In contrast, our studies to examine the nuclear integrity of the *EM*$^{-/y}$ fibroblasts indicated that these cells exhibit nuclear properties comparable to *Lmna*$^{+/+}$ fibroblasts and therefore have apparently normal nuclear mechanics, despite the often irregular nuclear shape. In the nuclear strain experiment, the nuclei of *EM*$^{-/y}$ and *Lmna*$^{+/+}$ fibroblasts showed comparable nuclear strain, while *Lmna*$^{-/-}$ nuclei exhibited more than twice the nuclear strain of the other two cell types. The greater nuclear fragility found in *Lmna*$^{-/-}$ fibroblasts could lead to altered nuclear mechanosensing and impaired mechanotransduction pathways leading to disease. Difficulties arose in this study when studying sensitivity to strain in primary mouse embryo fibroblasts. Large variability and nuclear and partial cytoskeletal detachment were initially found during strain application. Therefore, strain application was reduced from 20% (used in transformed fibroblasts) to 5% strain. Nuclear detachment of the cell types was still occasionally found at this lower strain with the nucleus visibly collapsing within the cytoskeleton and leaving an apparently empty space near the interface of the nucleus and cytoskeleton. In addition, partial cytoskeletal detachment from the silicone membrane resulted in the nucleus collapsing and shrinking in size as the cellular pre-stress was partially released. However, no correlation was found between cell type and percentage of cells with nuclear detachment, indicating that nuclear detachment was likely due to sensitivity of primary cells to strain application and low cell adhesion strength with the fibronectin used.

Microinjection studies were conducted to examine nuclear envelope integrity. Leakage of the large biopolymer dextran into the nucleus during cytoplasmic microinjection or into the cytoskeleton during nuclear microinjection indicated a compromised or ruptured nucleus. During cytoplasmic microinjection, dextran did not leak into the nucleus for all three cell types. The injection pressure of 500 hPa at the cell membrane did not seem to affect the nuclear integrity. However, nuclear microinjection at 500 hPa showed greater nuclear fragility with dextran leaking into the cytoskeleton in *Lmna*$^{-/-}$ cells. These experiments were consistent with the nuclear strain experiments in demonstrating normal nuclear integrity of *EM*$^{-/y}$ fibroblasts where *EM*$^{-/y}$ fibroblasts were seen to have a comparable percentage of ruptured nuclei to wildtype cells during nuclear microinjection. *Lmna*$^{-/-}$ fibroblasts showed a significant increase in ruptured nuclei during nuclear microinjection, indicating compromised nuclear envelope integrity. Only a small number of ruptured nuclei were found in affected muscle tissue in patients suffering from EDMD [20]. This is consistent with the small fraction of *Lmna*$^{-/-}$ and *EM*$^{-/y}$ cells (~ 5%) that exhibited nuclear rupture in our nuclear strain experiments. Additional events are likely required to trigger this specific disease since nuclear integrity is not impaired in *EM*$^{-/y}$ cells. Therefore, impaired

transcription in mechanotransduction signaling is likely the underlying cause of this muscular dystrophy.

The cytoskeletal mechanics experiments were studied in conjunction with the nuclear strain experiments to understand the possible role of the cytoskeleton on nuclear stress and strain. Lammerding et. al found that *Lmna*$^{-/-}$ have decreased cytoskeletal stiffness[19] with increased nuclear deformation with strain. This altered cytoskeletal stiffness could arise as a compensatory mechanism to protect a fragile nucleus. Cytoskeletal mechanics are important in cell shape, migration, and other critical functions such that altered cytoskeletal mechanics may affect these critical functions as well and play an essential role in the pathophysiology of the various laminopathies. In our experiment, induced bead displacement amplitude showed large variations in all three cell types such that insignificant differences in cytoskeletal stiffness were seen. Variability in bead displacement amplitude was likely due to the different adhesion strengths of the fibronectin-coated paramagnetic bead to the cell surface, the different cell surface properties along the cell (location of bead attachment on the surface of the cell - 5 μm away from the nucleus to the peripheral edge of the cell), and the variability in the properties of the primary fibroblasts used. The fibronectin-coated beads often clumped together and would disperse unevenly along the cell. Therefore, possible effects of neighbor beads could have altered the induced bead displacement amplitude. Although the results of unaltered cytoskeletal stiffness for *Lmna*$^{-/-}$ fibroblasts differs from Lammerding et. al [17], the results for *EM*$^{-/y}$ fibroblasts were not surprising since increased nuclear deformations during nuclear strain was not found. Therefore, no cytoskeletal compensation is needed to protect the nucleus of *EM*$^{-/y}$ cells through altered transmission of strain to the nucleus.

Mechanotransduction plays a critical role in the cell survival or many cell types. By translating the mechanical stress into a biochemical signal through transcription pathways, cells are able to respond accordingly to the strain exhibited upon it. Impaired transcriptional activation could therefore lead to increased apoptosis (through NF-κB pathway) in mechanically strained tissue. Kumar et al. demonstrated in *ex vivo* experiments that NF-κB in skeletal muscle fibers was activated in response to mechanical stress and that this activation was altered in *mdx* mice, a model for Duchenne Muscular Dystrophy (DMD), stressing the importance of NF-κB signaling in muscle tissue that is affected most often in laminopathies [22]. Since nuclear fragility was not present in our EM-/y fibroblasts, altered gene expression may be the primary cause for the laminopathies. With the multiple functions and binding factors found in emerin, disrupted transcription in *EM*$^{-/y}$ mice would not be surprising since they show no overt phenotype of EDMD. Tissue specific effects observed in EMDM may thus arise from abnormal transcriptional activation disrupting adaptive and protective pathways. Our results show that the cellular response of *Lmna*$^{-/-}$ and *EM-/y* fibroblasts to mechanical stimulation through expression of the mechanosensitive genes *egr-1*, *iex-1*, and *txnip* was disrupted. Expression of *egr-1* and *iex-1* is up-regulated with mechanical stimulation while *txnip* is down-regulated in response to mechanical stimulation. At 2 hours and 4 hours of 4% biaxial cyclic strain, up-regulation of *egr-1* and *iex-1* was impaired in both *Lmna*$^{-/-}$ and *EM*$^{-/y}$ cells at both with decreased band intensity through Northern analysis. Similarly down-regulation of *txnip* was impaired during 2 and 4 hours of mechanical strain of the mutant cells with slightly greater band intensity than the *Lmna*$^{-/-}$ cells. The mechanically unresponsive gene *glyceraldehyde 3-phosphate dehydrogenase* (*GAPDH*) showed unaltered expression among the cell types, indicating that transcription was likely not impaired in a nonspecific manner. Both *Lmna*$^{-/-}$ and *EM*$^{-/y}$ showed greater i*ex-1* expression under

IL-1β stimulation. This increased cellular response to IL-1β has is likely due to differences in baseline activity under IL-1β stimulation.

Induction of *iex-1* has been shown to be impaired through northern analysis and real time PCR. Since *iex-1* is an NF-κB dependent survival gene, this reduced expression may be due to a disturbance in NF-κB signaling. The NF-κB luciferase studies were conducted to verify a possible disturbance in NF-κB signaling through biochemical signaling of IL-1β. As previously found [19], IL-1β-induced activity of NF-κB dependent luciferase was significantly impaired in *Lmna*$^{-/-}$ fibroblasts. However, *EM*$^{-/y}$ fibroblasts showed similar luciferase activity to that of the wildtype fibroblasts indicating transcriptional regulation was not disrupted in the *EM*$^{-/y}$ fibroblasts. Variability in luciferase expression may be due to low levels of β-galactosidase expression for normalization, low transfection efficiency, and variable response from primary cells found during the study.

Cellular death may result as a response due to mechanical strain and could be the underlying cause of the laminopathies. The viability studies and apoptotic studies were inconclusive with no statistical difference in apoptotic cells and nonviable cells among the three cell types. Eight hour studies to determine possible effects of differences in cell cycle revealed similar percentages of cells in various cell cycle stages. Part of the difficulty in this study was due to the sensitivity and variability of primary cells that lead to cellular changes related to cell transformation. Viability assays would initially show expected peaks through flow cytometry, but as the cells transformed and became more mitotic, the cell cycle phases would change and result in inconclusive data. Another possible cause of inconclusive data could be the length of time the biaxial strain applied. Cells may die within the first few hours of the 24 hour strain period and thus by the time of analysis, cellular DNA may be degraded and unidentifiable by flow cytometry.

1.5 CONCLUSION and OUTLOOK

Our studies suggest that the mechanical stress hypothesis does not apply to the *EM*$^{y-}$ fibroblasts since they exhibited no difference in cell sensitivity, nuclear integrity and cytoskeletal stiffness compared to wildtype cells under stress and strain. Instead, it appears that emerin plays an important role in mechanotransduction, and this loss of function due to emerin mutations could contribute to muscular dystrophy. However, unlike lamin A/C deficient cells, NF-κB activation appeared normal in the emerin deficient cells, suggesting that alternative pathways must be affected by emerin and lamin mutations.

These novel results should prompt further investigation in the underlying cause of EDMD and the role of nuclear envelope proteins in disease. This includes exploring other mutations that result in the phenotype of EDMD to reveal the role and function of emerin. Surprisingly, *EM*$^{-/y}$ mice show no phenotype, and thus application of these experiments performed in this thesis on human *EM*$^{-/y}$ fibroblasts might give different results than those on the mouse cells. Additional experiments can also be designed to investigate the transcriptional pathways of the mechano-sensitive genes *egr-1*, *iex-1*, and *txnip* in more detail. For example, AP-1 activates *egr-1* and disruption in transcriptional activation of this transcription factor could be analyzed similarly through luciferase assays. Exploration of emerin mutations that do not disrupt the stability or

nuclear envelope localization of emerin but disrupt the binding to its partners might further help to clarify the role of emerin in EDMD. In vivo experiments to study mechanotransduction in mice and human muscle may also reveal more factors causing the disease.

In conclusion, our findings indicate that the function of the nuclear envelope proteins must be expanded beyond a mere structural role to that of an active regulator of gene transcription and mechanotransduction, and future experiments will provide new insights into the effect of lamin A/C and emerin mutations on these functions and how they lead to the varied phenotypes observed in laminopathies.

2.0 NUCLEAR STRAIN MODELING

2.1 INTRODUCTION

Nuclear deformation plays an important role in cell motility[23], cell function [24], and diseased states related to cellular morphology [25]. In diseased states, nuclear deformation can occur through external stress transduced from the extracellular matrix through membrane receptors such as integrins to the cytoskeleton and the nucleus of the cell [26]. Therefore, external forces can be directly transferred through the cytoskeleton to the nucleus causing nuclear deformations, and possibly resulting in modulation of gene expression, the nucleus acting as a mechanosensor in mechanotransduction. Transmission of the shear stress signal throughout the vascular endothelial cell involves a complex interplay between cytoskeletal and biochemical elements and results in changes in structure, metabolism, and gene expression.[27]. Osteocytes have been seen to act as mechanoregulator by adjusting the mass and structure of bone in which they are embedded [28].

Previous studies have examined nuclear strain in intact cells. In leukocytes, nuclear strain has been related to cell recovery dynamics [29]. Chondrocyte nuclei have been shown to undergo deformation to a similar degree as the surrounding tissue matrix, suggesting significant strain levels experienced by nuclei [30]. Our nuclear strain experiments show that at identical stress imposed *Lmna* $^{-/-}$ fibroblasts exhibited a strain twice as large as wild type cells whose nuclei are 5-10 times stiffer than the cytoskeleton. However, in each case the deformation of the nucleus was coupled to the deformation of the entire cell, and it was unclear how much stress was placed on the nucleus. The complicated geometry and strain fields within the cell make analytical predictions difficult. To tackle this complexity, numerical models using finite element analysis were used to approximate the cytoskeletal and nuclear stress and strain fields within the fibroblasts during nuclear strain experiments. The present finite element model allows to evaluate the affect of altered nuclear and cytoskeletal stiffness on the effective nuclear stress and strain levels in the nuclear strain experiments.

2.2 METHODS

2.2.1 Model geometry

Model geometry and material properties were based on features of the *Lmna* and *EM* fibroblasts used in the previous studies (see Section 1.2 Materials and Methods). The complex and irregular shape of these cells featuring lamellipodia and filopodia was approximated with three simplified 2-dimensional axisymmetric models. The models constructed include the nucleus and the cytoskeleton as the key features. The simplest model is comprised of a rectangular nucleus embedded in a rectangular cytoskeleton (Figure 2.1a). Fibroblasts have a varying thickness throughout the cell. At the center of the cell, the nucleus makes up approximately half the cell thickness. The thickness decreases significantly along the peripheral edge giving the cell a hill-like shape. To model the cytoskeletal structure of the cell more accurately, the rectangular cell model was modified such that the height decreases linearly halfway through the cell radius giving a sharp corner at the peripheral edge. Although the sharp corner is unrealistic, it unlikely affects the result of stress and strain on the nucleus since little

stress concentrations should be apparent in that region. The nucleus was modeled with a rounded edge to more accurately describe a nucleus within a cell, resulting in model II that includes the modified cytoskeleton with a cylindrical nucleus that has a semi-circular edge (Figure 2.1b). To further analyze the significance of nuclear shape on the nuclear strain level, a third model was developed to include the slanted cytoskeleton shape with the nucleus modeled as an ellipsoid (Figure 2.1c). Consequently, the first model gives the simplest representation of the cell while the third model gives the most accurate representation of the fibroblast used.

Model geometry was based on measurements taken from fibroblasts used in the experiments (see Section 1.3.1 Results - Nuclear Mechanics), resulting in a cell radius of 36 μm, cell height of 10 μm, nuclear diameter of 18 μm, and nuclear height of 5 μm. For the modified cytoskeleton model, the cytoskeletal height decreases linearly halfway through the cell radius giving a 45° along the peripheral edge.

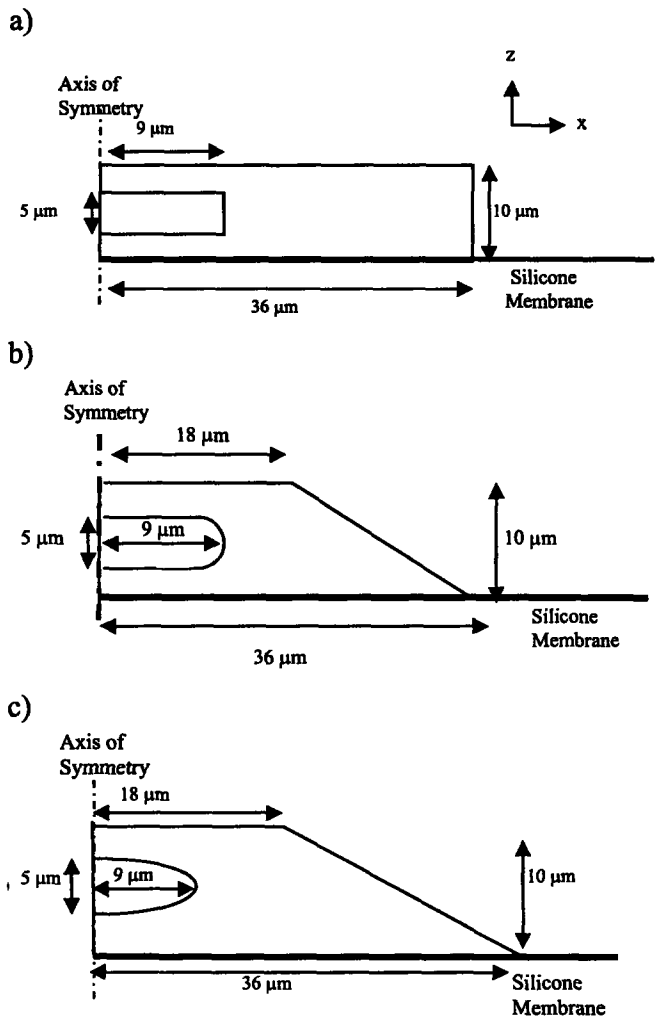

Figure 2.1: Geometry Models
Three axisymmetric models of the cell with cell radius of 36 μm, cell height of 10 μm, a nuclear radius of 9 μm, and a nuclear height of 5 μm. a) The first model has a rectangular nucleus and cytoskeleton b) The second model has a cylindrical nucleus with a rounded edge and a modified cytoskeleton that tapers off at the cell perimeter. c) The third model has an elliptical nucleus and the same modified cytoskeleton as model II.

2.2.2 Boundary Conditions

All models are 2-dimensional and axisymmetric with linear bi-axial strain in the y-direction along the bottom edge of the cytoskeletal structure. Since the model is axisymmetric, a zero Y-translation boundary condition was placed at the center axis of the model to reflect the fixed center of a cell. The fibroblasts of the nuclear strain experiment were plated on a silicone membrane, therefore a zero z-translation boundary condition was placed along the bottom edge of the model to prevent movement in the z-direction.

2.2.3 Mechanical and material properties

To examine the effect of variations in nuclear and cytoskeletal stiffness on nuclear stress and strain, the material properties of these two components were varied. The cytoskeleton was modeled as an incompressible homogenous isotropic Maxwell viscoelastic material with a shear modulus of 100-250 N/m^2 and a bulk modulus to give an incompressible material with a Poisson ratio of 0.499. Normal nuclear stiffness has been found to be 5-10 times stiffer than the cytoskeleton[31] while we assume the lower limit of a soft nucleus approaching cytoskeletal stiffness for pathological conditions. Therefore the nucleus was modeled similarly as an incompressible homogenous isotropic Maxwell viscoelastic material with a shear modulus ranging from 250 N/m^2 to 2500 N/m^2 and a varying bulk modulus to give an incompressible material with a Poisson ratio of 0.499. The equation to determine the bulk modulus is governed by:

$$\nu = \frac{(3K - 2G)}{6K + 2G}$$

where ν is Poisson's ratio, G is the shear modulus, and K is the bulk modulus.

In the following sections, Condition 1 represents normal material properties for the nucleus and cytoskeleton with the lower limit of nuclear stiffness, i.e. the nucleus is ~5-10 times stiffer than the cytoskeleton. Condition 2 represents a hypothetical cell with a very soft nucleus that approaches the stiffness of the cytoskeleton (250 N/m^2) while maintaining normal cytoskeletal (250 N/m^2) material properties. Condition 3 represents material properties found in *Lmna*$^{-/-}$ fibroblasts where both the nucleus (250 N/m^2) and cytoskeleton (100 N/m^2) are softer than normal, suggesting possible cytoskeletal compensation. Condition 4 represents a cell with the upper limit of normal nuclear stiffness, i.e. a hard nucleus (2500 N/m^2) 10 times stiffer than the cytoskeleton and normal (250 N/m^2) cytoskeletal material properties. Finally, condition 5 represents a soft nucleus (500 N/m^2) with a soft cytoskeleton (100 N/m^2), so that the normal ratio of nuclear to cytoskeletal stiffness is maintained (summarized in Table 2.1).

Condition	Element	Shear Modulus (N/m^2)	Bulk Modulus (N/m^2)	Poisson Ratio u	Nuclear to Cytoskeletal Stiffness Ratio	Biological settings	Significance
1	Normal Nucleus	1250	624583.3	0.499	5	*Lmna* $^{+/+}$ fibroblasts	Control
	Normal Cytoskeleton	250	124916.7	0.499			
2	Very Soft Nucleus	250	124916.7	0.499	1		No cytoskeletal compensation
	Normal Cytoskeleton	250	124916.7	0.499			
3	Normal Nucleus	250	124916.7	0.499	2.5	*Lmna* $^{-/-}$ fibroblasts	Cytoskeletal Compensation
	Soft Cytoskeleton	100	49966.67	0.499			
4	Stiff Nucleus	2500	1249167	0.499	10		Upper limit of normal cells (high stiffness ratio)
	Normal Cytoskeleton	250	124916.7	0.499			
5	Soft Nucleus	500	249833.3	0.499	5		Soft nucleus/cytoskeleton with normal stiffness ratio
	Soft Cytoskeleton	100	49966.67	0.499			

Table 2.1 Conditions with varying shear modulus

2.2.4 Applied Strain

To simulate the nuclear strain experiments performed with our *Lmna* and *EM* fibroblasts, the magnitude of applied strain on the models corresponded to the range of typical experimental values of ~5-20% strain found. Therefore 5% strain was applied on the models along the bottom edge of the model to represent the stretch of the silicone membrane. That is, displacement increased linearly with distance from the center to the peripheral edge of the cell. The strain application was step-wise with intracellular stress and strain evaluated one second after application.

Cells adhere to a substrate through adhesion sites that are often located along the peripheral edge of the cell. The applied strain translates to the cell through these adhesion sites. Therefore, to evaluate the effect of force transmission to the nucleus through localized adhesion sites, we created additional models in which the applied displacement was only applied to a localized section of the cell/membrane interface. The size of the effective adhesion section at which displacement was varied from a length equivalent to 10% and 33% of the cell radius, located at the outer periphery of the cell.

2.2.5 Solution Techniques

A finite element model was developed using the commercially available software ADINA V.8.02 (Watertown, MA) to determine the normal and tangential stress along the nuclear-cytoskeletal interface and the effective stress and displacement strain within the cell. The cytoskeletal mesh consisted of 5,667 nodes and the nuclear mesh consisted of 133 to 185 nodes, depending on the nuclear geometry. All finite element nodes associated with the cytoskeletal/nuclear interface were shared to represent the junction between the nucleus and the cytoskeleton. Running the simulation for the model took 5.82 seconds on a 4-processor SGI Origin 2000 computer equipped with 6 GB RAM.

2.3 RESULTS

2.3.1 Geometrical Models

Three different geometrical models were implemented to approximate the fibroblasts geometry used in the nuclear strain experiment (see Section 1.3.1 Results – Nuclear Mechanics). The most simplified representation of the cell was the "rectangular model" with both a rectangular nucleus and cytoskeleton. To model the geometry of the cell more accurately, the cell height was allowed to taper off toward the cell edge halfway though the length of the cell. In addition, the nucleus was modeled with a rounded edge to more accurately describe nuclear shapes found in live cells. This second model will be referred to as the "cylindrical model". A third model was developed that included the modified cytoskeletal shape previously described together with an elliptically shaped nucleus to analyze the effect of nuclear shape on the intracellular stress/strain distribution. The third model will be referred to as the "elliptical model". For all three models, normal nuclear (1250 N/m^2) and cytoskeletal (250 N/m^2) material properties were selected.

Stress and strain distribution

Comparison between the three models revealed that the effective stress and strain distribution in the cytoskeleton did not depend on the cytoskeletal shape selected. Figure 2.2a depicts the effective stress distribution in the cytoskeleton of the rectangular model, revealing that the greatest stress in the cell is found at the outer bottom corner of the cell. The profile throughout the rectangular cytoskeleton showed a decrease in stress towards the top of the cell with the outer top corner showing the least stress. The strain profile revealed compressive strain at a small region near the bottom lateral edge of the rectangular cytoskeleton (Figure 2.4a). The tapered cytoskeletal shape of the cylindrical and elliptical model (Figure 2.2 b,c) showed qualitatively similar cytoskeletal stress profiles despite the different nuclear shape. Cytoskeletal stress also generally decreased towards the top of the cell, but the stress was distributed more evenly throughout the cell than in the rectangular model. Only a very small cytoskeletal region showed extremely low stress (at the top of the cell where the cell begins to taper off), in contrast to the large region in the rectangular model, indicating a more uniform transmission of stress through the cytoskeleton. Regions of highest strain were found in the cytoskeleton surrounding the tip region of the cylindrical and elliptical nucleus (Figure 2.5 b,c).

The effective stress, a scalar measuring shear, on the nucleus of the three models showed similar magnitudes, but different distributions. The rectangular nucleus revealed high stress concentrations at the top and bottom corners on the lateral side of the nucleus (Figure 2.3a). The increase in stress at the edges was likely due to the sharp edges of the rectangular nuclear geometry that concentrated the stress in these small regions. The rectangular nucleus generally showed a nearly uniform strain distribution, but with less strain in the middle region of the nucleus towards the lateral edge (Figure 2.5a). The cylindrical nucleus showed the greatest stress along the bottom region of the nucleus that subsequently decreases linearly to the top edge of the nucleus (Figure 2.3a). The strain placed on the cylindrical nucleus showed higher strain towards the axis of symmetry (center of nucleus) rather than at the tip of the nucleus (Figure 2.5 b). Notably, the greatest strain in the nucleus was not at the same position of greatest stress. The elliptical model showed the most uniform stress profile throughout the whole nucleus. However, increased stress levels giving were found at some nodes at the tip region near the apex (Figure 2.3c). These small, local maxima were likely due to numerical artifacts of the model. The

greatest magnitude of stress in the elliptical model was slightly higher than that of the cylindrical model (104.4 N/m^2 versus 96.98 N/m^2), which were both similarly placed on the bottom tip region of the nucleus (indicated by triangle on figures). Unlike the cylindrical model, the positions of maximal stress and strain coincided in the elliptical model (Figure 2.5c). Overall, the elliptical model had the smallest mean stress and strain compared to the other models (see Table 2.2).

a)

b)

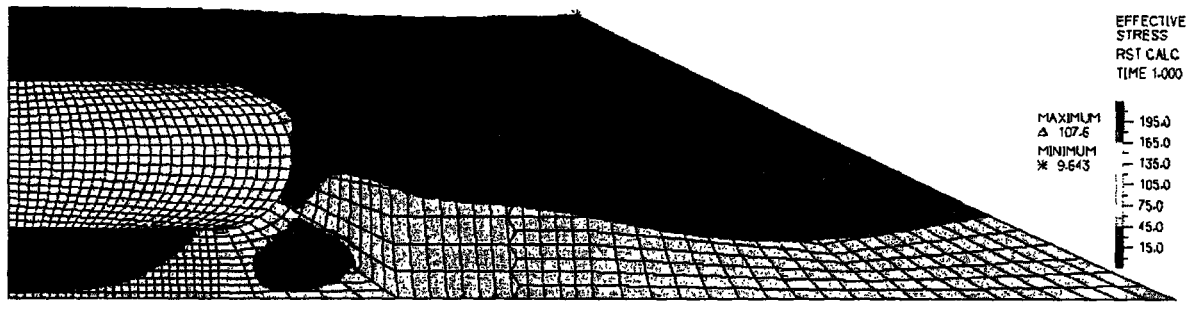

c)

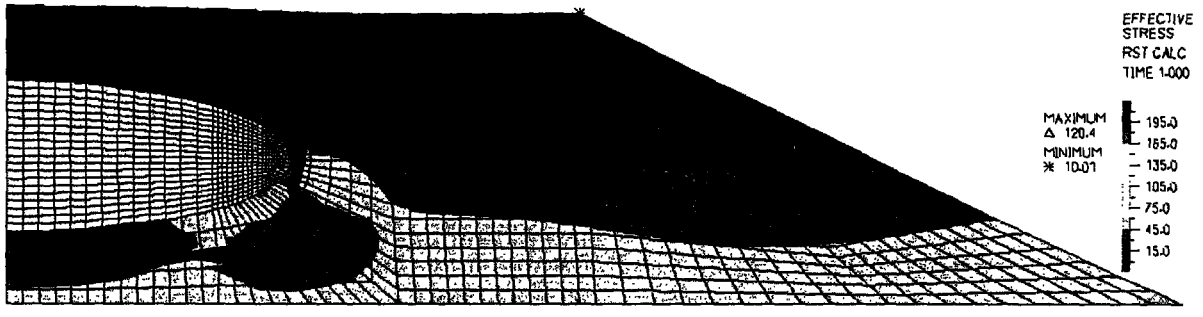

Figure 2.2 Effective stress band plots of a) rectangular model, b) cylindrical model, and c) elliptical model with normal cell material properties (250 Pa – cytoskeleton, 1250 Pa – nucleus).

a)

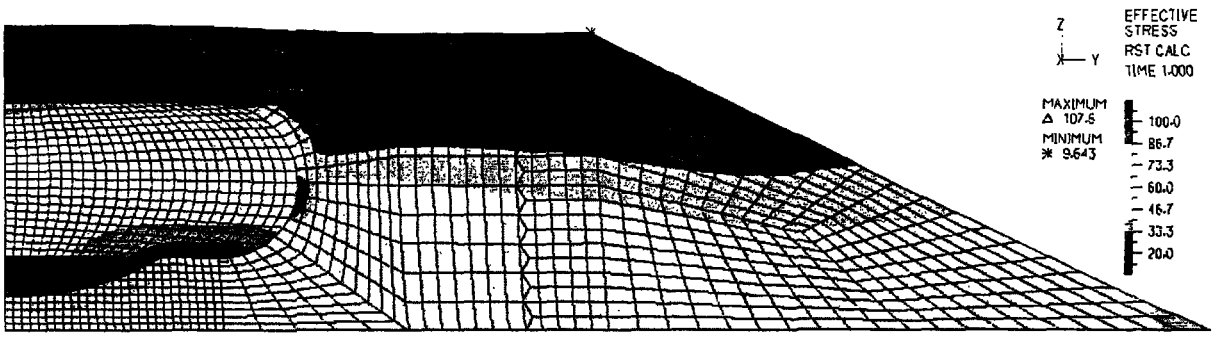

b)

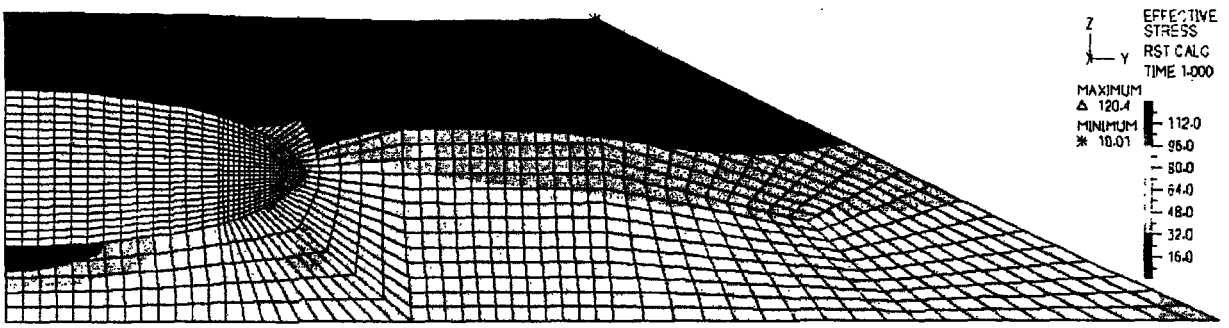

c)

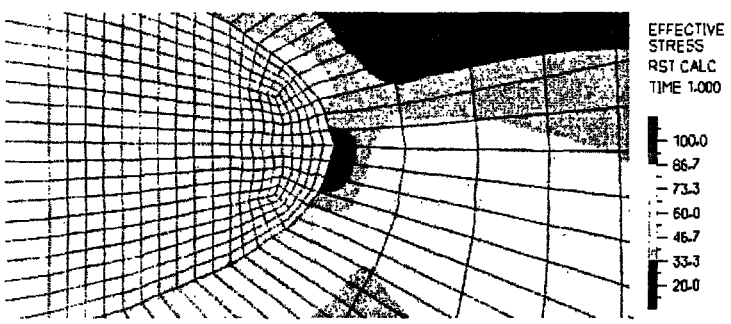

Figure 2.3 More detailed effective stress figures of models

The figures are similar to that of Figure 2.2, but with a rescaled color legend of the effective stress profile of the a) cylindrical and b) elliptical model. c) Peaks of increased stress were apparent along the tip region of the nuclear interface with the maximal stress levels localized at the bottom edge of the nuclear tip region.

a)

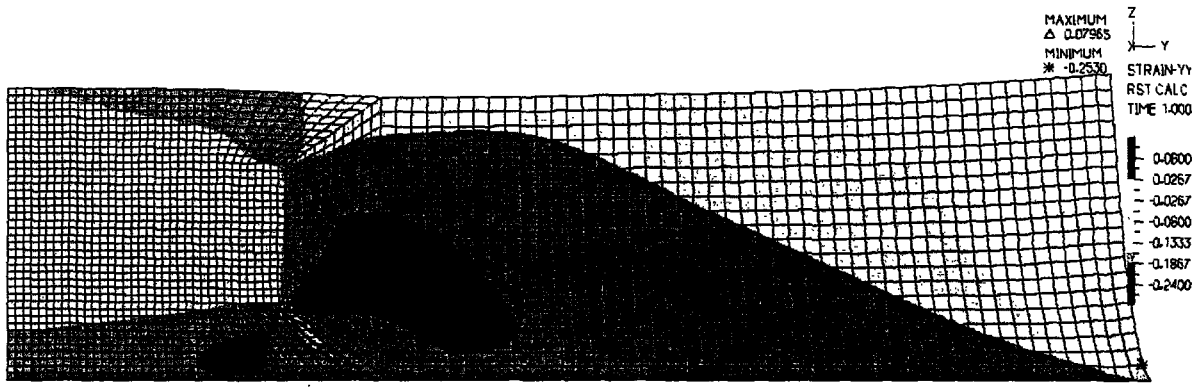

b)

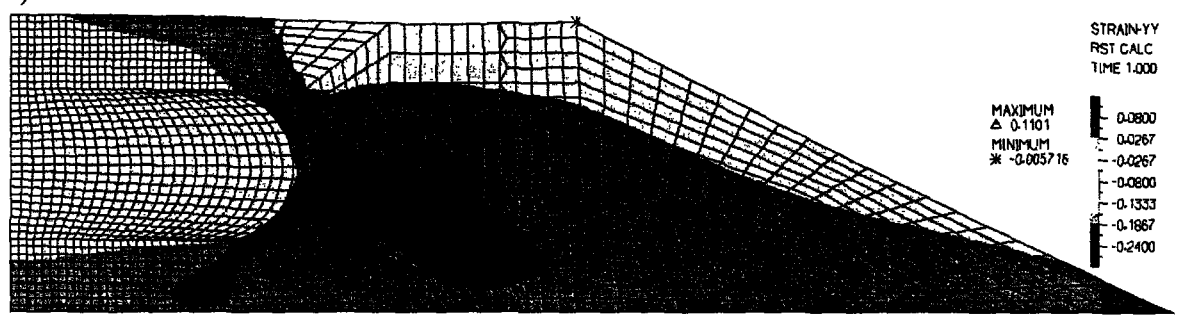

c)

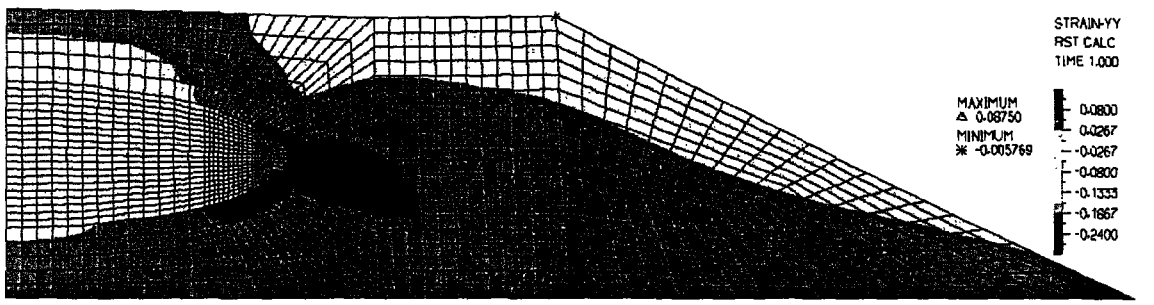

Figure 2.4 Strain YY band plots of a) rectangular model, b) cylindrical model, and c) elliptical model with normal cell material properties (250 Pa – cytoskeleton, 1250 Pa – nucleus).

a)

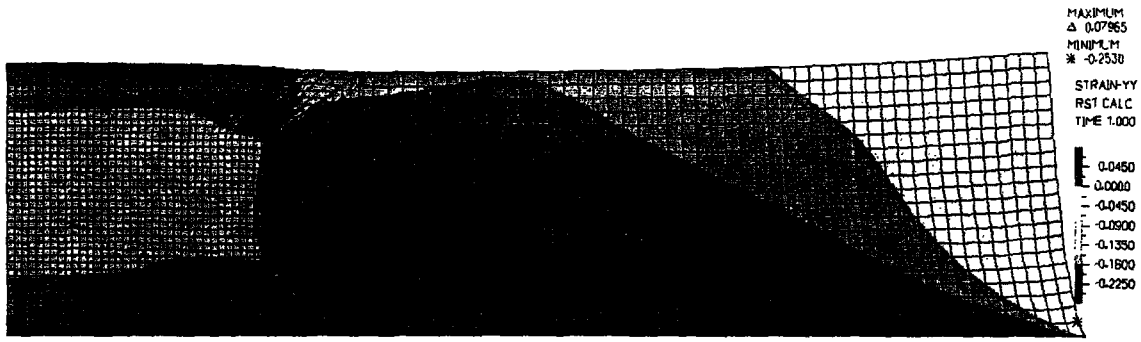

b)

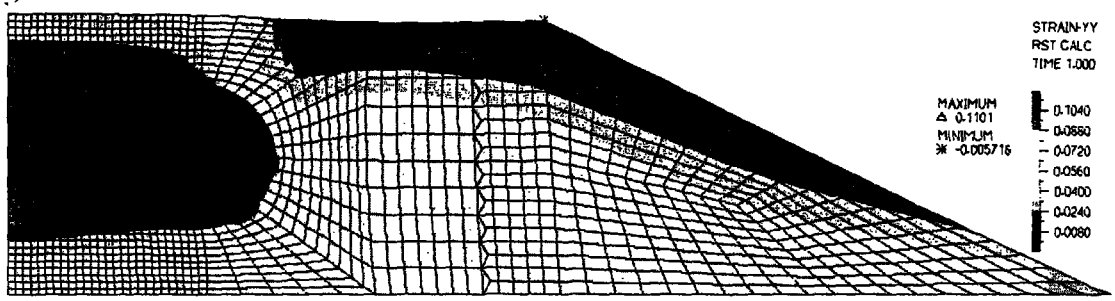

c)

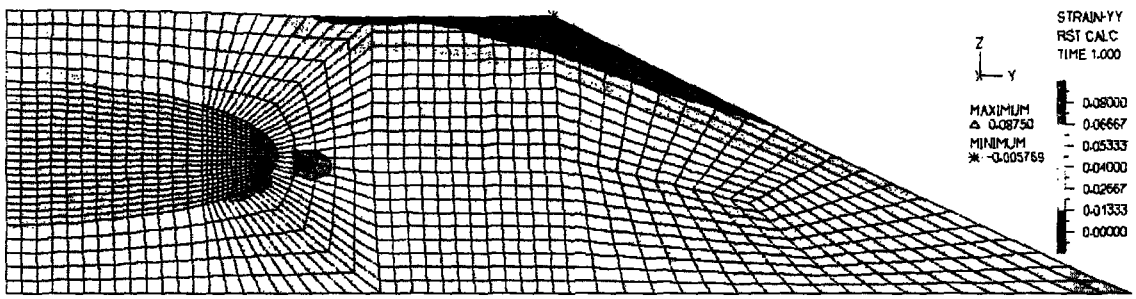

Figure 2.5 More detailed strain-YY figures of models
The figures are similar to that of Figure 2.4, but with a rescaled color legend of the strain profile in the y-direction of the a) cylindrical and b) elliptical model. c) Regions of greater stress were seen around the apex the cylindrical and elliptical nucleus.

Model	Effective Stress (N/m^2)			Strain YY		
	Minimum	Maximum	Node Average	Minimum	Maximum	Node Average
Rectangular	51.1	166.97	85.49	0.011	0.059	0.018
Cylindrical	31.8	104.50	78.80	0.010	0.063	0.017
Elliptical	44.7	102.16	75.89	0.012	0.054	0.016

Table 2.2 Range of stress and strain values in three nuclei of the models at typical nuclear and cytoskeletal properties and same applied stretch on the silicon membrane.

Normal Stress and Strain along Nuclear Interface

To evaluate the role of cytoskeletal and nuclear stiffness on the mechanical load experienced at the nuclear envelope, we plotted the normal and tangential stress and strain components along the nuclear-cytoskeleton interface. The stress or strain at the nodes along the interface was plotted from the top of the nucleus to the tip and down to the bottom edge leading towards the center of the cell (Figures 2.6-2.9, Figure 2.14, and Figure 2.19). The red stars represent nodes along the nuclear interface at the beginning of the tip region, the apex, and the bottom end of the tip region. For the rectangular and cylindrical model for example, the first star is at the top edge with y-coordinates of (6.5, -2.5) while the second star represents the apex of the tip (9,-5) and the third star represents the bottom edge with the coordinates (6.5, -7.5).

In the rectangular model, compressive stress and strain levels were found at the top corner while increased levels of stress was transmitted to the bottom corner of the nucleus lateral edge of the nucleus (Figure 2.6a,b and 2.8a). At the lateral edge, tensile stress and strain along the interface increased at the corners of the nucleus as well. Not surprisingly, the greatest stress and strain normal to the surface was at the corners of the nucleus in the rectangular model.

In the upper flat section of the cylindrical nucleus, small tensile stress was transmitted. Compressive stress at the upper tip region (first star) transitioned to increasing tensile stress until it reached its maximum at the apex (second star in Figure 2.6c,d). Tensile stress decreased along the bottom tip region of the nucleus (third star) until compressive stress dominated along the flat bottom region of the nucleus. Surprisingly, the normal strain along the top edge was compressive when small tensile stress was transmitted along the same area (Figure 2.8b). In the tip region, the cylindrical nucleus showed fluctuations in compressive and tensile strain. Since the normal stress profile was smooth along this region, these fluctuations in strain were likely numerical artifacts in the model. Tensile strain was only along the bottom area of the tip region while the rest of the nuclear interface had compressive strain.

The normal stress on the elliptical nucleus showed a similar profile to the cylindrical model. Since the nucleus has a curved surface, the transition from compressive to tensile stress and vice versa was more gradual. The elliptical model also showed a greater magnitude of tensile stress along the nuclear tip region than the cylindrical nucleus. Since the strain was applied at the bottom edge of the cell, the slower decrease in tensile stress along the bottom edge of the nucleus was consistent with the strain application. Smoothing the normal stress profile using a five-point average showed the similar profiles between the elliptical and cylindrical model (Figure 2.6d,f). The normal strain profile of the elliptical nucleus was similar to the stress profile but with a slower decline in strain along the bottom section of the tip region (Figure 2.8 c,d).

Tangential Shear Stress and Strain along Nuclear Interface

The tangential vector was in the counter-clockwise direction. As a result, the tangential vector was in the opposite direction to the induced strain along the top edge of the nuclear interface of the models giving a negative shear stress in this area. All three models showed similar shear stress and strain profiles (Figure 2.7 and Figure 2.9). Small levels of shear stress and strain at the top edge of the rectangular nucleus increased slowly towards the outer corner edge (Figure 2.7a). Shear stress and strain along the lateral edge should have been close to zero since its tangential direction is normal to the direction of applied strain. However, this model showed a decrease in compressive stress and strain instead. At the bottom corner of the rectangular nucleus, the maximum magnitude of the shear stress and strain of the nuclear

interfaces decreased as it reached the axis of symmetry where the cell was fixed in the y-direction (Figure 2.9a).

The tangential shear stress along the cylindrical nuclear-cytoskeletal interface was small along the top edge. The magnitude of shear stress increased towards the region of the nuclear tip (first star), and slowly decreased to zero at the apex of the cell. After the apex, the shear stress peaked in magnitude and decreased less slowly along the bottom edge as it reached the fixed axis of symmetry (Figure 2.7b). The slow decrease in shear stress along the bottom edge was due to the induced strain placed on the bottom of the cell which transmitted more stress to the bottom of the nucleus. The strain profile of the cylindrical nucleus was less smooth with fluctuating shear strain after the apex and at the lower tip region (Figure 2.9b).

The shear stress along the elliptical nucleus showed a similar profile to the cylindrical nucleus but contained larger variations and localized peaks of high stress near the apex (Figure 2.7c,d, 2.9c,d). Shear stress levels at the top and bottom of the nucleus (outside the region marked by asterisks) were higher compared to the other models, as the top and bottom edges are not flat as in the rectangular and cylindrical nucleus. In contrast, shear strain levels at the top and bottom of the nucleus were considerably lower than in the other models. Smoothing the stress plot using a 5-point average reduces the stress peaks described above and revealed a stress and strain distribution similar to the cylindrical model (Figure 2.7d).

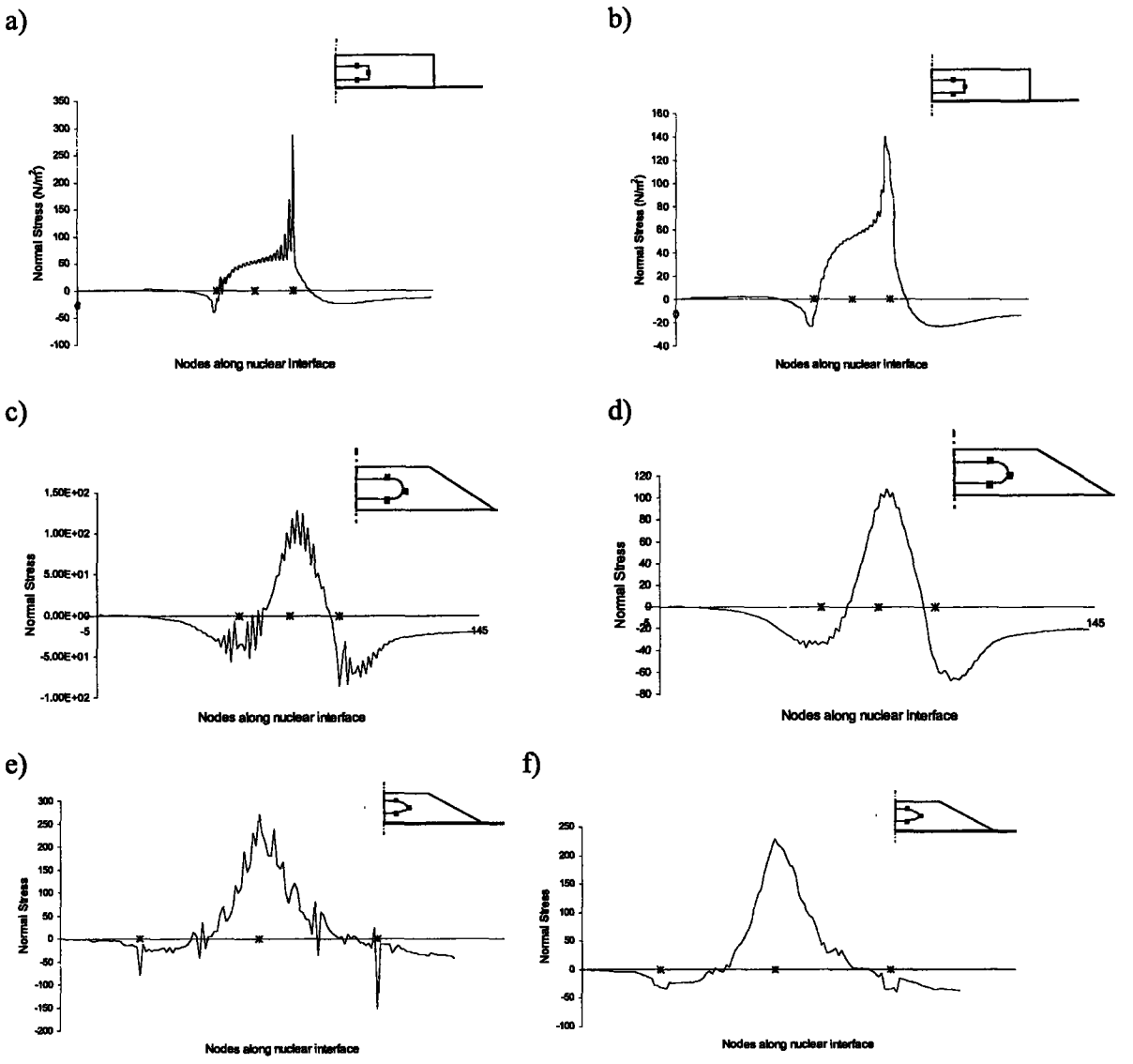

Figure 2.6 Normal Stresses found on a) Rectangular model, b) Rectangular model using Five-point Average c) Cylindrical model, d) Cylindrical model using Five-point Average, e) Elliptical model, f) Elliptical using Five-point-Average. The red stars represent nodes along the nuclear interface at the beginning/top of the tip region, the apex, and the bottom end of the tip region.

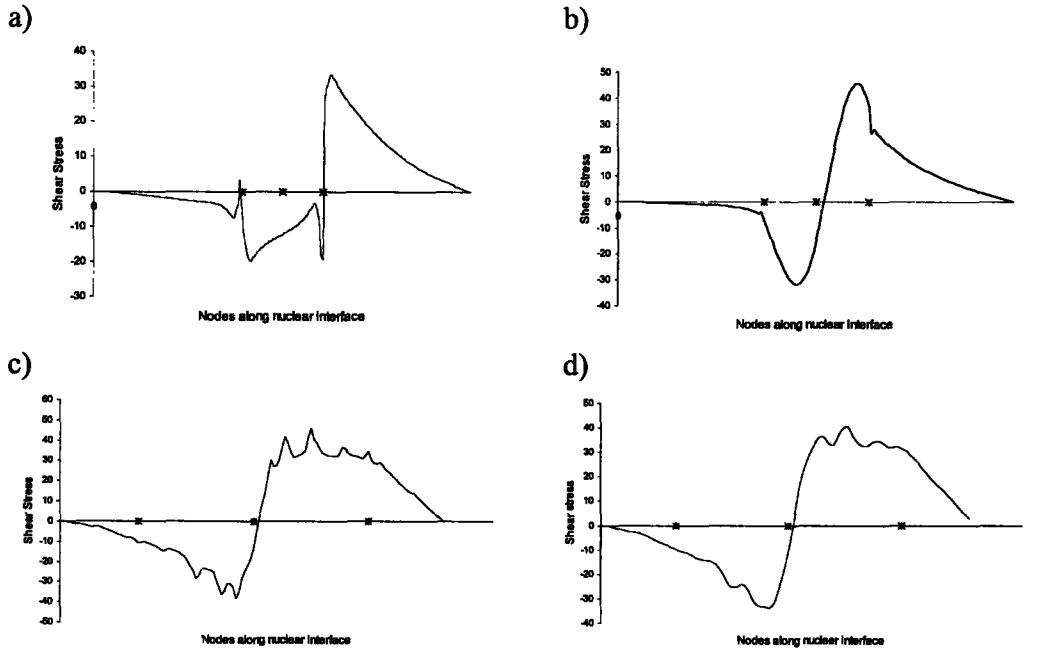

Figure 2.7 Shear Stresses on a) Rectangular b) Cylindrical and c) Elliptical Model. d) Shear stress plot of Elliptical Model smoothed using 5-point-average. The red stars represent nodes along the nuclear interface at the beginning/top of the tip region, the apex, and the bottom end of the tip region.

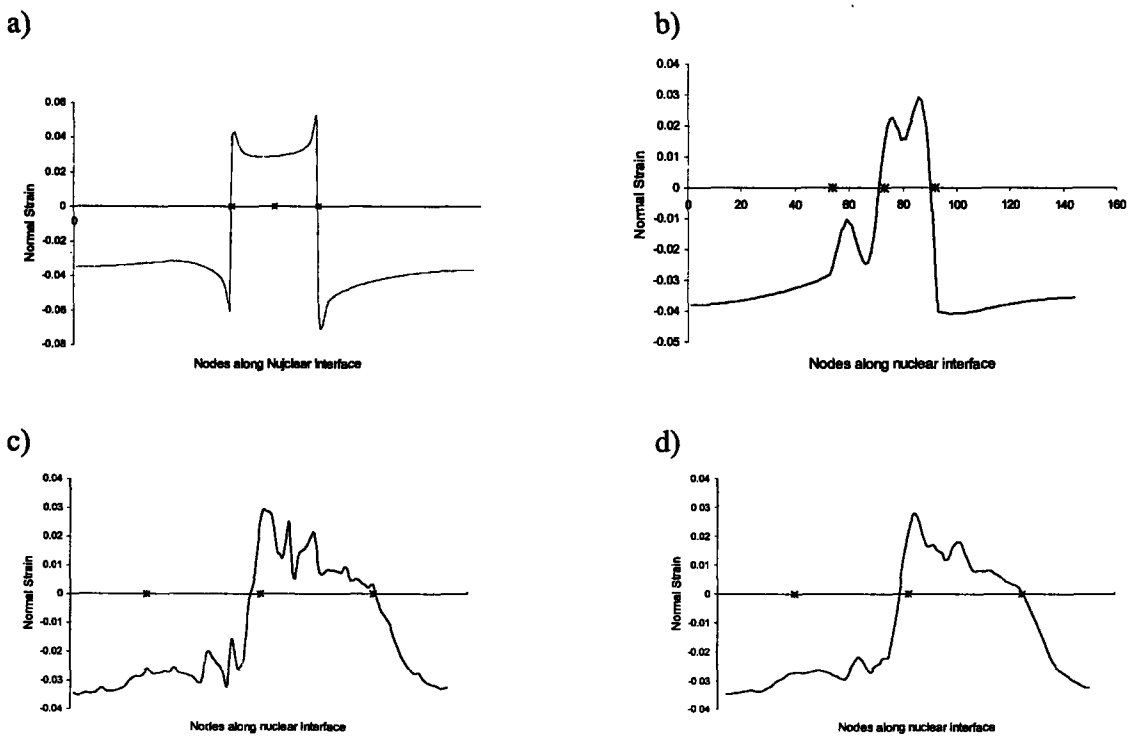

Figure 2.8 Normal strain on a) Rectangular b) Cylindrical and c) Elliptical Model. d) Five nodal point Average on the Elliptical Model

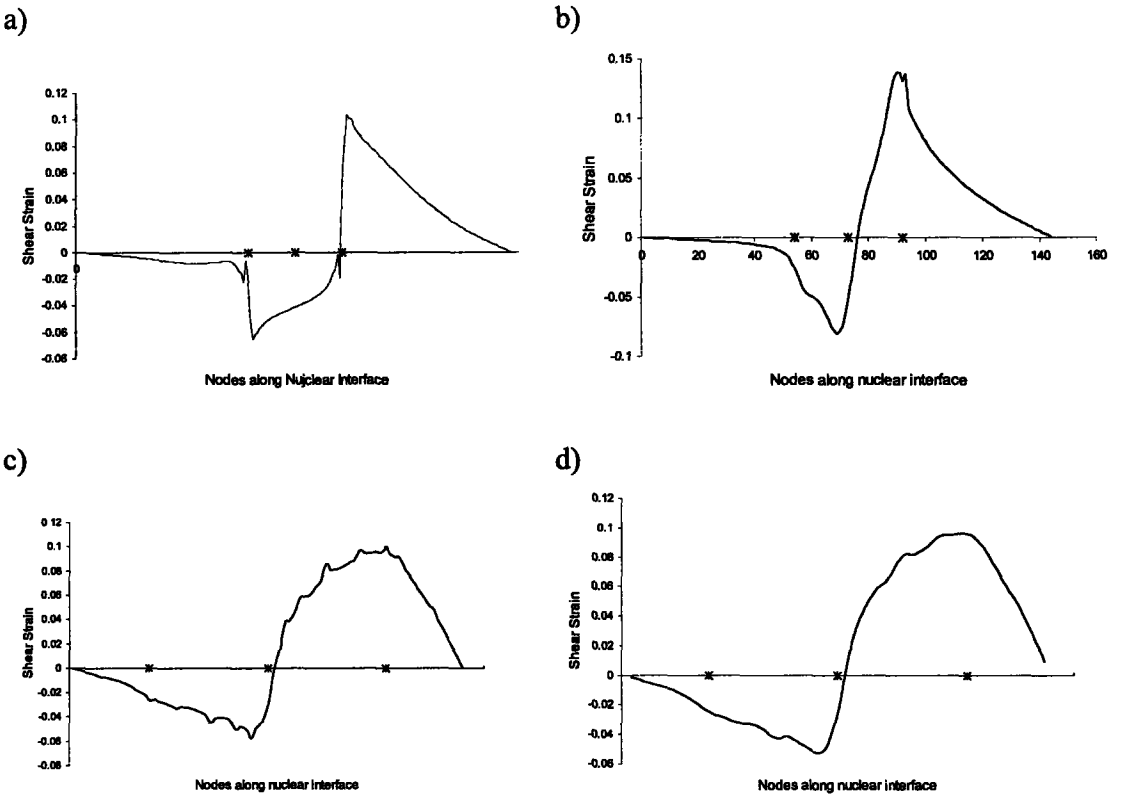

Figure 2.9 Shear Strain on a) Rectangular b) Cylindrical and c) Elliptical Model. d) Tangential strain plot of elliptical model smoothed using 5-point average. The red stars represent nodes along the nuclear interface at the beginning/top of the tip region, the apex, and the bottom end of the tip region.

2.3.2 Variation in cytoskeletal and nuclear stiffness

Subsequently, we examined the effect of variations in nuclear and cytoskeletal stiffness on the stress and strain experienced within the nucleus and at the nuclear/cytoskeletal interface. If the nucleus acts as a mechanosensor in mechanotransduction, altered stress and strain levels at these locations could result in modified gene regulation.

Based on the results of the previous section, we decided to use the elliptical model for subsequent studies as it appears to produce the most physiological stress and strain profiles within the nucleus and cytoskeleton. Although small fluctuations in stress and strain were found at the nuclear interface, these fluctuations were small enough to not affect the general trend of the stress and strain profiles. In addition, the elliptical model most accurately represents the cell geometry found in the fibroblasts used in our experiments. Normal nuclear stiffness has been found to be 5-10 times stiffer than the cytoskeleton. In addition, we also examine pathological conditions with the lower limit of a soft nucleus approaching cytoskeletal stiffness. By changing the nuclear and cytoskeletal stiffness, the effect of nuclear and cytoskeletal stiffness on the intracellular stress and strain distribution can be better evaluated.

Stress distribution

Comparison of the different conditions revealed that the cytoskeletal stress magnitude strongly depends on the cytoskeletal stiffness. This is seen in stress profiles of Condition 1, condition 2, and condition 4, that all have a cytoskeletal stiffness of 250 N/m^2 (Figure 2.10 a-e) resulting in very similar stress magnitudes and profiles. Soft nuclear material properties and small nuclear to cytoskeletal stiffness ratios gave nuclear stress profiles continuous with the cytoskeletal profile. This is seen in Condition 2 and 3 where the nuclei had a stiffness of 250 N/m^2 and a nuclear to cytoskeletal stiffness ratio of 1:1 and 2.5:1, respectively (Figure 2.11 b,c). The nuclear stress profiles in these models decrease in magnitude up the cell like the cytoskeletal stress profile. Condition 3 (soft nucleus, soft cytoskeleton) had a greater nuclear to cytoskeletal stiffness ratio than condition 2, therefore the nucleus had a greater magnitude in stress (Figure 2.10c). The stress profile for Condition 4 showed that more stress was transmitted upon the nucleus for a stiff nucleus (Figure 2.10 a,d). Both condition 1 and 5 had a nuclear to cytoskeletal stiffness ratio of 5:1 but condition 1 had an overall greater stiffness and consequently a greater overall magnitude in stress.

In conditions where the stiffness ratio was 5:1 or higher (conditions 1, 4, and 5), the highest stress was found at the bottom edge of the tip region (represented by a triangle Figure 2.10). In addition, these nuclei exhibited regions of high stress at the nuclear interface (Figure 2.12 a, d, e). Condition 3 had a stiffness ratio of 2.5 and also had high regions of nuclear stress at the interface but to a lesser magnitude (Figure 2.12 c). Therefore, as the stiffness ratio increases, the nuclear profile transitions from the cytoskeletal stress profile to a uniform stress profile with small localized peaks of high stress along the nuclear interface.

Strain distribution

The strain profile and magnitude within the tapered region of the cytoskeleton was similar for all conditions. Interestingly, regions of high strain were present in the cytoskeletal area near the nuclear apex but not at the apex (Figure 2.13). Greater nuclear to cytoskeletal stiffness ratios, resulted in increased magnitudes of strain in these small regions of high strain. When the cell is strained, less stress is transmitted to a stiffer nucleus which then transmits to the cytoskeleton and causes more cytoskeletal deformation. In nuclei that were five to ten times stiffer than the cytoskeleton with normal properties (Conditions 1 and 4), strain within the nucleus was very uniform (Figure 2.13 a,d). For Condition 2, in which nucleus and cytoskeleton share the same material properties, the nuclear strain profile is continuous with the cytoskeletal strain distribution, as we'd expect from a homogeneous material (Figure 2.13b). Condition 3, i.e. the combination of soft nucleus and soft cytoskeleton, leads to generally smaller strain levels at the bottom half of the nucleus but larger variations within the nuclear strain, with increased strain near the nuclear apex (Figure G.1e).

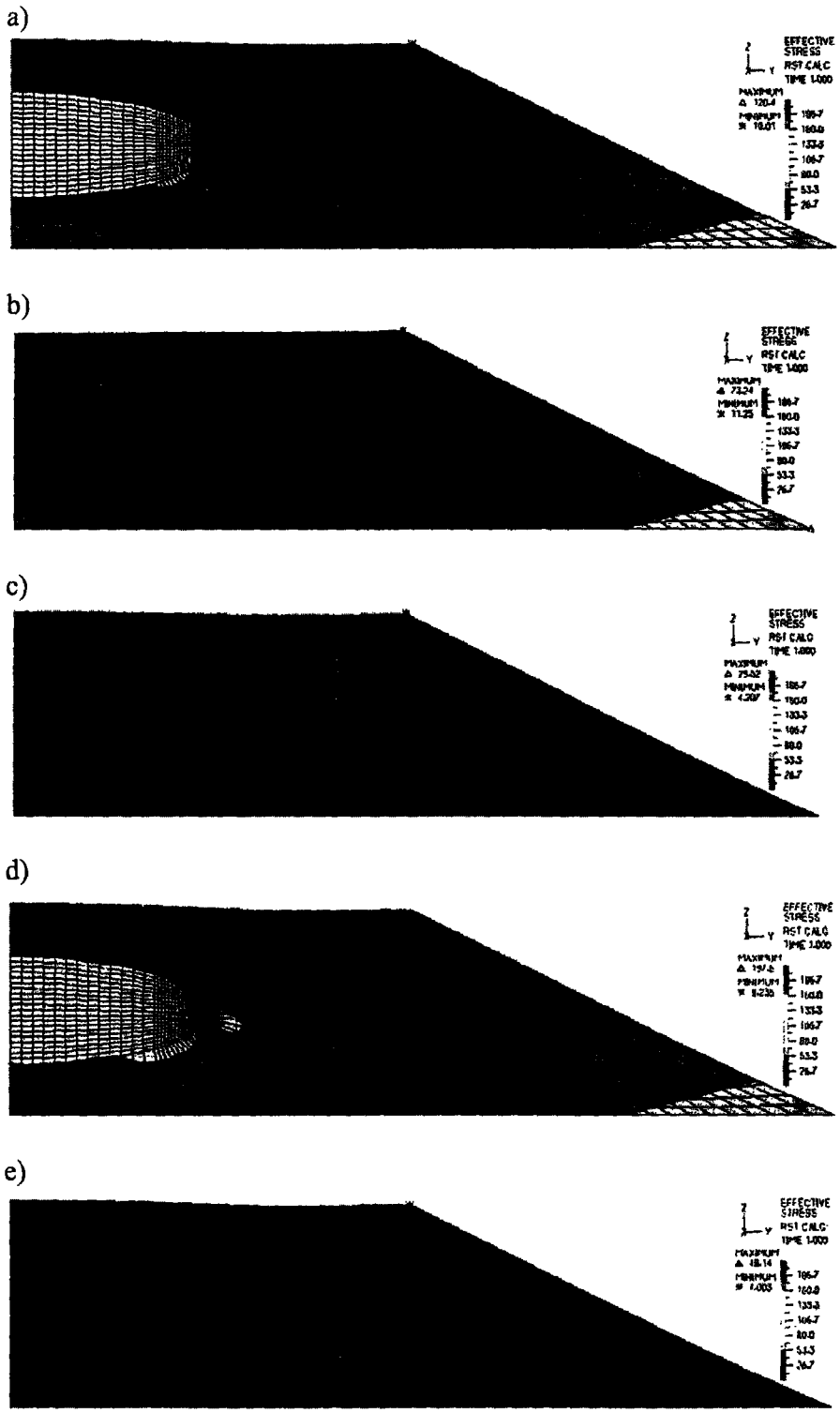

Figure 2.10 Effective stress of elliptical model with various material properties. a) Condition 1 - normal nucleus 1250 N/m^2, normal cytoskeleton 250 N/m^2 b) condition 2 – very soft nucleus 250 N/m^2, normal cytoskeleton 250 N/m^2 c) condition 3 – very soft nucleus 250 N/m^2, soft cytoskeleton 100 N/m^2, d) condition 4 – hard nucleus 2500 N/m^2, normal cytoskeleton 250 N/m^2, e) condition 5 – soft nucleus 500 N/m^2, soft cytoskeleton 100 N/m^2.

a)

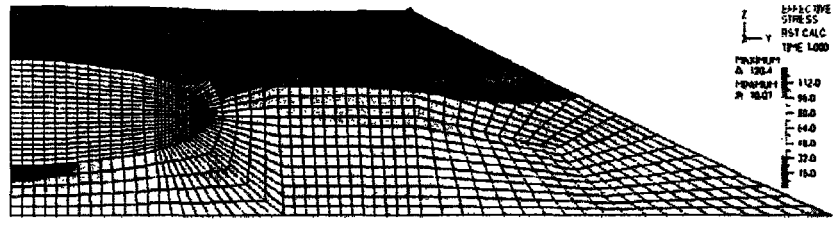

b)

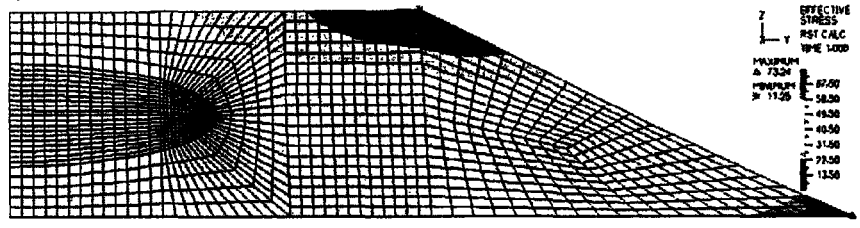

c)

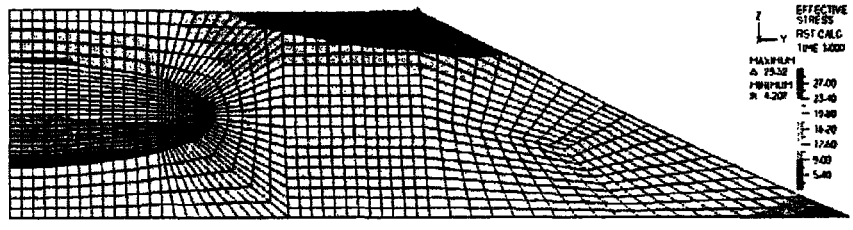

d)

e)

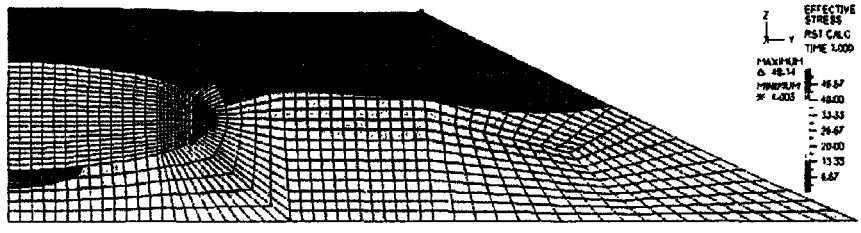

Figure 2.11 Effective Stress profiles of elliptical model with various material properties and scaled individually for more detailed stress profile of a) condition 1 - normal nucleus 1250 N/m^2, normal cytoskeleton 250 N/m^2 b) condition 2 – very soft nucleus 250 N/m^2, normal cytoskeleton 250 N/m^2 c) condition 3 – very soft nucleus 250 N/m^2, soft cytoskeleton 100 N/m^2. d) condition 4 – hard nucleus 2500 N/m^2, normal cytoskeleton 250 N/m^2, e) condition 5 soft nucleus 500 N/m^2, soft cytoskeleton 100 N/m^2.

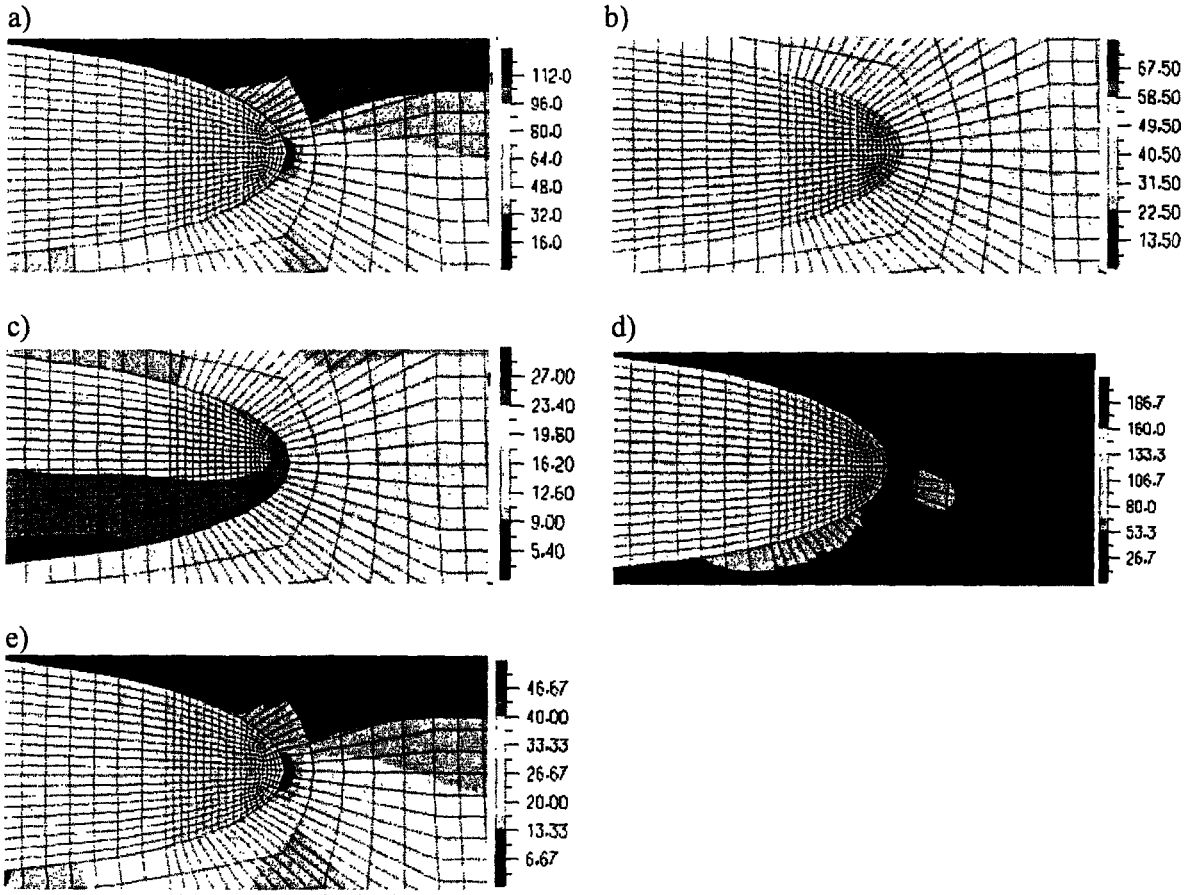

Figure 2.12 Nuclear profiles of effective stress for elliptical model with various material properties and scaled individually for more detailed stress profile of a) condition 1 - normal nucleus 1250 N/m^2, normal cytoskeleton 250 N/m^2 b) condition 2 – very soft nucleus 250 N/m^2, normal cytoskeleton 250 N/m^2 c) condition 3 – very soft nucleus 250 N/m^2, soft cytoskeleton 100 N/m^2, d) condition 4 – hard nucleus 2500 N/m^2, normal cytoskeleton 250 N/m^2, e) condition 5 – soft nucleus 500 N/m^2, soft cytoskeleton 100 N/m^2.

a)

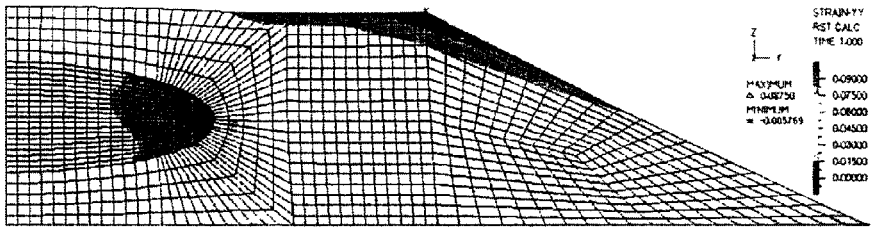

b)

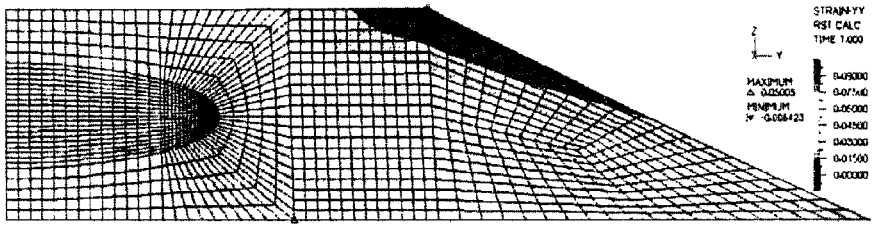

c)

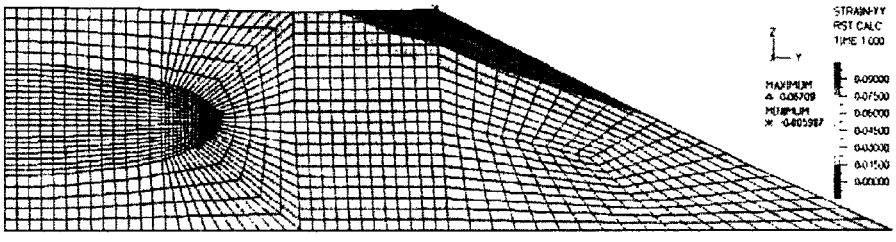

d)

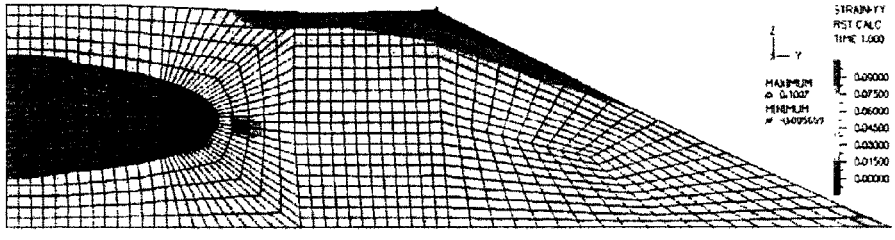

e)

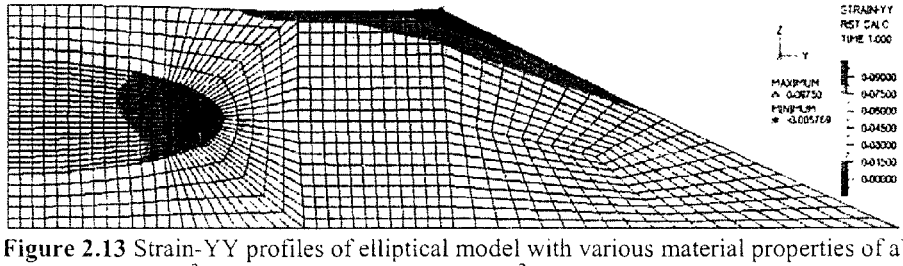

Figure 2.13 Strain-YY profiles of elliptical model with various material properties of a) condition 1 - normal nucleus 1250 N/m^2, normal cytoskeleton 250 N/m^2 b) condition 2 – very soft nucleus 250 N/m^2, normal cytoskeleton 250 N/m^2 c) condition 3 – very soft nucleus 250 N/m^2, soft cytoskeleton 100 N/m^2, d) condition 4 – hard nucleus 2500 N/m^2, normal cytoskeleton 250 N/m^2, e) condition 5 – soft nucleus 500 N/m^2, soft cytoskeleton 100 N/m^2

Normal and Tangential Stress and Strain along the Nuclear Interface

The profiles of the normal stress showed that increased nuclear stiffness leads to increased stress (both tensile and compressive) at the nuclear/cytoskeletal interface (Figure 2.14a). The normal strain profiles revealed that smaller nuclear to cytoskeletal stiffness ratios, resulted in greater magnitudes of normal strain at the nuclear interface. This was supported by the identical magnitude and normal strain profiles of Conditions 1 and 5, which both have a nuclear to cytoskeletal stiffness ratio of 5 but different material properties.

In comparison, the shear stress profiles along the nuclear interface showed that the greater the cytoskeletal stiffness and nuclear to cytoskeletal stiffness ratio, the greater the magnitude of shear stress (Figure 2.14b). Condition 2 (nuclear to cytoskeletal stiffness ratio of 1) had a stress plot line that was greater in magnitude than both condition 5 and 3 (stiffness ratio of 5 and 2.5), therefore the shear stress and magnitude was first dependent on the cytoskeletal stiffness than the nuclear to cytoskeletal stiffness ratio. In contrast, the shear strain showed that higher nuclear to cytoskeletal stiffness ratios resulted in greater magnitudes of shear strain along the nuclear interface (Figure 2.14d). In the case where the stiffness ratio was the same, stiffer material properties would cause an increase in shear strain at the nuclear interface.

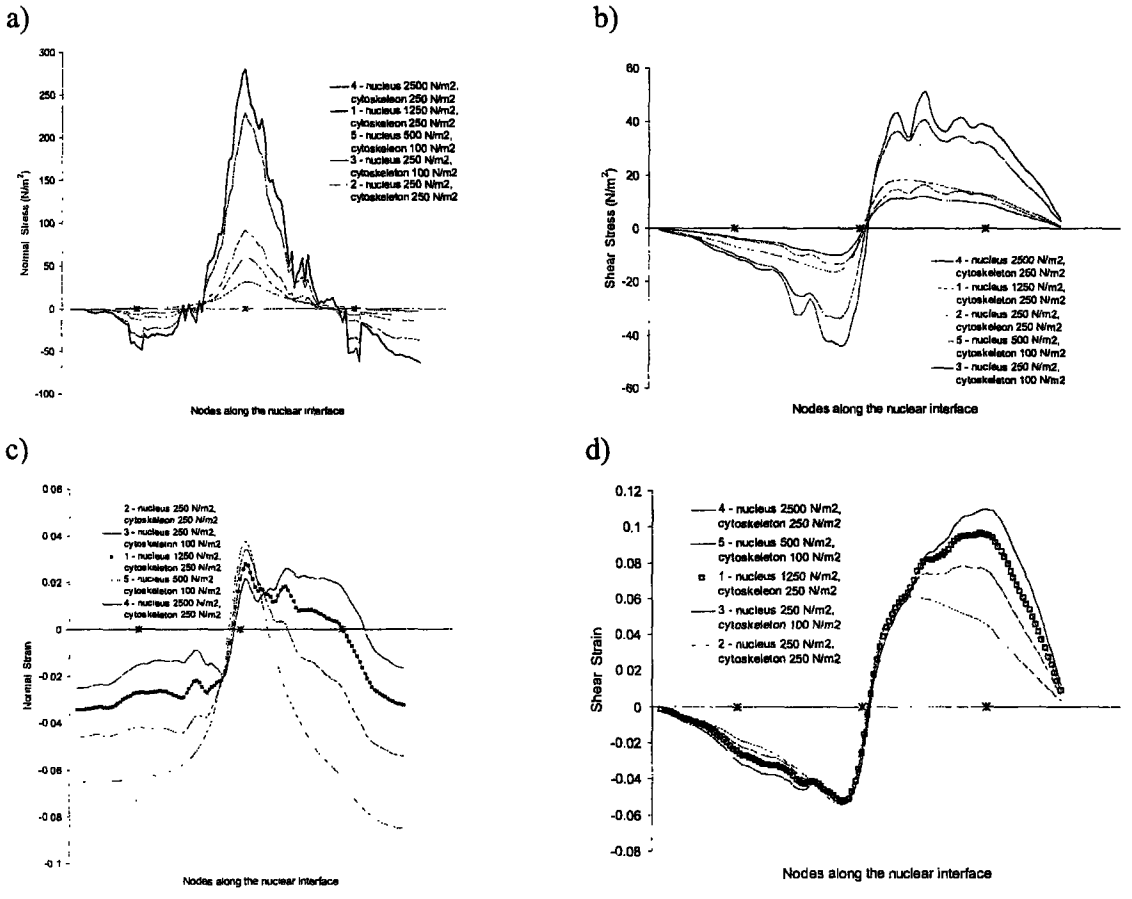

Figure 2.14 Material Properties a) Normal Stress b) Shear Stress c) Normal Strain d) Shear Strain

Experimental Validation

In our previous nuclear strain experiments, we found that *Lmna*$^{-/-}$ fibroblasts had larger nuclear strain under biaxial strain. Condition 3 best describes these cells while Condition 1 or 4 best represented our *Lmna*$^{+/+}$ fibroblasts with normal cytoskeletal material properties and a normal to stiff nucleus. We computed the mean nuclear strain in the Y-direction (parallel to the membrane) based on the total displacement values found at the apex of the nucleus in the elliptical model (Table 2.3), and obtained the minimum and maximum strain values along the mid plane of the nucleus from the ADINA model. The computed mean nuclear strain values lie within the minimum and maximum strain values given from the ADINA and are very close to the average strain values of all the nodes in the nucleus. Normalizing the mean nuclear strain values by the applied membrane strain (5% strain) allowed us to compare the computational results with the experimental normalized nuclear strain data (Figure 1.4) obtained from the nuclear strain experiments (see Table 2.4). The normalized nuclear strain results in *Lmna*$^{+/+}$ (0.2670±0.0444) and *EM*$^{-/y}$ (0.2252±0.0658) fibroblasts was within the normalized mean strain values for Condition 4 (0.1817) , the upper range of normal nuclear stiffness, and Condition 1 (0.3082), suggesting that the nucleus of the fibroblasts is approximately five to ten times stiffer than the cytoskeleton. Experimental behavior of *Lmna*$^{-/-}$ fibroblasts (0.5680± 0.0591 normalized nuclear strain) was best described by condition 3 (0.4789 normalized nuclear strain), consistent with the earlier findings that lamin A/C deficient cells have reduced nuclear and cytoskeletal stiffness.

Condition	Material Properties	Range of Strain in Nucleus from Nodes			Displacement at apex	Mean Strain value from displacement at apex	Normalized Mean Strain value from displacement at apex
		Minimum	Maximum	Node Average			
1	normal nucleus, normal cytoskeleton	0.0123	0.0539	0.0162	0.1387	0.0154	0.3082
2	very soft nucleus, normal cytoskeleton	0.0324	0.0427	0.0363	0.3277	0.0364	0.7283
3	very soft nucleus, soft cytoskeleton	0.0207	0.0482	0.0246	0.2155	0.0239	0.4789
4	stiff nucleus, normal cytoskeleton	0.0047	0.0564	0.0100	0.0818	0.0091	0.1817
5	soft nucleus, soft cytoskeleton	0.0123	0.0539	0.0162	0.1387	0.0154	0.3082

Table 2.3 Average nuclear strain. Normalized strain is defined as the actual nuclear strain divided by the applied membrane strain

Cell type	Mean	Standard Error
Lmna +/+	0.2670	0.0444
Lmna -/-	0.5680	0.0591
EM -/y	0.2252	0.0658

Table 2.4 Experimental Values of normalized nuclear strain from nuclear strain experiment described in the preceding chapters (compare with Figure 1.4)

2.3.3 Adhesion Sites

In our previous models, the applied strain was imposed along the entire cell/silicone membrane interface, assuming tight connections between the cytoskeleton and the membrane over the full length. Cells, however, adhere to the substrate only at specific focal adhesion sites that are predominantly located at the cell periphery (Figure 2.15a). Membrane receptors at these adhesion sites transmit forces from the extracellular environment to the cytoskeleton, which in turn transmits these forces to the nucleus. Staining fixed mouse fibroblasts for focal adhesion proteins paxillin and talin, we found that most focal adhesion sites are located at the outer ~1/3 to 1/10 of the cell radius (Figure 2.15a). Therefore, in order to estimate the effect of localized focal adhesion sites on the intracellular strain distribution, we designed a revised model in which strain was only applied to the outer 10% or 33% length of the cell (see Figure 2.15b). These models are subsequently referred to as the 10%, 33 %, and 100% adhesion model. In this case, the 100% adhesion model represents the elliptical model with the strain applied to the whole length of the cell as used in the previous sections. Normal nuclear and cytoskeletal properties were assumed for all adhesion models and the total strain applied was constant (5% strain) for all three conditions.

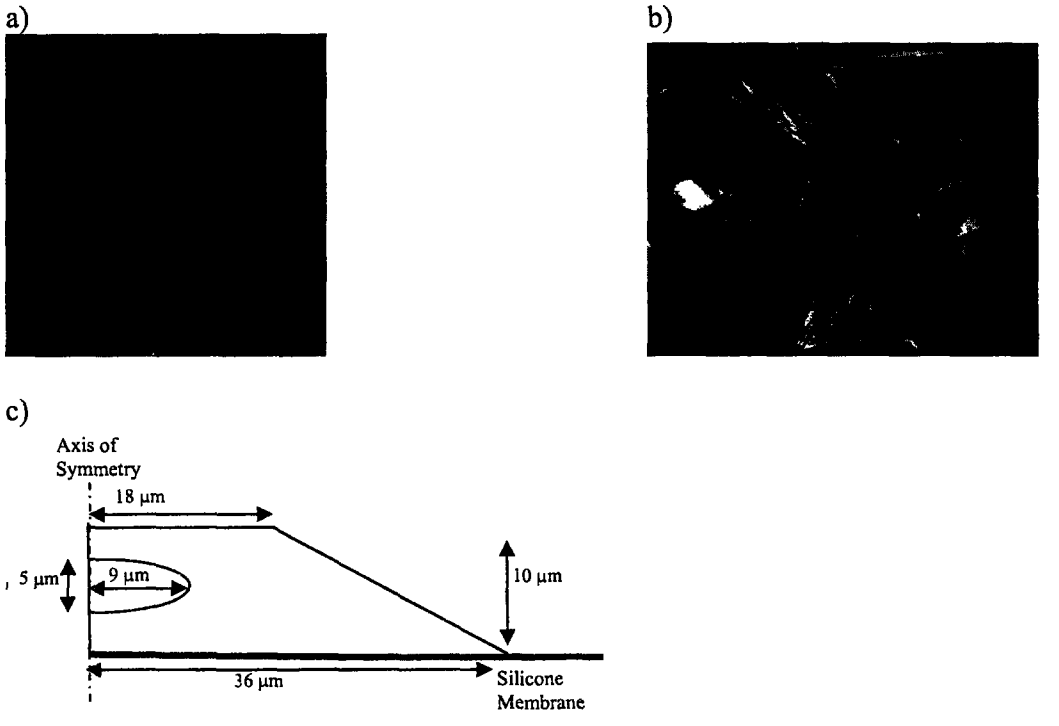

Figure 2.15 a) Fibroblast cell stained with for paxillin, a focal adhesion protein. Focal adhesion sites are seen along the peripheral edge of the cell. b) Actin fibers (green) leading to focal adhesions along the peripheral edge (red). c) Modified adhesion models such that application of strain is at 10% or 33% length of the cell (red line at peripheral edge of cell).

Stress and Strain Distribution

The different adhesion models revealed that cytoskeletal stress distribution strongly depended on adhesion site location and size (Figure 2.16a-c). When adhesion receptors make up 10% or 33% of the bottom edge, the stress was localized in the area of the strain application and stress was transmitted rather uniformly through the rest of the cytoskeleton as well as to the nucleus. Therefore, the 10% adhesion model had the least amount of nuclear stress while the 33% and 100% adhesion model showed increasingly larger nuclear stress. Notably, high cytoskeletal stress and strain concentrations were localized at the point where the adhesion sites end in both the 33% and 10% adhesion model (Figure 2.16b,c, 2.17b,c). No noticeable spikes along the tip region of the nuclear interface were found in the model with 10 and 33% adhesion receptor length as found in the 100% adhesion length model. This is likely due to the decreased and more uniform stress and strain at the nuclear interface.

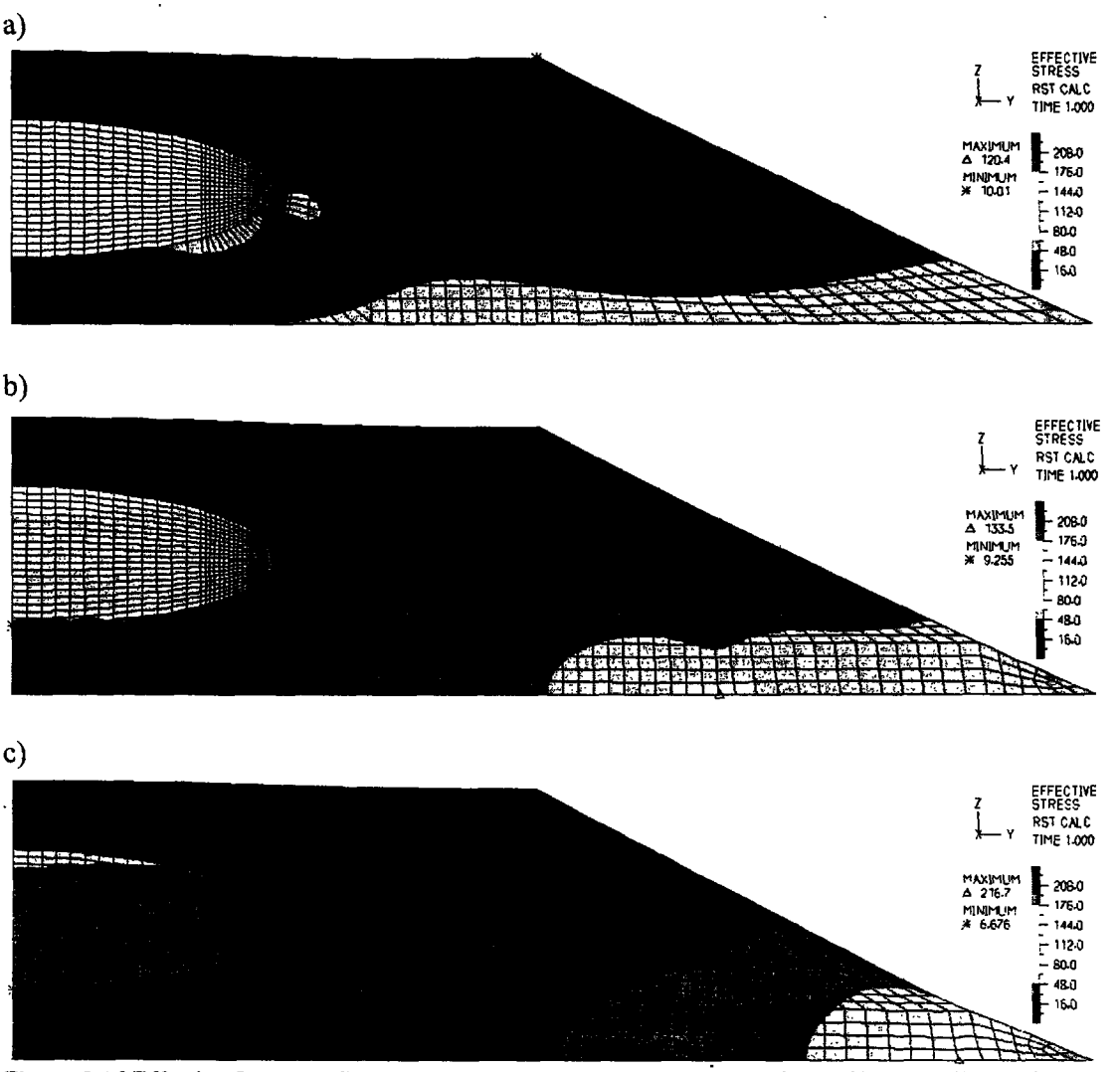

Figure 2.16 Effective Stress profiles of models with a) 100% cell adhesion length b) 33% cell adhesion length c) 10% adhesion length.

a)

b)

c)

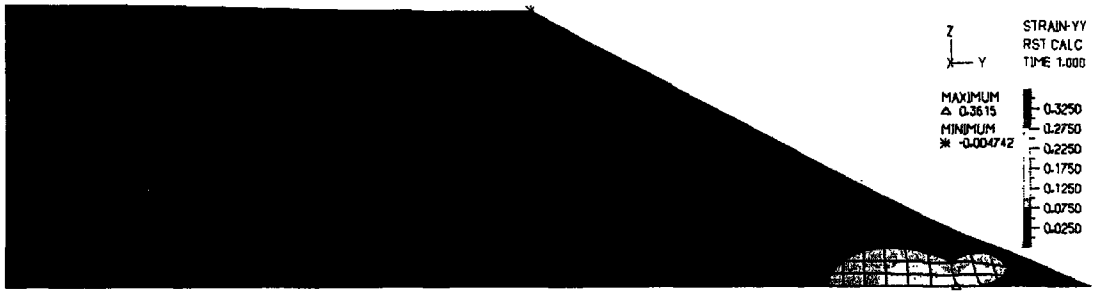

Figure 2.17 Strain-YY profiles of models with a)100% cell adhesion length b) 33% cell adhesion length c) 10% adhesion length.

Normal and Tangential Stress and Strain

Greater magnitudes of normal and tangential stress and strain were found along the interface with an increase in cell length of adhesion receptors (Figures 2.18 a,b).

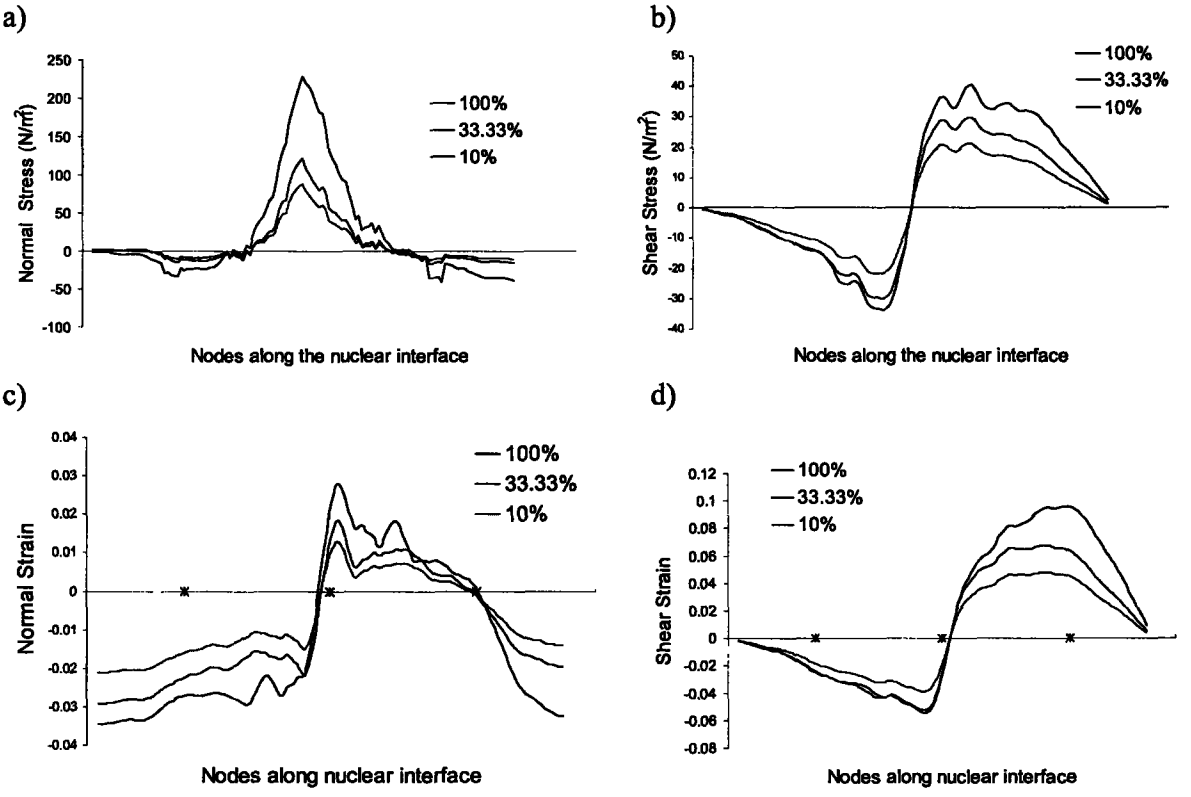

Figure 2.18: Figures of a) normal stress, b) shear stress, c) normal strain, d) shear strain, of the cell adhesion length models.

2.4 DISCUSSION

The finite element models developed in this chapter provide important insights into the role of cytoskeletal shape, nuclear shape, nuclear and cytoskeletal material properties, and focal adhesion size on the intracellular stress and strain distribution in fibroblasts during nuclear strain experiments. By varying each factor separately, its influence on stress and strain levels in the cytoskeleton, nucleus and at the nuclear/cytoskeletal interface could be independently quantified.

Importance of cytoskeletal geometry

Two cytoskeletal geometries were evaluated to compare the stress and strain distribution throughout the cytoskeleton and nucleus. Since stress was transmitted from the membrane through the integrins to the cytoskeleton and subsequently to the nucleus, the geometry selected for the cytoskeleton can be a critical factor in the transmission of stress to the nucleus. In our rectangular model, the maximum stress was localized at the peripheral lower edge, and only low stress levels were transmitted to the top outer corner of the cytoskeleton, that appeared

mechanically isolated from the direct stress transmission path. The strain profile revealed compressive strain at a small region near the bottom lateral edge of the rectangular cytoskeleton. This localized compression may be due to the cytoskeleton resisting the induced strain with a local area of compression that may help to decrease strain to the rest of the cell. The tapered cytoskeletal geometry showed a more uniform and linear distribution of stress throughout the cell. The smallest stresses were found at the top edge where the cytoskeleton began to taper off, but this region was significantly smaller than that found in the rectangular model. Despite the localized regions of extreme stress and strain, the rectangular cytoskeleton only gave a slightly different profile of stress and strain than the cytoskeleton with a linear slant. Consequently, at the cytoskeletal region near the lateral edge, the stress levels near the nucleus were comparable.

Importance of nuclear structure

The shape of the nucleus was the most important structural feature of the model. With a rectangular nucleus, greater stress was found at the corners of the nucleus, thus affecting the stress profile of both the cytoskeleton and the nucleus. As a result, the rectangular nucleus showed a greater magnitude of stress throughout the nucleus than that of the cylindrical and elliptical nucleus, and the sharp corners of the nucleus resulted in localized areas of concentrated stress and strain. In the cylindrical nuclear shape, the stress was localized at the bottom region of the nucleus and decreased linearly such that the upper tip region received less stress. In contrast, the elliptical model had very uniform stress distribution throughout the nucleus, except for some small spikes of high stress near the tip region, which appear to be numerical artifacts that tend to subside as the difference in stiffness between the nucleus and cytoskeleton is reduced (see Figure 2.3c). Overall, stresses in the cylindrical nucleus were larger than in the elliptical nucleus, but the elliptical nucleus had highly localized regions of very high stress. Both the cylindrical and elliptical nucleus showed similar cytoskeletal stress and strain profiles surrounding the nucleus. However, the cylindrical nucleus had larger maximal stress and strain at the nuclear interface than the elliptical nucleus.

Analysis of the normal stresses and strain along the nuclear/cytoskeletal interface revealed important information of the stress and strain transmitted to the nucleus from the cytoskeleton. Since the nucleus has been proposed to act as a mechanosensor in mechanotransduction, these stress or strain levels could play an important role in the mechanosensitive gene regulation. The rectangular nucleus showed sharp transitions of normal and shear stress and strain along the corners of the rectangle. Both the cylindrical and elliptical nucleus showed regions of compressive stress at the top region of the nuclear periphery, increasing tensile stress towards the apex, decreasing tensile stress at the bottom region of the nuclear periphery, and compressive stress on the bottom edge. Surprisingly, the strain profile varied from the stress profile with high compressive strain along the top edge of the nucleus. Also, the cylindrical and elliptical nucleus had high shear stress and strain around the tip region of their nucleus.

These model predictions indicate that nuclear shape/geometry plays an important role on the stress and strain levels within the nucleus, at the interface, and in the cytoskeleton surrounding the nucleus. The nuclear geometry in normal cells can be approximated by both the cylindrical shape and elliptical shape, but the elliptical model is probably a closer representation of the fibroblasts used in our experiments. Our models showed that the elliptical nucleus had the least amount of overall stress and strain throughout the nucleus. However, localized areas of high stress at the cytoskeleton near the interface may possibly explain the nuclear detachment from

the cytoskeleton in our nuclear strain experiments in the case of large biaxial strain application. The *Lmna* and *EM* fibroblasts were seen with an elliptical-shaped nucleus, however, *Lmna*$^{-/-}$ fibroblasts especially showed very irregularly-shaped nuclei that did not fit either the cylindrical or elliptical model. Rather, the nuclei of *Lmna*$^{-/-}$ fibroblasts had a non-continuous shape with abrupt changes in the radius of curvature that could further increase the stress and strain experienced at the nucleus. High stress and strain at the nucleus could then lead to increased nuclear rupture. Therefore, the shape of cells may be important for cells experiencing significant stress or strain.

Importance of Material Properties

Varying the material properties assigned to the nucleus and cytoskeleton revealed that cytoskeletal stiffness and nuclear stiffness as well as the ratio of these two properties determine the magnitude of stress and strain at the nuclear/cytoskeletal interface. The modeling results showed that stress levels (both tensile and compressive) at the interface increased with increasing nuclear stiffness. In addition, increased nuclear stiffness resulted in a more uniform stress distribution throughout the nucleus, but with elevated stress at the nuclear/cytoskeletal interface. The shear stress profile of the nuclear interface revealed that greater cytoskeletal stiffness resulted in higher magnitudes of shear stress. Since the cytoskeleton transmits stress from the membrane to the nucleus, a stiffer cytoskeleton results in less strain and stress, allowing more shear stress to be transmitted to the nucleus. In addition, we found that the ratio between nuclear and cytoskeletal stiffness determined the strain experienced at the nuclear interface. An increased stiffness ratio resulted in reduced levels of normal strain and a greater magnitude of shear strain at the nuclear interface. Since strain was applied in the y-direction, the stress likely decreases in the stiffer material like the nucleus, but transmit even greater stress and strain in the softer material to give a greater overall magnitude of shear strain at the interface. Another factor of the stress and strain distribution of the nucleus is the time dependency of the Maxwell viscoelastic material properties. The strain was applied in a step-wise function with evaluation of stress and strain after one second. However, at steady state, the strain on viscoelastic materials would eventually decrease to zero since the material would not recover to its original shape and size when the strain is removed.

Lammerding et al. [19] reported that *Lmna*$^{-/-}$ fibroblasts had decreased nuclear stiffness as well as reduced cytoskeletal stiffness. The decrease in nuclear stiffness is most likely a consequence of impaired nuclear structure due to the loss of lamin A/C in the nuclear lamina. The surprising concomitant decrease in cytoskeletal stiffness was hypothesized to be a cellular adaptation to the softer and more fragile nucleus. The cellular response of decreased cytoskeletal stiffness could thus be a compensatory mechanism to protect the nucleus from excessive stress and strain, possibly mediated by nuclear mechanotransduction mechanisms. Our finite element data suggests that a decrease in nuclear stiffness without changes in cytoskeletal stiffness (Condition 2) would result in a decrease in the nuclear to cytoskeletal stiffness ratio and lead to significantly higher nuclear stress and strain levels compared to normal cells. The results summarized in Table 2.3 clearly demonstrate that a compensatory reduction in cytoskeletal stiffness reduces the mean nuclear strain by ~ 24.9%. In addition, the normal strain component at the nuclear/cytoskeletal interface is dramatically reduced compared to the uncompensated case (see Figure 2.14c). Thus, it is conceivable that nuclear strain levels are an important factor in cellular mechanotransduction. In consequence, a softer cytoskeleton would prevent an increase in shear stress and strain along the nuclear interface.

Importance of Adhesion Sites

Evaluation of the effect of localized cellular adhesion sites on intracellular stress and strain distribution demonstrates a strong dependence between cytoskeletal stress and strain levels on the size and location of the focal adhesion sites. In the nuclear strain experiments, the applied strain is transmitted from the membrane to the cytoskeleton through adhesion receptors. Our computational results revealed that increased adhesion size, i.e. the area where the cytoskeleton and membrane are physically connected, results in increased normal and tangential stress and strain at nucleus, even though the applied membrane strain was held constant. In the case of localized adhesion sites (the 10% and 33% models), localized areas of high stress and strain were found at the inner edge of the focal adhesion sites. However, since the stress and strain was more localized and farther away from the nucleus, lower stress and strain levels were seen at the nuclear interface. This finding might explain one of the many practical reasons why adhesion receptors are found along the peripheral edge of the cell and at the cell center or below the nucleus.

2.5 CONCLUSION and OUTLOOK

From our analysis of the various models, it was found that nuclear shape, material properties of the cytoskeleton and nucleus, as well as the length of strain application on the peripheral edge are important parameters in determining the magnitude of stress and strain at the nuclear interface. The nuclear shape determined whether the stress and strain were distributed throughout the cell or at the nucleus-cytoskeleton interface. High nuclear stiffness resulted in greater tension and compression along the nuclear interface while greater cytoskeletal stiffness yielded higher magnitudes of shear stress at the interface. Also, greater ratios of nuclear stiffness to cytoskeletal stiffness, resulted in larger magnitudes of shear strain and smaller magnitudes of normal strain on the nucleus. These correlations hope to further reveal the interaction between the nucleus and cytoskeleton of cells. If these correlations are verified experimentally, the cellular response to cytoskeletal compensation of decreased cytoskeletal stiffness is an important mechanism to protect the nucleus from greater stress and strain.

Although the cytoskeletal shape did not seem to impact the relationship between nucleus and cytoskeleton, it might be useful to model other cytoskeletal shapes that are seen in cells. A smooth, rounded cytoskeletal shape may be one possible geometry that could be explored. It would be interesting to explore the effect of material properties and cell adhesion lengths on a cell with a cylindrical-shaped nucleus. Also, the time dependency of the intracellular stress and strain profiles after the step-wise strain application would be important to explore as well. Cyclic strain application would be another possible useful modification to consider. Our models did not include a nuclear membrane, which has been shown to have even stiffer material properties than the nucleus. Addition of a nuclear membrane would likely affect the magnitude and profiles of stress and strain in the nucleus as well as in the cytoskeleton. Further modifications of the cell adhesion length would also be useful since strain would not be applied continuously along the cell bottom, but at very small adhesion sites along the peripheral edge of the cell. In our previous nuclear strain experiments, nuclear strain increased quite linearly with applied membrane strain. Therefore, another useful modification in our models would be to increase the applied strain to 10% and 20% strain on the elliptical model to see if strain increased linearly in our models as

well. Nuclear strain experiments can be conducted using $Lmna^{+/+}$ fibroblasts treated with cytochalasin, an actin filament disrupting drug that makes the cytoskeleton softer. This would give experimental strain values of a normally stiff nucleus with a soft cytoskeleton and can be compared to a model with normal nuclear properties and soft cytoskeletal properties. A continuum approximation was assumed for the cell, which is valid so long as the scale of our interest in much larger than the cytoskeletal and nuclear stress fibers. Our models represent a very simplified representation of the cells modeled; however, with further modifications to the model, the interactions between the cytoskeleton and nucleus can be more accurately explored.

3.0 REFRENCES

1. Cohen, M., Lee, K. K., Wilson, K. L. & Gruenbaum, Y. Transcriptional repression, apoptosis, human disease and the functional evolution of the nuclear lamina. *Trends Biochem Sci* **26**, 41-7 (2001).
2. Wilson, K. L., Zastrow, M. S. & Lee, K. K. Lamins and disease: insights into nuclear infrastructure. *Cell* **104**, 647-50 (2001).
3. Fairley, E. A., Riddell, A., Ellis, J. A. & Kendrick-Jones, J. The cell cycle dependent mislocalisation of emerin may contribute to the Emery-Dreifuss muscular dystrophy phenotype. *J Cell Sci* **115**, 341-54 (2002).
4. Maraldi, N. M., Lattanzi, G., Sabatelli, P., Ognibene, A. & Squarzoni, S. Functional domains of the nucleus: implications for Emery-Dreifuss muscular dystrophy. *Neuromuscul Disord* **12**, 815-23 (2002).
5. Bengtsson, L. & Wilson, K. L. Multiple and surprising new functions for emerin, a nuclear membrane protein. *Curr Opin Cell Biol* **16**, 73-9 (2004).
6. Wilkinson, F. L. et al. Emerin interacts in vitro with the splicing-associated factor, YT521-B. *Eur J Biochem* **270**, 2459-66 (2003).
7. Burke, B. & Stewart, C. L. Life at the edge: the nuclear envelope and human disease. *Nat Rev Mol Cell Biol* **3**, 575-85 (2002).
8. Bechert, K., Lagos-Quintana, M., Harborth, J., Weber, K. & Osborn, M. Effects of expressing lamin A mutant protein causing Emery-Dreifuss muscular dystrophy and familial partial lipodystrophy in Hela cells. *Exp Cell Res* **286**, 75-86 (2003).
9. Burke, B., Mounkes, L. C. & Stewart, C. L. The nuclear envelope in muscular dystrophy and cardiovascular diseases. *Traffic* **2**, 675-83 (2001).
10. De Sandre-Giovannoli, A. et al. Homozygous defects in LMNA, encoding lamin A/C nuclear-envelope proteins, cause autosomal recessive axonal neuropathy in human (Charcot-Marie-Tooth disorder type 2) and mouse. *Am J Hum Genet* **70**, 726-36 (2002).
11. Ostlund, C., Bonne, G., Schwartz, K. & Worman, H. J. Properties of lamin A mutants found in Emery-Dreifuss muscular dystrophy, cardiomyopathy and Dunnigan-type partial lipodystrophy. *J Cell Sci* **114**, 4435-45 (2001).
12. Mounkes, L., Kozlov, S., Burke, B. & Stewart, C. L. The laminopathies: nuclear structure meets disease. *Curr Opin Genet Dev* **13**, 223-30 (2003).
13. De Sandre-Giovannoli, A. et al. Lamin A Truncation in Hutchinson-Gilford Progeria. *Science* (2003).
14. Mounkes, L. C., Kozlov, S., Hernandez, L., Sullivan, T. & Stewart, C. L. A progeroid syndrome in mice is caused by defects in A-type lamins. *Nature* **423**, 298-301 (2003).
15. De Keulenaer, G. W. et al. Identification of IEX-1 as a biomechanically controlled nuclear factor-kappaB target gene that inhibits cardiomyocyte hypertrophy. *Circ Res* **90**, 690-6 (2002).
16. Granet, C., Boutahar, N., Vico, L., Alexandre, C. & Lafage-Proust, M. H. MAPK and SRC-kinases control EGR-1 and NF-kappa B inductions by changes in mechanical environment in osteoblasts. *Biochem Biophys Res Commun* **284**, 622-31 (2001).
17. Sullivan, T. et al. Loss of A-type lamin expression compromises nuclear envelope integrity leading to muscular dystrophy. *J Cell Biol* **147**, 913-20 (1999).

18. Wehnert, M. & Muntoni, F. 60th ENMC International Workshop: non X-linked Emery-Dreifuss Muscular Dystrophy 5-7 June 1998, Naarden, The Netherlands. *Neuromuscul Disord* **9**, 115-21 (1999).
19. Lammerding, J. et al. Lamin A/C deficiency causes defective nuclear mechanics and mechanotransduction. *J Clin Invest* **113**, 370-8 (2004).
20. Markiewicz, E. et al. Increased solubility of lamins and redistribution of lamin C in X-linked Emery-Dreifuss muscular dystrophy fibroblasts. *J Struct Biol* **140**, 241-53 (2002).
21. Vigouroux, C. et al. Nuclear envelope disorganization in fibroblasts from lipodystrophic patients with heterozygous R482Q/W mutations in the lamin A/C gene. *J Cell Sci* **114**, 4459-68 (2001).
22. Kumar, A. & Boriek, A. M. Mechanical stress activates the nuclear factor-kappaB pathway in skeletal muscle fibers: a possible role in Duchenne muscular dystrophy. *Faseb J* **17**, 386-96 (2003).
23. Germain, F., Doisy, A., Ronot, X. & Tracqui, P. Characterization of cell deformation and migration using a parametric estimation of image motion. *IEEE Trans Biomed Eng* **46**, 584-600 (1999).
24. Thomas, C. H., Collier, J. H., Sfeir, C. S. & Healy, K. E. Engineering gene expression and protein synthesis by modulation of nuclear shape. *Proc Natl Acad Sci U S A* **99**, 1972-7 (2002).
25. Bissell, M. J. et al. Tissue structure, nuclear organization, and gene expression in normal and malignant breast. *Cancer Res* **59**, 1757-1763s; discussion 1763s-1764s (1999).
26. Maniotis, A. J., Chen, C. S. & Ingber, D. E. Demonstration of mechanical connections between integrins, cytoskeletal filaments, and nucleoplasm that stabilize nuclear structure. *Proc Natl Acad Sci U S A* **94**, 849-54 (1997).
27. Papadaki, M. & Eskin, S. G. Effects of fluid shear stress on gene regulation of vascular cells. *Biotechnol Prog* **13**, 209-21 (1997).
28. Burger, E. H. & Klein-Nulend, J. Mechanotransduction in bone--role of the lacuno-canalicular network. *Faseb J* **13 Suppl**, S101-12 (1999).
29. Kan, H. C., Shyy, W., Udaykumar, H. S., Vigneron, P. & Tran-Son-Tay, R. Effects of nucleus on leukocyte recovery. *Ann Biomed Eng* **27**, 648-55 (1999).
30. Guilak, F. The deformation behavior and viscoelastic properties of chondrocytes in articular cartilage. *Biorheology* **37**, 27-44 (2000).
31. Guilak, F., Tedrow, J. R. & Burgkart, R. Viscoelastic properties of the cell nucleus. *Biochem Biophys Res Commun* **269**, 781-6 (2000).
32. Lammerding, J. in *Bioengineering* 283 (Massachusetts Institute of Technology, Cambridge, 2004).

Appendix A: Experimental Setups

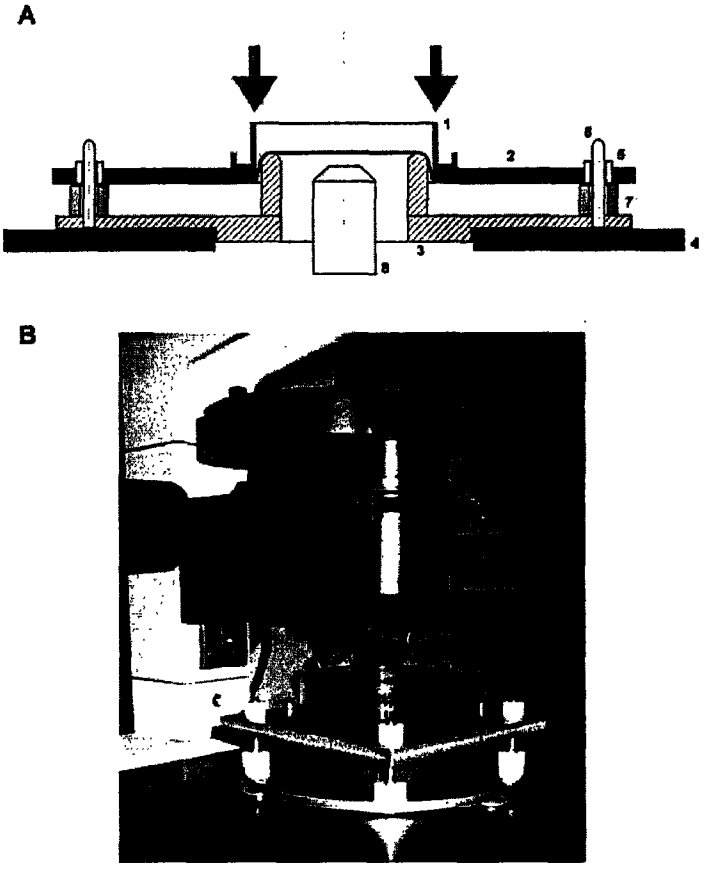

Figure A.1. Nuclear Strain Device Design.
A) Schematic of the strain device in cross-section. The silicone membrane cell culture dish (*1*) is mounted onto the dish-holder plate (*2*) and placed on the base plate (*3*) that fits firmly onto the microscope stage (*4*). Polytetrafluoroethylene bearings (*5*) in the dish-holder plate and vertical pins (*6*) on the base plate provide precise alignment and stabilization of the silicone membrane dish relative to the stationary platen. Nylon spacers (*7*) limit the vertical displacement and thus the applied membrane strain. A central bore in the base plate accommodates the high power microscope objective (*8*).
B) Strain device with a cell culture dish in resting condition mounted on an inverted Olympus IX-70 microscope.

* figures and details provided by Jan Lammerding [32]

Figure A.2. Magnetic trap set-up. The magnetic trap is mounted on a manually operated micromanipulator at an angle of ~45°. At this angle, the lower edge of the magnetic trap tip is approximately parallel to the microscope stage. The magnetic coil is powered by a computer controlled power supply not visible in this image. The sample dish on the temperature controlled microscope stage can be seen in the image center.

* figure and details provided by Jan Lammerding [32]

Appendix B: Oligonucleotide Sequences

Integrated DNA Technologies, Inc.
25 nmole DNA Oligonucleotide Standard desalting, 20 bases

mouse β tubulin sense	5' – GGA ACA TAG CCG TAA ACT GC -3'
mouse β tubulin antisense	5' – TCA CTG TGC CTG AAC TTA CC – 3'
mouse egr-1 sense	5' – GTC ACT GGC CTC GTG AGC AT – 3'
mouse egr-1 antisense	5' – AGG TGG TCA CTA CGA CTG AA- 3'
mouse gapdh sense	5' – ACC ACA GTC CAT GCC ATC AC -3'
mouse gapdah antisense	5' – TCC ACC ACC CTG TTG CTG TA – 3'
mouse iex-1 sense 406	5' – CCA TCT CCA CAC CAT GAC TG – 3'
mouse iex-1 antisense 406	5' – CTC CGA GGT CAG GTT CAA AC – 3'
mouse iex-1 sense 194	5' – TCT GGT CCC GAG ATT TTC AC – 3'
mouse iex-1 antisense 194	5' – AAG ATG ATG GCG AAC AGG AG – 3'

Appendix C: Geometry of Rectangular Model

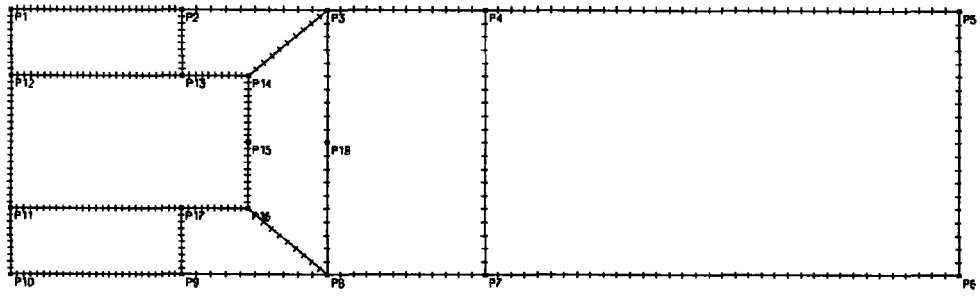

Figure C1: Points of Rectangular Model

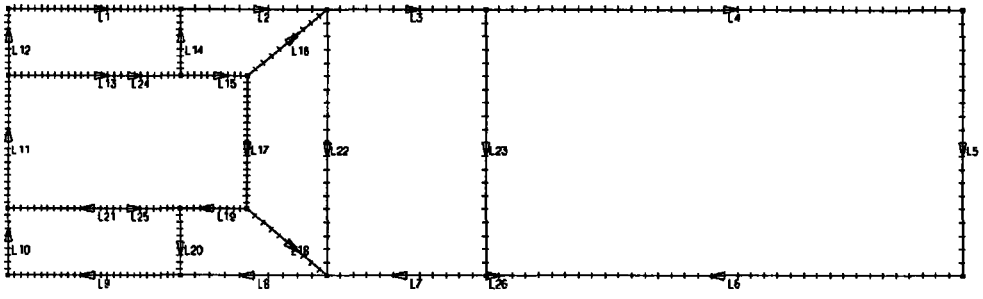

Figure C2: Lines of Rectangular Model

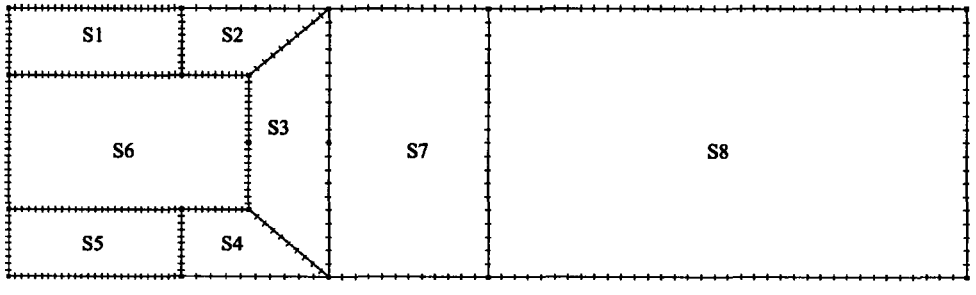

Figure C3: Surface areas of Rectangular Model

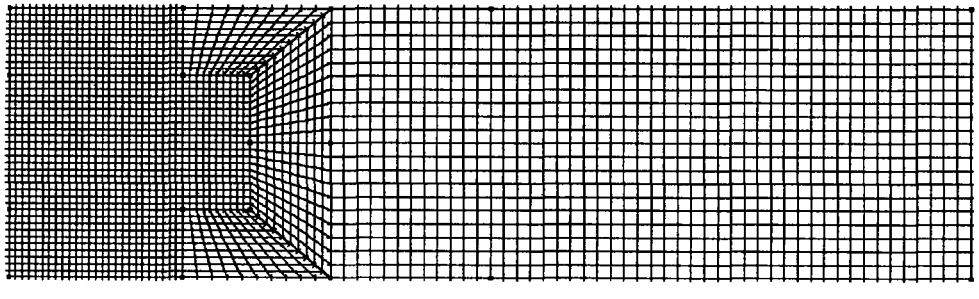

Figure C4: Mesh Lines of Rectangular Model

Point #	x1	x2	x3	System
1	0	0	0	0
2	0	6.5	0	0
3	0	12	0	0
4	0	18	0	0
5	0	36	0	0
6	0	36	-10	0
7	0	18	-10	0
8	0	12	-10	0
9	0	6.5	-10	0
10	0	0	-7.5	0
11	0	0	-7.5	0
12	0	0	-2.5	0
13	0	6.5	-2.5	0
14	0	9	-2.5	0
15	0	9	-5	0
16	0	9	-7.5	0
17	0	6.5	-7.5	0
18	0	12	-5	0

Table C1: Coordinates of Points of Rectangular Model

Line	Point 1	Point 2	Type
1	1	2	Straight
2	2	3	Straight
3	3	4	Straight
4	4	5	Straight
5	5	6	Straight
6	6	7	Straight
7	7	8	Straight
8	8	9	Straight
9	9	10	Straight
10	10	11	Straight
11	11	12	Straight
12	12	1	Straight
13	12	13	Straight
14	2	13	Straight
15	13	14	Straight
16	14	3	Straight
17	14	16	Straight
18	16	8	Straight
19	16	17	Straight
20	17	9	Straight
21	17	11	Straight
22	3	18	Straight
23	4	7	Straight
24	13	15	Combined
25	21	19	Combined

Table C2: Coordinate of Lines of Rectangular Model

Surface	Line 1	Line 2	Line 3	Line 4	Type
1	1	14	13	12	Patch
2	2	16	15	14	Patch
3	16	17	18	22	Patch
4	19	18	8	20	Patch
5	21	20	9	10	Patch
6	11	24	17	25	Patch
7	3	22	7	23	Patch
8	23	4	5	6	Patch

Table C3: Coordinate of Surfaces of Rectangular Model

Appendix D: Geometry of Cylindrical Model

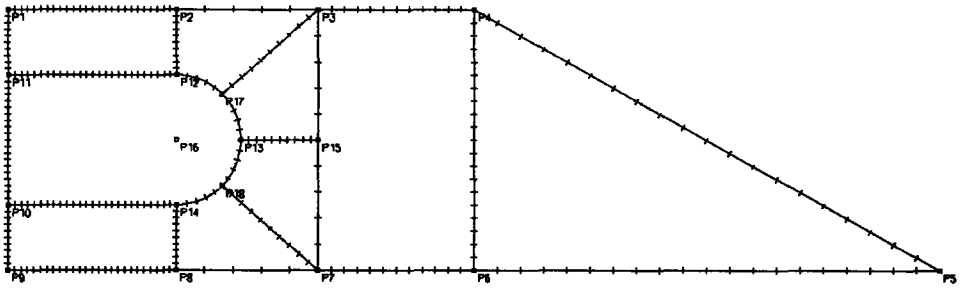

Figure D1: Points of Cylindrical Model

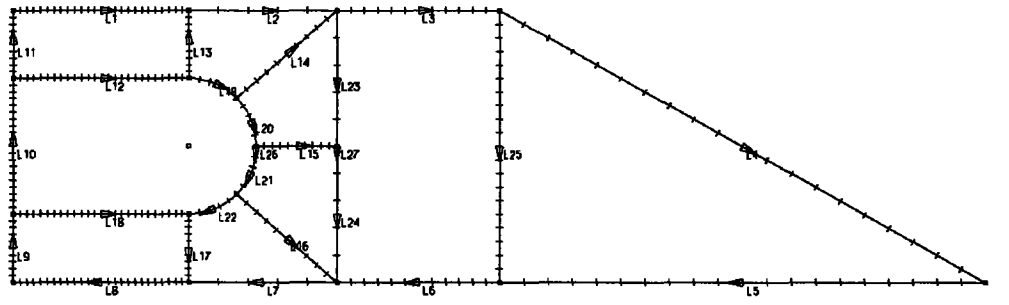

Figure D2: Lines of Cylindrical Model

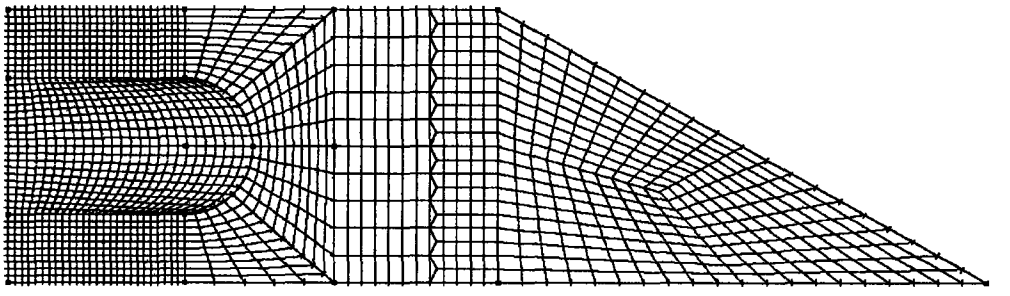

Figure D3: Mesh Plot of Cylindrical Model

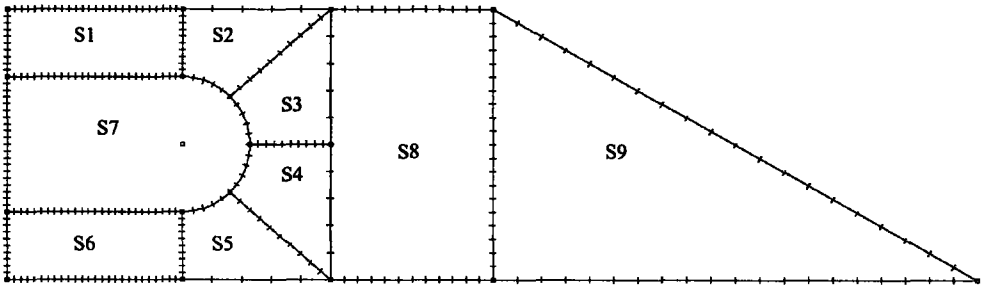

Figure D4: Surface Areas of Cylindrical Model

Point #	x1	x2	x3	System
1	0	0	0	0
2	0	6.5	0	0
3	0	12	0	0
4	0	18	0	0
5	0	36	-10	0
6	0	18	-10	0
7	0	12	-10	1
8	0	6.5	-10	0
9	0	0	-10	0
10	0	0	-7.5	0
11	0	0	-2.5	0
12	0	6.5	-2.5	0
13	0	9	-5	0
14	0	6.5	-7.5	0
15	0	12	-5	0
16	0	0	0	1

Table D1: Coordinate of Points of Cylindrical Model

System Number	1		
Type	Cylindrical		
Defined by	Origin and Direction Vectors		
Origin	x = 0	y = 6.5	z = -5
Vector A	x = 1	y = 0	z = 0
Vector B	x = 0	y = 1	z = 0

Table D2: System 1 Coordinates of Cylindrical Model

Line	Point 1	Point 2	Point 3	Point 4	Center	Type
1	1	2				Straight
2	2	3				Straight
3	3	4				Straight
4	4	5				Straight
5	5	6				Straight
6	6	7				Straight
7	7	8				Straight
8	8	9				Straight
9	9	10				Straight
10	10	11				Straight
11	11	1				Straight
12	11	12				Straight
13	2	12				Straight
14	17	3				Straight
15	13	15				Straight
16	18	7				Straight
17	14	8				Straight
18	10	14				Straight
19	12	17			16	Arc
20	17	13			16	Arc
21	13	18			16	Arc
22	18	14			16	Arc
23	3	15				Straight
24	15	7				Straight
25	4	6				
26	19	20	21	22		Combined
27	23	24				Combined

Table D2: Coordinate of Lines of Cylindrical Model

Surface	Line 1	Line 2	Line 3	Line 4	Type
1	1	13	12	11	Patch
2	2	13	10	14	Patch
3	23	14	20	15	Patch
4	15	24	16	21	Patch
5	22	16	7	17	Patch
6	18	17	8	9	Patch
7	10	12	26	18	Patch
8	3	27	6	25	Patch
9	25	4	5		Patch

Table D3:Coordinate of Surfaces of Cylindrical Model

Appendix E: Geometry of Ellipitcal Model

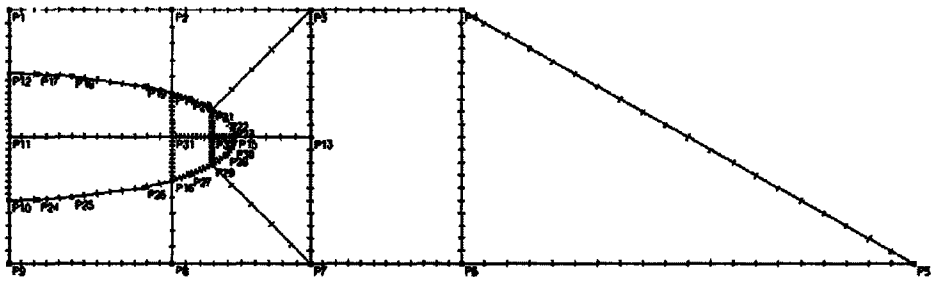

Figure E1: Points in Elliptical Model

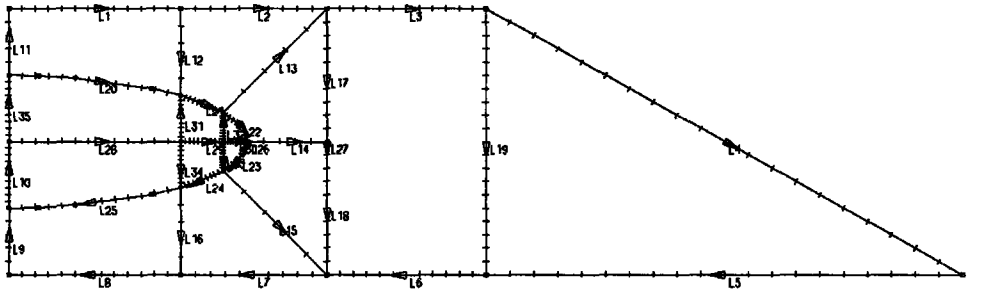

Figure E2: Lines in Elliptical Model

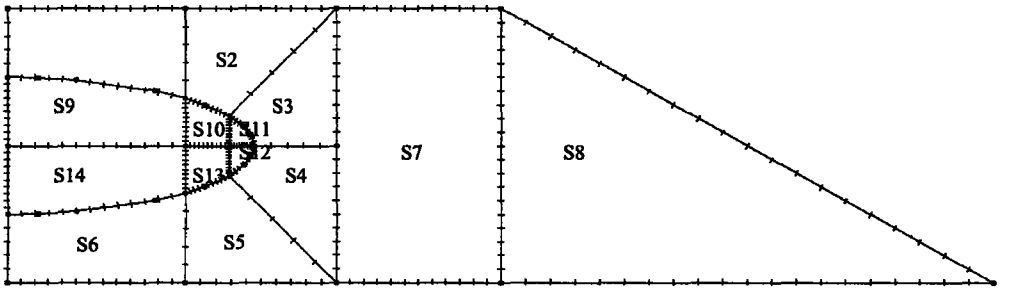

Figure E3: Surfaces of Elliptical Model

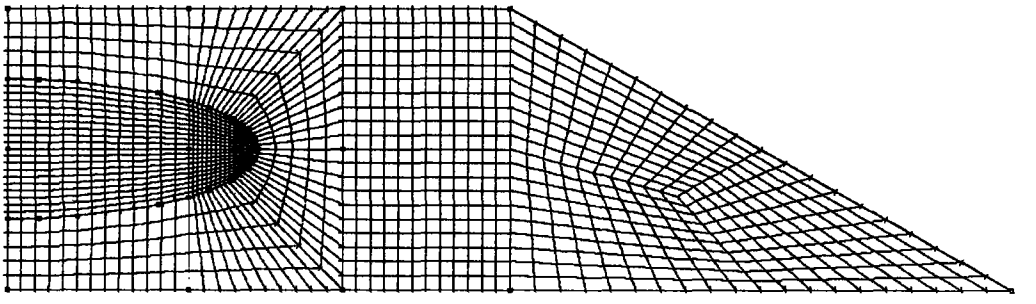

Figure E4: Mesh Plot of Elliptical Model

Point #	x1	x2	x3	System
1	0	0	0	0
2	0	6.5	0	0
3	0	12	0	0
4	0	18	0	0
5	0	36	-10	0
6	0	18	-10	0
7	0	12	-10	0
8	0	6.5	-10	0
9	0	0	-10	0
10	0	0	-7.5	0
11	0	0	-5	0
12	0	0	-2.5	0
13	0	12	-5	0
14	0	6.5	-3.27085	0
15	0	9	-5	0
16	0	6.5	-6.72915	0
17	0	1.13614	-2.52	0
18	0	2.52	-2.6	0
19	0	5.4	-3	0
20	0	7.2	-3.5	0
21	0	8.08198	-3.9	0
22	0	8.64	-4.3	0
23	0	8.880405	-4.6	0
24	0	1.13614	-7.48	0
25	0	2.52	-7.4	0
26	0	5.4	-7	0
27	0	7.2	-6.5	0
28	0	8.64	-5.7	0
29	0	8.08198	-6.1	0
30	0	8.880406	-5.4	0

Table E1: Coordinate of Points of Elliptical Model

Line	Point 1	Point 2	Point 3	Point 4	Center	Type
1	1	2				Straight
2	2	3				Straight
3	3	4				Straight
4	4	5				Straight
5	5	6				Straight
6	6	7				Straight
7	7	8				Straight
8	8	9				Straight
9	9	10				Straight
10	10	11				Straight
11	12	1				Straight
12	2	14				Straight
13	21	3				Straight
14	15	13				Straight
15	29	7				Straight
16	16	8				Straight
17	3	13				Straight
18	13	7				Straight
19	4	6				Straight
20	12	17	18	19	14	Polyline
21	14	20	21			Polyline
22	21	22	23	15		Polyline
23	15	30	28	29		Polyline
24	29	27	16			Polyline
25	10	24	25	26	16	Polyline
26	21	22	23	24		Combined
27	17	18				Combined
28	11	31				Straight
29	31	32				Straight
30	32	15				Straight
31	31	14				Straight
32	32	21				Straight
33	32	29				Straight
34	31	16				Straight
35	11	12				Straight

Table E2: Coordinate of Lines of Ellipitcal Model
Note: Type Polyline with straight segments

Surface	Line 1	Line 2	Line 3	Line 4	Type
1	1	12	20	11	Patch
2	2	13	21	12	Patch
3	13	17	14	22	Patch
4	18	15	23	14	Patch
5	24	15	7	16	Patch
6	25	16	8	9	Patch
7	27	3	19	6	Patch
8	19	4	5		Patch
9	35	20	21	28	Patch
10	21	32	29	31	Patch
11	32	22	30		Patch
12	30	23	33		Patch
13	29	33	24	34	Patch
14	28	34	25	10	Patch

Table E3: Coordinate of Surfaces of Elliptical Model

Appendix F: Plot Command Files

Plot Command File for Cylindrical Model

```
CONSTANT YA 9.0
CONSTANT Y0 6.5
CONSTANT ZA 2.5
CONSTANT Z0 -5.0
CONSTANT RADIUS_CYLINDER 2.5
ALIAS Y 'Y-COORDINATE'
ALIAS Z 'Z-COORDINATE'
ALIAS TYY 'STRESS-YY'
ALIAS TZZ 'STRESS-ZZ'
ALIAS TYZ 'STRESS-YZ'
RESULTANT RADIUS_POINT 'MAX(SQRT((Y-
        Y0)**2 + (Z-Z0)**2),1E-5)'
RESULTANT COSN 'STEP(Y-Y0)*(Y-
        Y0)/RADIUS_POINT'
RESULTANT SINN '(STEP(Y-Y0)*(Z-
        Z0)/RADIUS_POINT) + (1.0 - STEP(Y-
        Y0))*(-1.0 + 2.0*STEP(Z-Z0))'
RESULTANT ANGLEN 'ATAN2(SINN,COSN)'
RESULTANT COS2N 'COS(2.0*ANGLEN)'
RESULTANT SIN2N 'SIN(2.0*ANGLEN)'
RESULTANT TNN '0.5*(TYY + TZZ) + 0.5*(TYY
        - TZZ)*COS2N + TYZ*SIN2N'
RESULTANT TNT '-0.5*(TYY - TZZ)*SIN2N +
        TYZ*COS2N'
ZONE NUCLEUS 'ELEMENT GROUP 2'
ZONE CYTOSKELETON 'ELEMENT GROUP 1'
DATAEND
```

Plot Command File for Elliptical Model

```
CONSTANT YA 9.0
CONSTANT ZA 2.5
CONSTANT Z0 -5.0
ALIAS Y 'Y-COORDINATE'
ALIAS Z 'Z-COORDINATE'
ALIAS TYY 'STRESS-YY'
ALIAS TZZ 'STRESS-ZZ'
ALIAS TYZ 'STRESS-YZ'
RESULTANT COSA 'Y/YA'
RESULTANT SINA '(Z-Z0)/ZA'
RESULTANT COSN 'ZA*COSA'
RESULTANT SINN 'YA*SINA'
RESULTANT ANGLEN 'ATAN2(SINN,COSN)'
RESULTANT COS2N 'COS(2.0*ANGLEN)'
RESULTANT SIN2N 'SIN(2.0*ANGLEN)'
RESULTANT TNN '0.5*(TYY + TZZ) + 0.5*(TYY
        - TZZ)*COS2N + TYZ*SIN2N'
RESULTANT TNT '-0.5*(TYY - TZZ)*SIN2N +
        TYZ*COS2N'
ZONE NUCLEUS
'ELEMENT GROUP 2'
ZONE CYTOSKELETON
'ELEMENT GROUP 1'
DATAEND
```

Trig representation of an ellipse:

$y=y_a*\cos(\alpha)$ (α is a parametric variable)
$z=z_a*\sin(\alpha) + z_o$

$n_y=z_a*\cos(\alpha)/denom$
$n_z=y_a*\sin(\alpha)/denom$
$denom=sqrt((y_a*\cos(\alpha))**2 + (z_a*\sin(\alpha))**2)$

$\theta = \tan(n_z/ny)$ where θ is the angle between the y axis and the normal)

Mohr's circle used to compute stress/strain.

written by Ted Sussman from ADINA R&D, Inc.

Appendix G: Results in More detail

a)

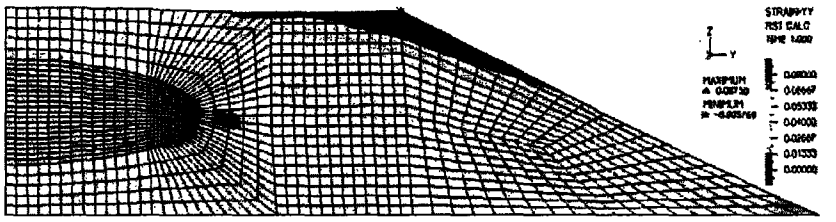

b)

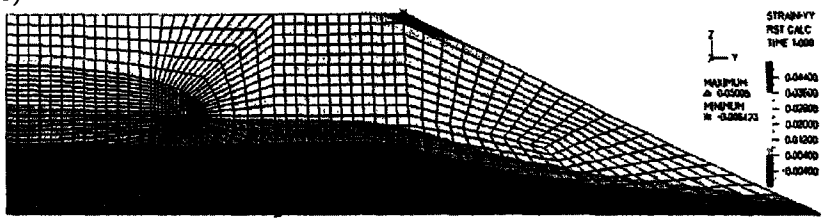

c)

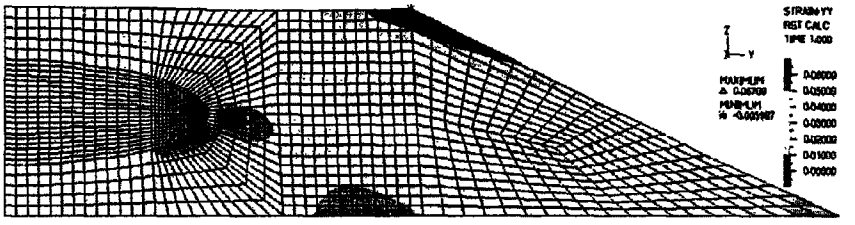

d)

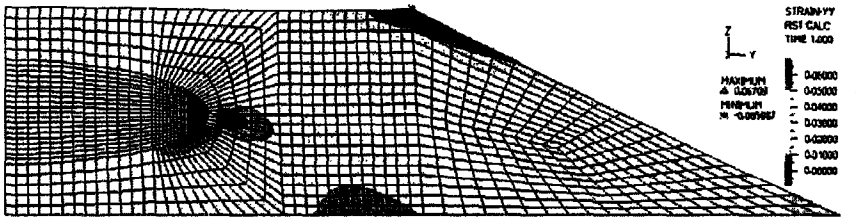

e)

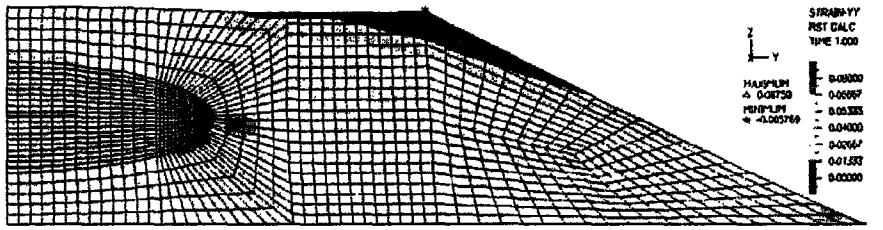

Figure G.1 Strain YY of elliptical model with various material properties and scaled individually for more detailed strain profile of a) condition 1 - normal nucleus 1250 N/m^2, normal cytoskeleton 250 N/m^2 b) condition 2 – very soft nucleus 250 N/m^2, normal cytoskeleton 250 N/m^2 c) condition 3 – very soft nucleus 250 N/m^2, soft cytoskeleton 100 N/m^2, d) condition 4 – hard nucleus 2500 N/m^2, normal cytoskeleton 250 N/m^2, e) condition 5 – soft nucleus 500 N/m^2, soft cytoskeleton 100 N/m^2.

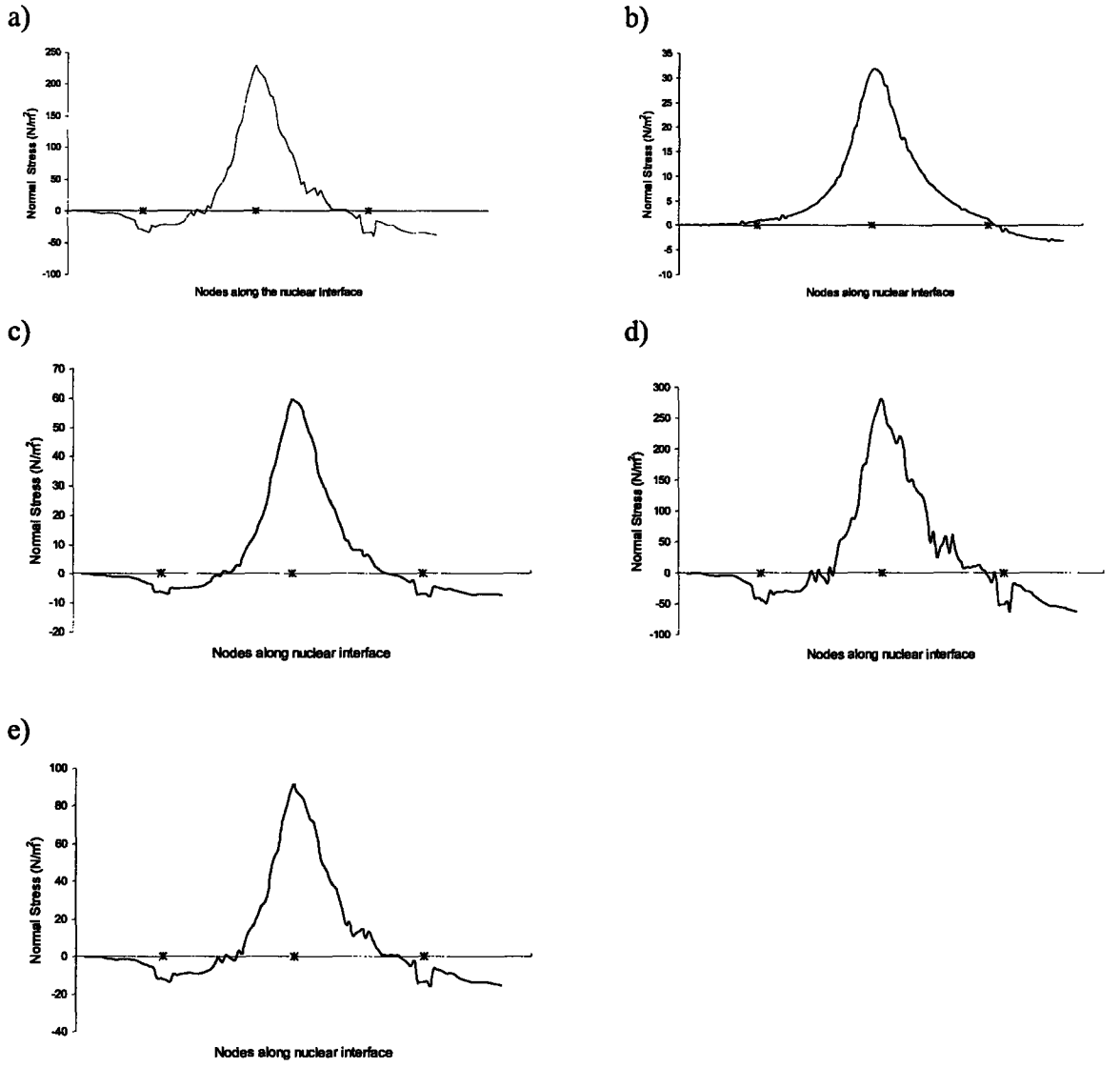

Figure G.2 Normal Stresses along nuclear interface for elliptical with various material properties. a) condition 1 - normal nucleus 1250 N/m^2, normal cytoskeleton 250 N/m^2 b) condition 2 – very soft nucleus 250 N/m^2, normal cytoskeleton 250 N/m^2 c) condition 3 – very soft nucleus 250 N/m^2, soft cytoskeleton 100 N/m^2, d) condition 4 – hard nucleus 2500 N/m^2, normal cytoskeleton 250 N/m^2, e) condition 5 – soft nucleus 500 N/m^2, soft cytoskeleton 100 N/m^2.

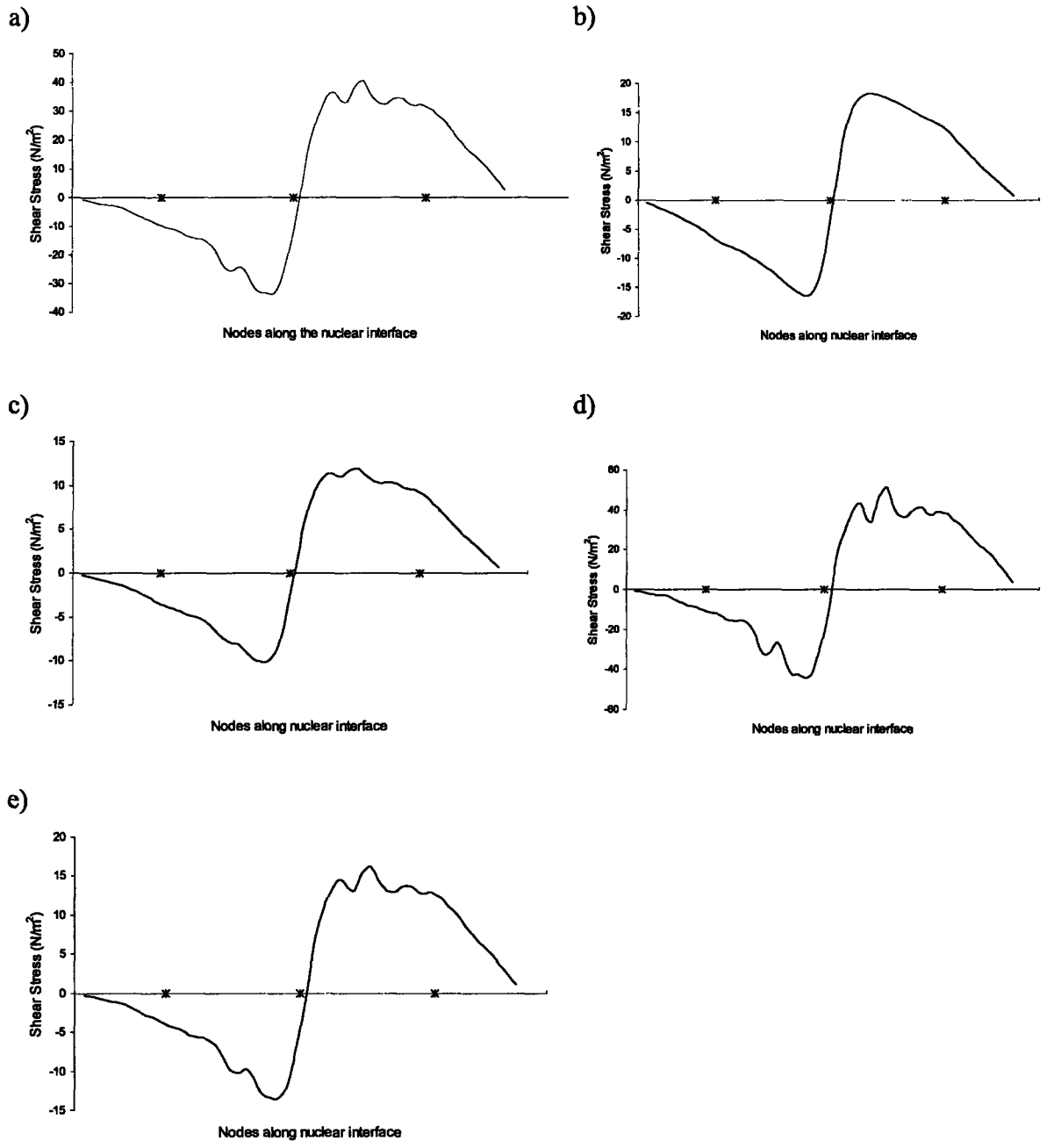

Figure G.3 Stresses (N/m^2) along nuclear interface for elliptical with various material properties. a) condition 1 - normal nucleus 1250 N/m^2, normal cytoskeleton 250 N/m^2 b) condition 2 – very soft nucleus 250 N/m^2, normal cytoskeleton 250 N/m^2 c) condition 3 – very soft nucleus 250 N/m^2, soft cytoskeleton 100 N/m^2, d) condition 4 – hard nucleus 2500 N/m^2, normal cytoskeleton 250 N/m^2, e) condition 5 – soft nucleus 500 N/m^2, soft cytoskeleton 100 N/m^2.

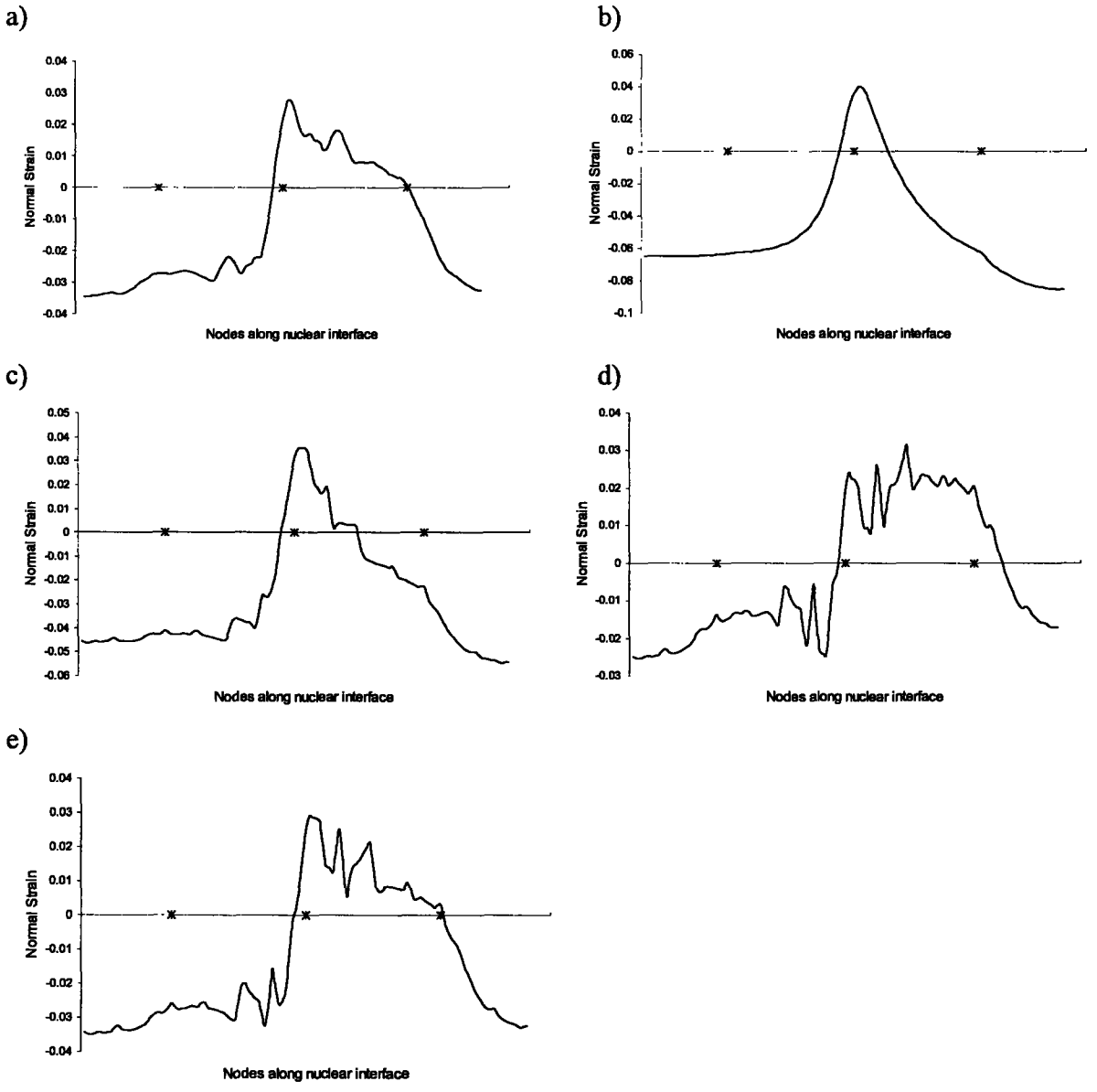

Figure G.4 Normal Strain along nuclear interface for elliptical with various material properties. a) condition 1 - normal nucleus 1250 N/m^2, normal cytoskeleton 250 N/m^2 b) condition 2 – very soft nucleus 250 N/m^2, normal cytoskeleton 250 N/m^2 c) condition 3 – very soft nucleus 250 N/m^2, soft cytoskeleton 100 N/m^2, d) condition 4 – hard nucleus 2500 N/m^2, normal cytoskeleton 250 N/m^2, e) condition 5 – soft nucleus 500 N/m^2, soft cytoskeleton 100 N/m^2.

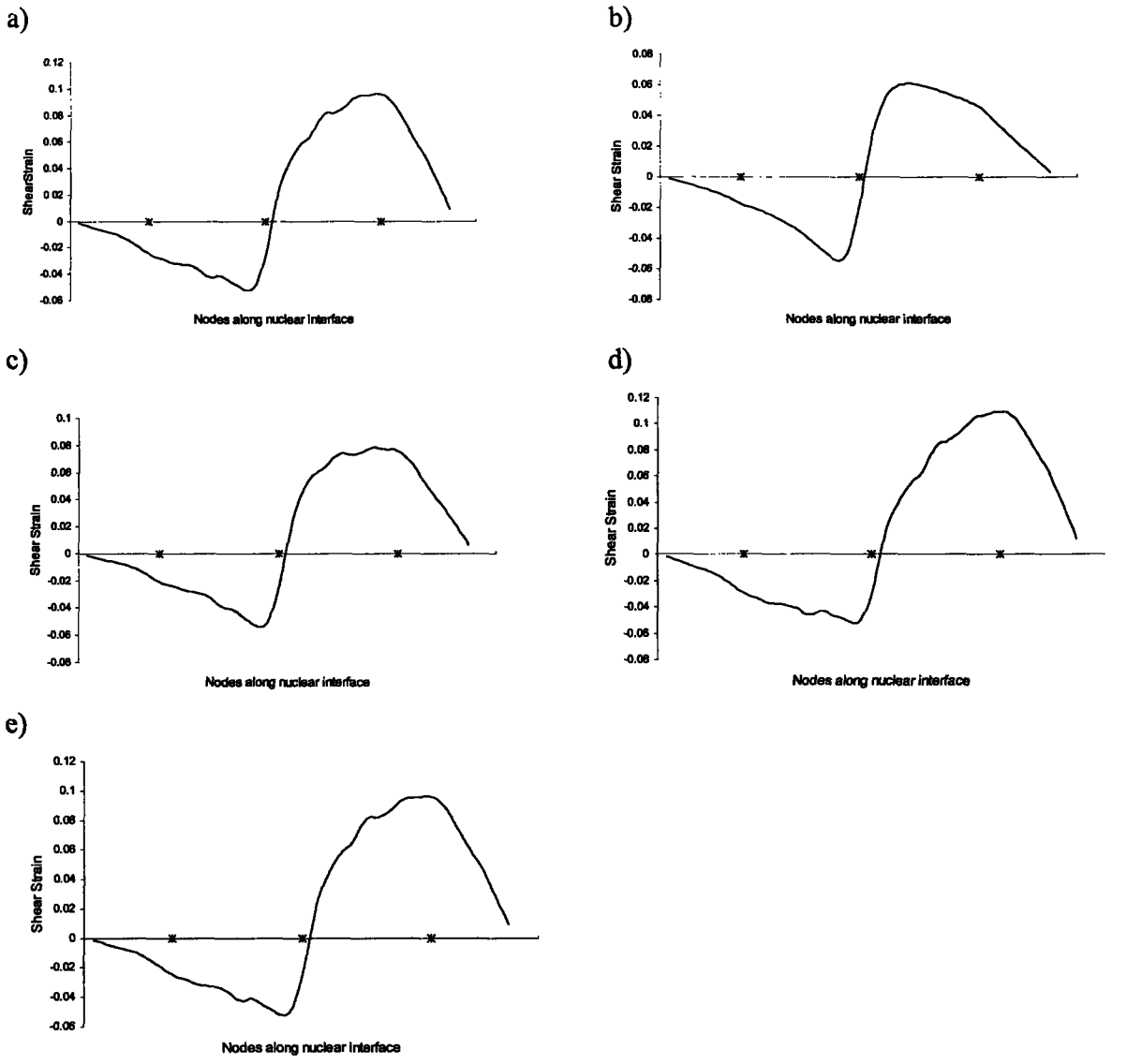

Figure G.5 Shear Strain along nuclear interface for elliptical with various material properties. a) condition 1 - normal nucleus 1250 N/m^2, normal cytoskeleton 250 N/m^2 b) condition 2 – very soft nucleus 250 N/m^2, normal cytoskeleton 250 N/m^2 c) condition 3 – very soft nucleus 250 N/m^2, soft cytoskeleton 100 N/m^2, d) condition 4 – hard nucleus 2500 N/m^2, normal cytoskeleton 250 N/m^2, e) condition 5 – soft nucleus 500 N/m^2, soft cytoskeleton 100 N/m^2.

a)

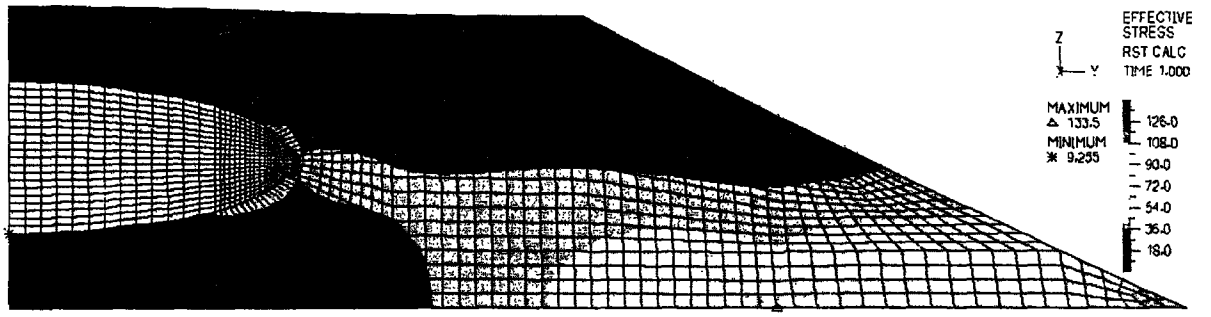

b)

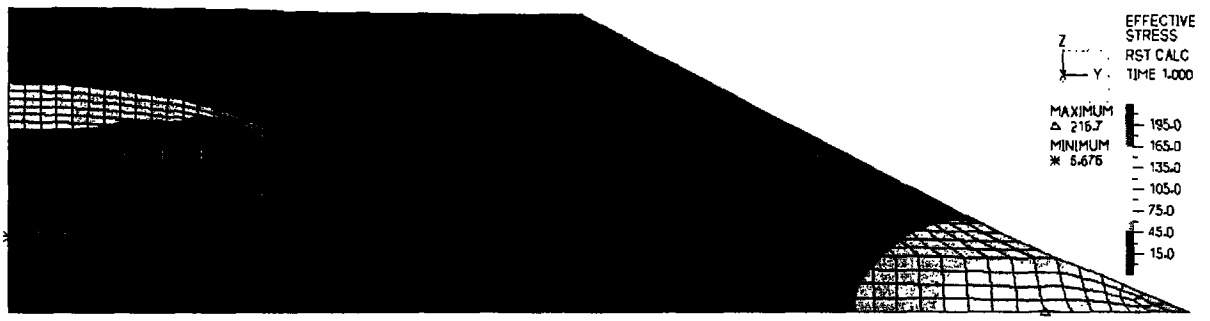

c)

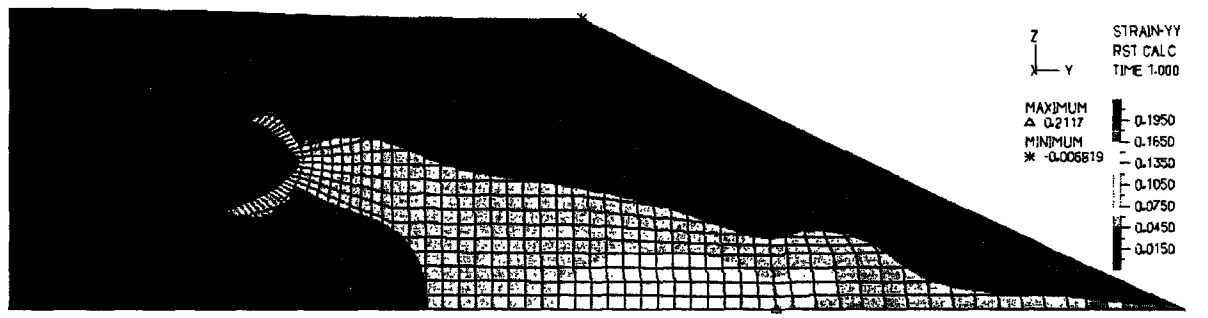

d)

Figure G.6 Band plot profiles of a) effective stress for 33% cell adhesion length b) effective stress for 10% cell adhesion length c) strain-vy for 33% cell adhesion length d) strain-yy for 10% cell adhesion length